Manipulation of nanoparticles by pushing operations using an Atomic Force Microscope (AFM)

A thesis

submitted to Cardiff University

for the degree of

Doctor of Philosophy

by

Mario Javier González Romo, M.Sc.

Institute of Manufacturing Engineering Centre

Cardiff University

School of Engineering

United Kingdom

September 2012.

SUMMARY

This thesis presents new paradigms for a particular class of non-prehensile manipulators of nanoscale objects that are limited to modelling accurately the relative motion of objects using continuous mechanics where the contact area is not presented. This restrictions results in models which have low accuracy and a lack of understanding about the real motion of the nanoscale object. The newly developed paradigms are focused on three topics: characterisation and analysis of forces present during motion at nanoscale in two dimensional space; characterisation and analysis of the quasi-static motion of nanoscale objects using the *the instantaneous centre of rotation* **iCOR**; and characterisation and analysis of the quasi-static, impulsive and dynamic motion of nanoscale objects using motion constraints and the **iCOR**.

For characterisation and analysis of forces present on objects being manipulated at nanoscale, new models to characterise rolling and sliding motion are introduced. For the sliding case a relation between friction load (force and torque) and slip motion (displacement and rotation) for rigid nano-object sliding on a flat and a rough surface, where the distribution of the normal contact forces is assumed to be known a priori and the friction is assumed to be independent of slip rate is introduced. Every point of frictional contact is assumed to obey Coulomb's friction law. A developed set of equations are solved, performing high accuracy integration techniques such as the **Bulirsch-Stoer Method** implemented on a computing programming language such as FORTRAN.

The full relation between the frictional load and the slip motion for a nano-object can thus be described by its **iCOR**. A new methodology to model the quasi-static motion of nanoscale objects is presented from which are derived equations that can be used to approximate the tri-

bological parameters of the nano-objects being manipulated for known and unknown contact pressure distributions. The characterisation of the tribological parameters, such as the coefficient of friction μ, is obtained from generated maps using the applied force or the observed **iCOR** location of the nano-object being manipulated. The approach has several advantages, including simplicity, robustness, and an ability to simulate classes of systems that are difficult to simulate using spatial mechanics.

The final part of this thesis introduces a novel constraint-based method in combination with a minimum force principle to locate the **iCOR** position for nano-objects at quasi-static motion. Furthermore, the **iCOR** location for impulsive and dynamic motion cases are introduced. The results generated by modelling these cases can describe the full motion of the manipulated nano-object and generate knowledge of their tribological parameters.

to my loving parents and family ...

Acknowledgements

DECLARATION AND STATEMENTS

DECLARATION

This work has not previously been accepted in substance for any degree and is not concurrently submitted in candidature for my degree.

Signed . . . .   (González Romo Mario Javier)   Date 28/09/2012.

STATEMENT 1

This thesis is being submitted in partial fulfilment of the requirements for the degree of Doctor of Philosophy (Ph.D.).

Signed . . . .   (González Romo Mario Javier)   Date 28/09/2012.

STATEMENT 2

This thesis is the result of my own independent work/investigation, except where otherwise stated. Other sources are acknowledged by explicit references.

Signed . . . .   (González Romo Mario Javier)   Date 28/09/2012.

STATEMENT 3

I hereby give consent for my thesis, if accepted, to be available for photocopying and for inter-library loan, and for the title and summary to be made available to outside organisations.

Signed . . . .   (González Romo Mario Javier)   Date 28/09/2012.

Table of Contents

List of Figures

xii

List of Tables

Nomenclature

k_z **AFM**-probe cantilever spring constant for bending due to the normal force.

α Geometrical parameter as defined in Figure 3.6.

α_r Nanotube angular rolling acceleration.

β Geometrical parameter as defined in Figure 3.4.

$\beta_1, \beta_2, \beta_3, \beta_4$ Geometrical parameter as defined in Figure 3.7.

$\ddot{\theta}$ In-plane nano-object angular acceleration.

$\ddot{x}$ In-plane linear acceleration of the nano-object centre of mass in plane OX.

$\ddot{y}$ In-plane linear acceleration of the nano-object centre of mass in plane OY.

$\Delta\theta$ **AFM**-probe torsional twisting cantilever deflection Figure 2.4 and Figure 2.5.

$\Delta\zeta$ **AFM**-probe normal cantilever deflection Figure 2.4 and Figure 2.5.

δA Differential element of area as defined in Figure 3.7.

$\dot{\theta}$ In-plane nano-object angular velocity.

μ Coefficient of friction between the nano-object an the supporting surface.

$\overline{a}_x$ Linear acceleration of the nano-object centre of mass during rolling motion.

ϕ Geometrical parameter as defined in Figure 3.4.

ρ Nano-object material density.

θ In-plane orientation of the nano-object as defined in Figure 3.4.

d Geometrical parameter as defined in Figure 3.4.

F Applied tangential force.

f Resultant frictional force.

$F_{adhesion}$ Adhesive force.

f_k Kinetic frictional force.

f_s Static frictional force.

F_{VdW} Van der Waals force.

$f_{x'}$ Component of the frictional force in the plane O'X'.

f_x Component of the frictional force in the plane OX.

$f_{y'}$ Component of the frictional force in the plane O'Y'.

f_y Component of the frictional force in the plane OY.

g Earth's constant of gravity defined as 9.81 m/s^2.

h Geometrical parameter as defined in Figure 3.1.

h_1, h_2, h_3, h_4 Geometrical parameter as defined in Figure 3.7.

$I_{C.M.}$ Nano-object inertia moment referenced to its centre of mass.

k Rolling coefficient of friction.

k_y^θ **AFM**-probe cantilever spring constant for twisting due to the lateral force.

k_y^b **AFM**-probe cantilever spring constant for lateral bending due to the lateral force

k_{xz} **AFM**-probe cantilever spring constant for bending due to the lateral force moment.

m Mass of the nano-object.

m_s Frictional moment.

N Normal force at contact.

r Radius of the nanotube.

W Total load acting between the nano-object and surface at contact.

X_m Nano-object centre of mass coordinate in plane OX as shown in Figure 3.6.

x_n Lateral distance as defined in Figure 3.4.

Y_m Nano-object centre of mass coordinate in plane OX as shown in Figure 3.6.

y_n Longitudinal distance as defined in Figure 3.4.

a,b   Contact area dimensions as defined in Figure 3.7.

O'X'Y'   Coordinate system associated with the nano-object.

OXY   Fixed coordinate system.

R   Distance between the nano-object centre of mass and its instantaneous centre of rotation as defined in Figure 3.7.

V   Volume of the nano-object.

AFM   Atomic Force Microscope.

C.M.   Nano-object centre of mass.

CNT   Carbon nanotube.

iCOR   Instantaneous centre of rotation.

MWCNT   Multi-walled carbon nanotube.

SPM   Scanning Probe Microscope.

STM   Scanning Tunneling Microscope.

Chapter 1

Introduction

1.1   Motivation

The invention and development of tools in the last two decades that can analyse objects in terms of their fundamental elements opened new opportunities in techniques and for the manipulation process. The ability to control and to understand objects at the nanoscale is a field which at the moment provides more questions than answers. In classic Newtonian mechanics, the mass of the object (the composition of the body) plays an important role. At the atomic level the mass is an important parameter which helps to organise elements in a periodic table. On the other hand, a large proportion of the research done at the moment at the nanoscale gives no such importance to this parameter when the motion of the object is described. Therefore, most of the reported equations of motion have a lack of the nano-object's mass in their terms.

Currently, modelling the motion of objects at the nanoscale is limited to models which have a lack of analysis over the contact area as the analysis is done for a line of contact. On the other hand, contact area analysis is restricted to being used on discrete models. Discrete models use a proposed real contact area. This real contact area is generally smaller than the boundary defined by the edge of the contact zone between the nano object and the substrate surface. The real contact area is analysed by multi-dynamics molecular analysis (**MDM**). Multi-dynamic-

molecular analysis is computationally expensive and limited to simulated small areas. In addition, the use of different and non-standard models which define the frictional force provide a big range of non-unified criteria and results.

Moreover, the reported manipulation of nano-objects is done most commonly by empirical experimentation. Nano-objects are manipulated and the generated motion registered in an attempt to characterise their motion. Therefore, more of the efforts are concentrated to model and described the actuator dynamic (**i.e. AFM**-probe) to provide a robust and efficient scheme of control which attempts to accurately and precisely position nano-objects into a desired location. In addition, manipulation at the nanoscale presents a lack of visual control as conventional optical microscopes breakdown. Thus, during the manipulation of nano-objects, it is difficult to correct any motion in real time. As a consequence, the resulting motion is only observed after the manipulation is completed and a technique that cope with uncertainly of the nano-object position is requested.

Furthermore, the study of analysis of motion of manipulated nano-objects is restricted to modelling quasi-static motion. This generates a gap in modelling other stages of motion that the nano-object being manipulated might experience. Analysing, studying and modelling these phases of motion can result in a more complete view of the motion that the nano-object will have a priori to be manipulated. Achieving controllability and repetition in the experimentation will also open a new understanding of the motion at the nanoscale.

All of these forecasting problems mentioned in previous paragraphs motivate a high interest in developing new and simple models which can describe the full dynamics of nano-objects being manipulated by pushing operations. A pushing operation is a robust technique and an efficient method being used at the macro-scale to accurately position objects. Translational motion and rotational motion are two basic operations to position objects. Therefore, translation and rotational motions can accurately be used for assembly tasks and to analyse materials properties at the nanoscale. Moreover, the motion of objects is directly related to their tribo-

2

logical properties. Tribological properties at the nanoscale are not well defined and need to be understood in order to provide accurate motion models of the objects being manipulated.

1.2   Aim and objectives

The aim of this research is to provide a new analysis and to develop new equations to describe the dynamics of nanoscale objects being manipulated with one point of contact by pushing operations. The specific objectives are:

1. To precisely and accurately calculate the position of nano-objects being pushed.

2. To study and to analyse Quasi-static, Impulsive and Quasi-dynamic motion of nanoscale objects.

3. To study and to analyse the frictional properties of the sliding nano-objects using their *instantaneous centre of rotation* **iCOR**.

4. To validate the use of Coulomb's friction law model at the nanoscale.

5. To study and analyse different types of motion such as the rolling and sliding of nano-objects.

1.3   Methods

For the aim and objectives proposed in this thesis and described in Section 1.2, each one will follow the same problem solving approach to reach the desired objectives. The methods used in this research may be summarised as follows:

Literature review: the most relevant papers for each research topic will be reviewed, pointing out the key results, advantages and disadvantages. This should help provide the groundwork for the research. In addition, all selected papers will be registered in a database using an specific utility for the generation of bibliographic references such as **jabRef**. **jabRef** provides visual tools to organise references by category. This will

3

provide a panoramic view of the topics and categories covered by the literature review. Also, it will shows the publication houses most relevant to our research.

Critical thinking: after the literature review is done, key questions for each research topic are generated to produce a hypothesis. Moreover, the hypothesis will provide a framework through which to look at things and also something to work towards. The framework analysis will derive new equations and methodologies which can explain and give answers to the nature of the selected issues. Ideas, analysis and discussions will be recorded by hand-writing in a notebook for further reference.

Experiments: practical simulated experiments are also required to validate the hypotheses and to see if the new developments really work. Each proposed method will be tested using different conditions or scenarios to increase the perception of the problem under analysis. Increasing the perception of the problem sometimes can give new directions making the hypothesis more robust. Finally, simulation programs will be provided with tools to help to organise the generated information. Consequently, a clear and organised record of the experiments will be made possible for further analysis.

1.4 Outline of the thesis

This thesis is organised into six chapters. The second chapter is the literature review. The next three chapters correspond to the three core research contributions. The sixth and final chapter of this thesis summarises the conclusions and possible directions for future work. The topics addressed in each chapter are as follows:

Chapter 2 presents the state of the art of the concepts behind the methods and techniques used at each stage of this research. This literature review will contain the most important and recent applications related to the fields developed in the main parts of this research.

Chapter 3 develops the architecture of the equations and will define the geometry of the parameters involved to the develop the equations of motion. The developed equations of motion are solved by accurate techniques implemented in a high-performance programming language. The developed programming code is used to analyse and describe the dynamics of nano objects being pushed. In particular, frictional force analysis for a contact area is carried out for two types of motion: Rolling and Sliding. Two different proposed models are introduced to explain the differences between the forces acting on the nano-object when it rolls or slides. Numerical simulations for these motions for different objects are presented. From previous simulations in sliding motion the problem of stick-slide takes a different perspective according to the obtained results whereas in rolling motion an erratic static frictional force behaviour is demostrated.

Chapter 4 describes a developed alternative and robust methodology to find *the instant centre of rotation* (**iCOR**) of nano objects. The **iCOR** is used to precisely characterise the nano-object going into sliding motion at any instant of time being pushed or pulled. The developed methodology is derived in equations which approximate the tribological properties of the nano objects being manipulated (*i.e.* coefficient of friction). Also, the developed equations are presented to model the **iCOR** location in known and unknown contact pressure distribution.

Chapter 5 reports the development of a new equation which improves the results in the location of the **iCOR** mentioned in Chapter 4 and extends an analysis to evaluate different conditions of motion. These conditions of motion correspond to the impulsive and dynamic cases. Then, the obtained results are critically analysed and a relation between the location of the applied force and a consistent **iCOR** location is presented.

Chapter 6 presents the conclusions and the main contributions of this thesis. Suggestions for future research in this field are also provided.

Chapter 2

Background

2.1   Introduction

This chapter starts with the state of the art regarding to manipulation process of micro and nanoscale objects by pushing operations. The chapter continues with a detailed description about techniques and methodologies implemented to manipulated objects. Finally, supported theory and description of interactive forces that perform between nanoscale objects is presented.

2.2   Manipulation of objects at nanoscale

The manipulation of elements down to atomic scale length has been related to the process of manufacturing. Manufacturing techniques are changing due to the characteristics of materials in size, shape and the manner of how materials need to be processed for the creation of new products [1, 2].

In dealing with the manufacturing process at the nanoscale, two approaches are implemented: **top-down** and **bottom-up**. The **bottom-up** or **self-assembly process** is focused on the assembly of nano devices using their atomic components and their chemical properties for assembly into more complex and organised structures without human or mechanical intervention [3, 4].

6

On the other hand, the **top-down** manipulation process of nanoscale elements involves mechanical manipulation using new, highly precise controlled tools [5–12].

The mechanical manipulation of objects at the nanoscale is achieved by techniques such as non-prehensile handling (**i.e.** pick and place operations). This is difficult to achieve as vision at the nanoscale is limited to the operator and adhesive forces became dominant [13–15]. On the other hand, the non-prehensile technique deals with the uncertainly in the location of the objects and reduces the amount of time required to position and orientate objects. Non-prehensile schemes of manipulation consist of pushing or pulling operations using one point of contact or more (**i.e.** stable pushing). Examples of this manipulation schemes have introduced in [16–23]. However, there is a lack of theoretical models which can describe the achieved results and only few of the cited literature references introduce models to describe the dynamics of the motion of the manipulated objects [24–28]. Therefore, this research is focused on the analysis and models to describe the manipulation of an object by non-prehensile techniques.

2.3   Scanning probe microscope SPM

Scanning probe microscopes (**SPMs**) represent a group of tools and techniques for imaging and manipulating objects at micro, nano and atomic levels [29–31]. In general, **SPMs'** image acquisition principle is based in a sharp tip/probe which scans the surface at close distance from it. Variation in the probe position due to electrostatic interaction between the probe and surface is transformed into a profile surface topography for later analysis and inspection. On the other hand, the use of **SMPs** for manipulation tasks can also be achieved by bringing the probe into mechanical contact with a micro/nano-object target.

The first device to belong to this category of **SPM's** is the *scanning tunnelling microscope* **STM**. Developed in 1980 by Bining and Gerber in the IBM Zürich laboratory, the **STM** gained for its inventors the Nobel Prize in 1986. The principle of operation of the **STM** consists in generating a constant tunnel current from a sharp and conductive probe which interacts very closly to a conductive surface (distances less than 10Å). The probe control is realised by means of piezo-drives, which expand and contract according to a drive voltage applied. Values in the tunnel current between the probe and the surface changes due to heights variations in the surface of the sample. Thus, by monitor variations of the tunnel current, a topography image of the sample can be obtained.

Manipulation using the **STM** was first reported by Eigler's group at the IBM Almaden laboratory to move and order Xenon atoms to build the IBM logo in the early 1990s by using a sliding or dragging process. In this scheme of manipulation, the **STM** probe is brought sufficiently close to an atom for the attractive forces to prevail over the lateral motion resistance. The probe then moves over the surface and the atom moves along with it. Finally, after the desired location is achieved, the probe withdraw from the surface leaving the atom in its new position.

The **STM** has two disadvantages which breaks down in two considerations; firstly, the **STM** can only work for conductive samples; secondly one, the **STM** operates in ultra hight vacuum (**UHV**) and in most cases at low temperature, resulting in time-consuming image acquisition process [32].

The second and most widely used instrument in the **SPM** category is the *Atomic Force Microscope* (**AFM**) [33]. Unlike its predecessor the **STM**, the **AFM** can operate in a diversity of environments like liquid, vacuum or ambient conditions, making it suitable for a variety of applications at micro, nano, atomic scales and biology applications [25, 34–42].

2.3.1   AFM-based nano manipulator

The **AFM** operating principle is similar to its predecessor the **STM**. Also, it can operate in a range of different modes (**i.e** contact, non-contact, lateral mode, etc...). In the **AFM** basic configuration, the *contact mode*, the **AFM** scans the surface with a sharp probe over a very short distance ($\sim$ 1nm). The **AFM**-probe is attached at the end of a rectangular or triangular cantilever. The geometry of the **AFM**-probe apex is spherical, with a radius of less than 10nm. Interactions forces between the sample and the **AFM**-probe are measured according to the cantilever deflection. This deflection will change according to the interaction between the **AFM**-probe and the surface topography. The cantilever deflection is obtained optically by hitting the back of it with a light beam (laser) and recording this deflection in a quadrant photo detector. Thus, the output signal of the photo detector become in a 3-D topography image of the sample under inspection. In addition, the **AFM** can be used to image conductive and non-conductive materials as electrostatic forces are present in all materials.

2.3.2   Methods for pushing of micro/nano particles.

Manipulation and assembly at the micro/nano scale has been an area of considerable research over the past several years. Critical to the development of micro/nano assembly is the study of the basic modes of manipulation such as pushing, pulling and pick and place. As a manipulation tool, the **AFM**-probe can be used to directly contact and position individual particles. Prior research demonstrated the ability to position individual particles of spherical and cylindrical shapes lying on planar surfaces through pushing and pulling techniques using an **AFM**-probe as a manipulator [34, 43–48]. In all previous pushing manipulation methods, the **AFM**-probe and particle come into contact and then move together until the contact between them is lost. After contact is lost, a subsequent image is taken to determine the actual position and orientation of the particle.

Dynamic motion models of the particle behaviour under manipulation are obtained using forces sensed by the **AFM**-probe. Then they can be used in order to predict the particle

motion. However, the accuracy of these models can be affected by the calibration of **AFM**-probe-sensing [49], ambient conditions and the nature of **AFM** sensors (piezo electric materials). In addition, substrate and particle materials are related with a particular type of interaction affecting how the particle is manipulated and behaves on the surface. Thus, a variation of these parameters and conditions can affect the resulted particle motion and particle-probe interaction. In the latter, a contact lost can occur due to the rotation of the particle with reference to the **AFM**-probe. Furthermore, the particle and **AFM**-probe could also slip or roll if a control technique is deficient to compensate this problems. Another problem related to pushing methods is sticking due to indentation (excess applied force) and electrostatic charges generated due to the friction of two surfaces in contact. The latter can be significantly reduced by grounding the substrate (connecting it to an electric ground) to dissipate the electrostatic currents generated during the particle movement.

On the other hand, some results have been achieved using *pulling* to position spherical particles [50]. However, pulling has been only achieved by selecting parameters such as the size of the particle, the radius of the **AFM**-probe, the force applied to the particle, and the tip-particle contact angle such that the adhesion force at the tip-particle interface exceeds the forces at the particle-substrate interface (tangential forces) to move the particle. As a result for most cases, adhesion forces at the particle-substrate interface are such that pulling cannot be achieved.

Whereas a major success has been achieved through *pushing* operations, yet a common problem is that the particle will slip or spin about the tip [51]. Therefore, *stablishing these particle conditions (**i.e.** translation and rotation) become of vital importance to assure success in the manipulation of objects at micro and nano scale*. Overcoming these problems, *pushing* is desirable for manipulation as *pulling* can only be achieved for larger particles where large adhesion forces are possible due to the large surface contact area at the tip particle-interface. In the next sections pushing strategies and methods will be described.

10

2.3.2.1 Method I: Moving substrate with controlled constant speed while the AFM-probe is in contact with particle.

In this method the stage z position is fixed at a constant reference height from the substrate using the signal coming from the **LVDT** (linear variable differential transformer) position sensor integrated with the **AFM** z-axis control stage. This signal is used to measure the **AFM**-probe deflection (**i.e.** forces during pushing). This technique assumes the substrate is very flat and parallel to the $x - y$ positioning stage which is not always the surface case.

For instance, this method is being used to characterise the frictional behaviour between the nano particle and the substrate at contact by measuring the forces during pushing [52]. However, this technique can not compensate for errors due to the substrate random height or orientation differences introducing these errors into the measured frictional values, affecting the control scheme efficiency.

The control scheme is shown in Figure 2.1 where the tip-particle contact force F_z^c is monitored at each $x - y$ stage (X_i, Y_i), $i = 1, \cdots, \frac{\Delta L}{\Delta}$ where Δ is the $x - y$ motion position size. As **error sources** considered in this approach are:

1. The particle sticks to the **AFM**-probe and the $x - y$ force offsets value adjustment. Shortly after the **AFM**-probe makes contact with the particle, the applied force will increase the pushing force to overcome the static friction force of the particle. Thus, the transition from the static to the kinetic phase of the pushing particle will be controlled by the $x - y$ force offset value taking time to adjust the force applied, inducing an error source.

2. The **AFM**-probe-particle contact loss. This error, despite the closed-loop control, is expected due to the $x - y$ positions errors at the contact point and by the rotation/spinning of the spherical particle along the z axis during *pushing*.
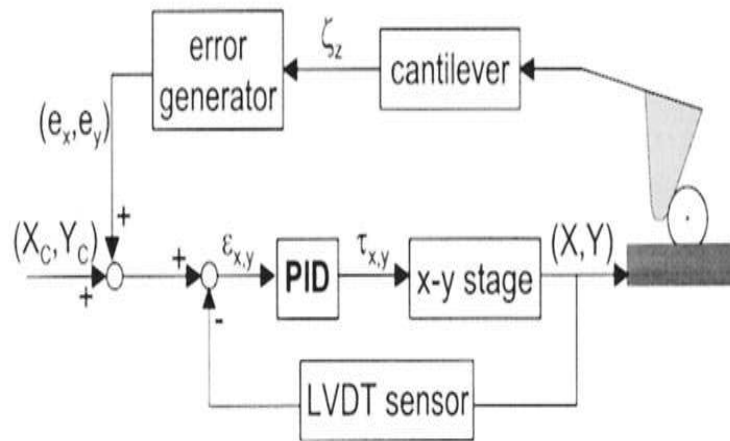
Figure 2.1: Control scheme for particle pushing with a constant **AFM**-probe height -adapted from [53].
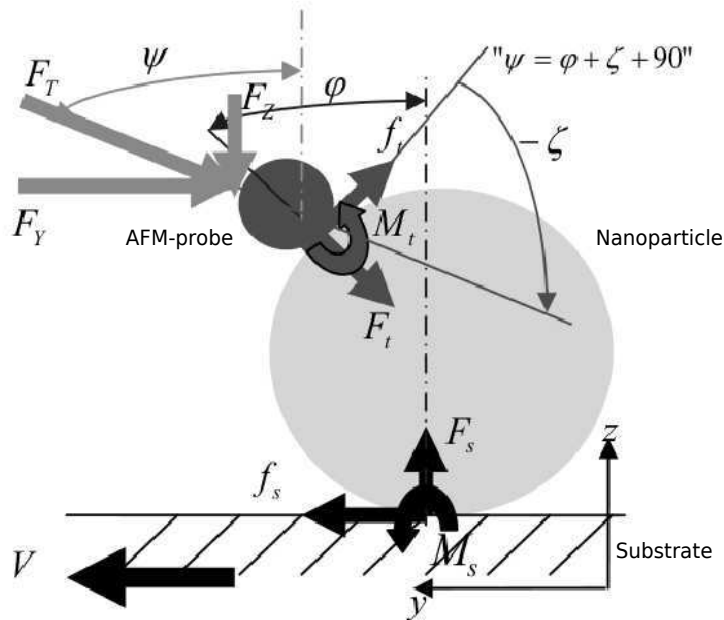
Figure 2.2: Forces during pushing a nanoparticle using an **AFM**-probe and nanoparticle modeled as sphere -adapted from [54].

2.3.2.2 Method II: AFM-probe moves and pushes the targeted particle over an immobile substrate.

In this method the resultant tangential force (F_T), *pushing force*, acting between **AFM**-probe and the nanoparticle is kept constant. The desired nanoparticle manipulation is provided by controlling the **AFM**-probe load/normal force F_z and its contact angle φ between the **AFM**-probe and the nanoparticle. The **AFM**-probe and nanoparticle are modeled as spheres of radius R. The **AFM**-probe angle is designed to be constant and greater than zero $\psi = \varphi + \zeta + 90°$ for a *pushing* task, as shown in Figure 2.2 above.

Figure 2.2 shows the analysis of forces during the pushing scheme, where f_s is the tangential/sliding frictional force between the nanoparticle and the substrate, F_s is the normal or reactive force between the nanoparticle and substrate at contact, M_s is the rolling friction moment acting on the nanoparticle and substrate as it rolls, M_t is the rolling friction rolling moment between the **AFM**-probe and the nanoparticle at contact, F_t is the normal or reactive force between the **AFM**-probe nanoparticle and the nanoparticle at contact, f_t is the tangential/sliding frictional force between the **AFM-**probe and nanoparticle, F_Y is the **AFM**-probe lateral applied force, V is the substrate speed to neglect inertia effects, ψ is the **AFM**-probe - nanoparticle angle in degrees, and ζ is the **AFM**-probe normal deflexion.

To predict the dynamic behaviour of a spherical nanoparticle such as sliding, rolling, and spinning, proposed empirical frictional models are derived. Solving and plotting these equations results in mode diagrams. Mode diagrams can related to the dynamic behaviour of nano particles and present and idea about the motion. However, problems arise if the tip slips from the particle surface and make a contact with the substrate instead of the particle during a *pushing* operation. This case becomes possible if the particle rolls [54]. Slow *pushing* and careful design of the **AFM**-probe-particle friction/sticking can eliminate this problem. The proposed control scheme in [53] for positioning spherical particles with constant contact force control is shown in Figure 2.3.
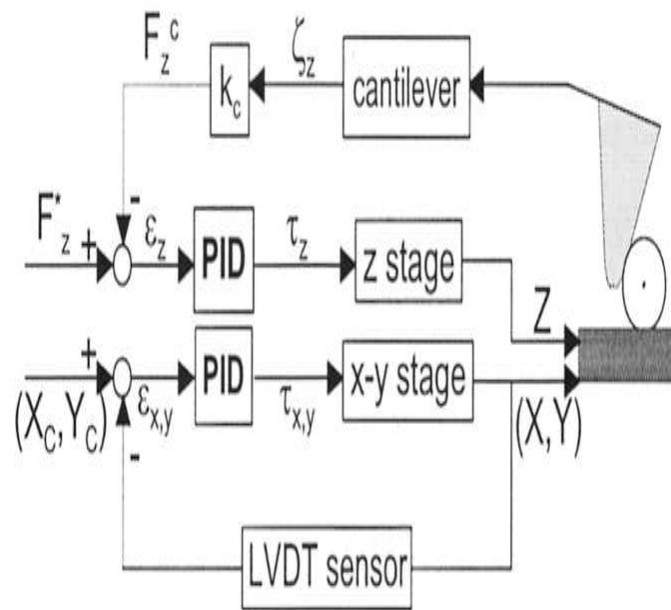
Figure 2.3: Control scheme for particle pushing with an AFM-probe constant force control -adapted from [53].
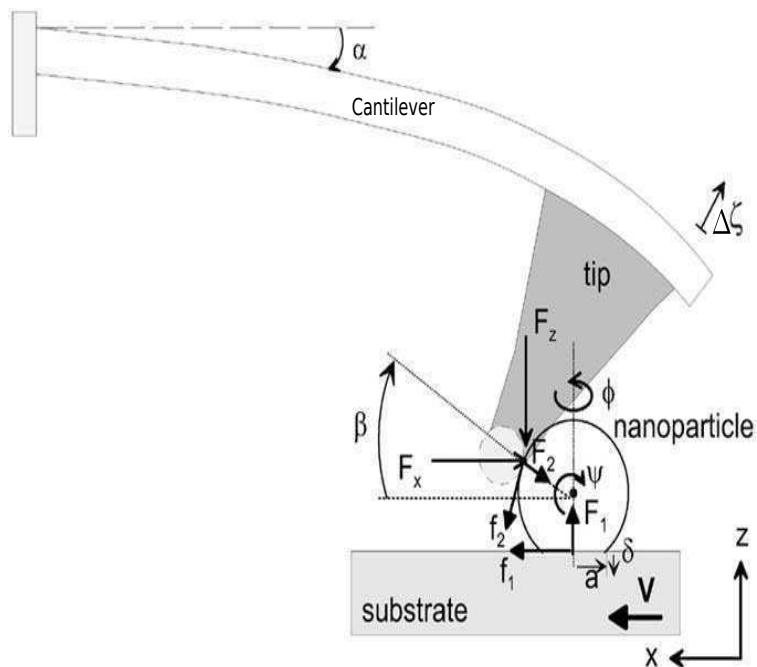
Figure 2.4: 1-D force analysis for **AFM**-probe-particle pushing interaction -adapted from [52].

The **AFM**-probe deflection measurement can be applied in two possible variations according to the number of forces registered. Therefore,

a) 1-D force sensing AFM-probe

Using 1-D optical or piezoresistive sensing, deflection data $\Delta\zeta$ is measured. This kind of simple set-up would indirectly measure the frictional force F_x by pushing the particle in the x-direction. The normal deflection of the **AFM**-probe is given by:

$$\Delta\zeta = \frac{F_z \cos\alpha - F_x \sin\alpha}{k_z} - \frac{F_z \sin\alpha + F_x \sin\alpha}{k_{xz}} \qquad (2.1)$$

where $\Delta\zeta$ is the only measured parameter which depends both on F_x and F_z.

For instance, assuming that F_z is relatively very small with respect to F_x by setting $\beta \approx 0$, the bending due to F_x is maximized by selecting α tilt angle large and an **AFM**-probe with a large probe height and short probe length, the force in x direction F_x can be extracted from the deflection data as shown in Figure 2.4. Also, Figure 2.4 shows the analysis of forces during the pushing scheme, where f_1 is the tangential/sliding frictional force between the nanoparticle and the substrate, f_2 is the tangential/sliding frictional force between the **AFM-**probe and nanoparticle, F_1 is the normal o reactive force between the nanoparticle and substrate at contact, F_2 is the normal o reactive force between the **AFM**-probe nanoparticle and the nanoparticle at contact, F_x is the **AFM**-probe lateral applied force, F_z is the **AFM**-probe normal/load force, β is the angle between the $x-axis$ and **AFM**-probe, α is the **AFM**-probe deflexion angle, ψ is the nanoparticle rolling angle, ϕ nanoparticle spining angle, ζ is the **AFM**-probe normal deflexion measured according to Equation (2.1), δ is the identation depth, a is the radius of the contact area between the nanoparticle (nanosphere) and the substrate, and V is the substrate speed to neglect inertia effects.

b) 2D force sensing AFM probe

In this method, the particle is pushed in the y-direction ($R_x = 0$) as shown in Figure 2.5, and F_y and F_z are measured simultaneously from the torsional twisting cantilever deflection $\Delta\theta$ and the normal cantilever deflection $\Delta\zeta$ datas [55]. Figure 2.5 shows the analysis of forces during the pushing scheme, where f_1 is the tangential/sliding frictional force between the nanoparticle and the substrate, f_2 is the tangential/sliding frictional force between the **AFM-**probe and nanoparticle, F_1 is the normal o reactive force between the nanoparticle and substrate at contact, F_2 is the normal o reactive force between the **AFM**-probe nanoparticle and the nanoparticle at contact, F_y is the **AFM**-probe lateral applied force, F_z is the **AFM**-probe normal/load force, β is the angle between the $y-axis$ and **AFM**-probe, α is the **AFM**-probe deflexion angle, ψ is the nanoparticle rolling angle, ϕ nanoparticle spining angle, ζ is the **AFM**-probe normal deflexion meassured according to Equation (2.2), δ is the identation depth, a is the radius of the contact area between the nanoparticle (nanosphere) and the substrate, and V is the substrate speed to neglect inertia effects. In this case, beam deflection equations are defined as:

$$\Delta\zeta = \frac{F_z \cos(\alpha)}{k_z} - \frac{F_z \sin\alpha}{k_{xz}} \tag{2.2}$$

$$\Delta\theta = S_\theta \frac{F_y}{k_y^\theta} \tag{2.3}$$

$$k_z = \frac{E\omega t^3}{4l^3} \tag{2.4}$$

$$k_{xz} = \frac{2L_s}{3} k_z \tag{2.5}$$

$$k_y^\theta = \frac{G\omega t^3}{3lH^2} \approx \frac{L_s^2}{2} k_z \tag{2.6}$$

$$k_y^b = \frac{Et\omega^3}{4l^3} = \left(\frac{\omega}{t}\right)^2 k_z \tag{2.7}$$
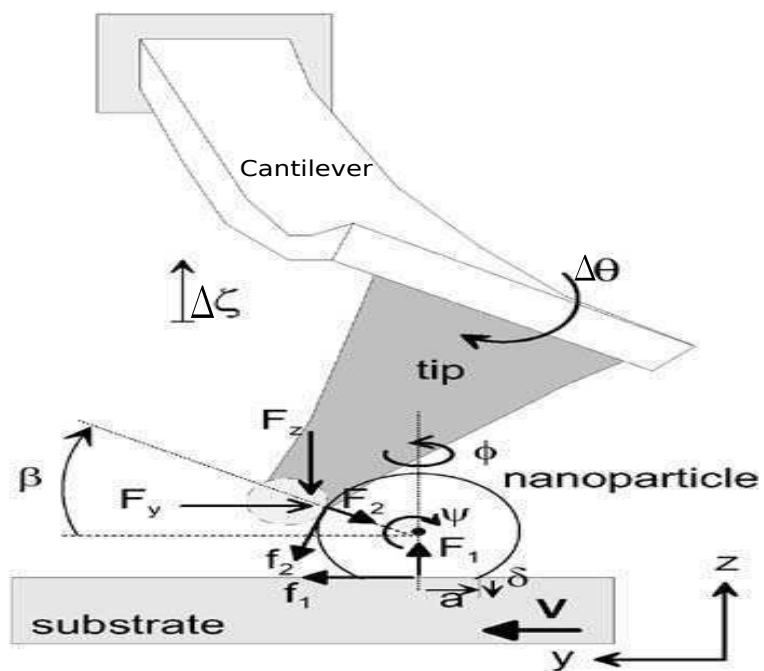
Figure 2.5: 2-D force analysis for **AFM**-probe-particle pushing interaction -adapted from [52].

where k_z, k_{xz}, k_y^θ, and k_y^b are the spring constants for bending due to the normal force, bending due to the lateral force moment, twisting due to the lateral force, and lateral bending due to the lateral force, respectively. Also, $E = 2(1 + \nu)G$, $\nu \approx 0.33$, l, ω, t, $L_s = \frac{l}{H}$, and H are the Young's modulus, shear modulus, Poisson 's ratio, length, width, thickness, structural constant, and tip height of the beam, respectively, S_θ is the sensor coefficient for the twisting measurement, and α is the beam tilt angle from the base guaranteeing the point contact of the particle with the substrate.

From Figure 2.5 measured forces to analyse the particle at *quasi-static motion* are related by equations

$$f_1 = F_z = F_2 \cos(\beta) - f_2 \sin(\beta) \tag{2.8}$$

$$f_2 = f_z \cos(\beta) - F_y \sin(\beta) \tag{2.9}$$

$$F_z = F_1 \tag{2.10}$$

Thus, the empirical possible models of motion observed for a nanosphere are:

- **Sticking:** If $F_y = f_1 < \tau^s A$ and $f_2 < \tau^s A_2$, the particle would stick to the substrate and tip.

- **Sliding:** If $F_y = f_1 \geq \tau^s A$ and $f_2 < \tau^s A_2$, the particle would slide while stuck to the tip.

- **Rolling:** If $(f_1 - f_2)R \geq f_1^\psi$ and $f_2 \geq \tau^s A_2$,(**i.e.** $f_2 = \tau A_2$), the particle would start to roll while sliding from the tip. The same equation can be written as

18

$$[f_z \cos(\beta) - (1 + \sin(\beta))F_y]R \geq \tau_\psi A \qquad (2.11)$$

- **Rotation (Spinning):** If there is an offset of x_0 along the x-axis, spinning could occur along the z-axis when $F_z x_0 \geq \tau_\theta A$, where τ_θ is the rotational friction coefficient.

where $A = \pi a^2$ and $A_2 = \pi a_2^2$ are the real contact areas for the particle-substrate and tip-particle and a, a_2 are the real contact radii of each interaction respectively, τ^s is the static or kinetic (τ) shear stress of the particle and substrate contact and the tip and particle contact points.

2.3.2.3 Method III: Non-contact AFM mode.

In 1998 Martin et al. [16] reported a method to manipulate using the non-contact **AFM**. In this method, particles to manipulate are metallic, of spherical shape with a size between 10 to 100 nm on a smooth silicon dioxide substrate (**i.e.** aerosol particle's). During the **NC-AFM** mode, the **AFM**-probe vibrate at a constant frequency near to the surface (substrate). The vibration amplitude diminishes as the distance decreases. Changes in the amplitude are used to generate an image of the topography. In this mode, the **AFM**-probe is used for locating and moving particles. Moreover, when using this technique the possibility of scanning the surface and moving the particle at the same time became possible. This operation avoids the sticking problem that typically makes manipulation difficult in the **AFM** contact mode. The control scheme algorithm developed by Sitti in [52] to move particles is summarised as

1. An image of sample deposited on the substrate is taken where a target particle is selected.

2. The **AFM** amplitude feedback loop control is set at a very low amplitude rate (**i.e.** 2 Hz

). Then, a linear trajectory path is selected in the desired direction to move the chosen particle. The length of the trajectory line scan is set to be about two or three times the particle diameter, and its direction controlled by the angle scan parameter from the **AFM** main control interface.

3. The **AFM** amplitude feedback control loop is then switched off to have control only in the direction of the z axis.

4. The **AFM** probe height is increased gradually (brought close to the surface/particle) until there is a clear change in the vibration amplitude of the **AFM**-probe. An offset between the surface and particle height is calculated to place the vibrating **AFM**-probe above the particle. The point which the **AFM**-probe touches the particle/substrate is easy located as the vibration amplitude becomes zero. This guarantees that the movement begins in the desired location.

5. Based on how the **AFM**-probe amplitude changes, it can be chosen either to lift or lower the **AFM**-probe position to achieve a strong tip-particle interaction.

6. When the **AFM**-probe touches the particle, it tries to push it towards the end of the scan. The signal from the vibration amplitude is monitored in real time to dertermine the position of the particle. Displacements of the particle may take place in one single push or it may take a few scans to achieve it.

7. After the particle has been moved, there is some offseting of the scan line to continue the movement until the final position is reached. If more than one pushing operations are needed, the current particle position to start the motion can be located without taking a topography image each time as the position and displaced length of particle is known at each manipulation stage.

2.3.3 Manipulation strategies

Manipulation strategies can be divided into two categories: Non-automatic and Automatic.

2.3.3.1 Non-automatic pushing strategy

In method I and method II, the pushing manipulation strategy followed by the **AFM** was accomplished by the motion steps shown in Figure 2.6, where:

1. $1 \rightarrow 2$ (auto-parking): The **AFM**-probe is automatically moved in the z direction until it detect contact with the substrate by measuring the cantilever deflection (absolute tip-substrate distance is not known initially), and retracted back to a predetermined parking height h_{set}.

2. $2 \rightarrow 3$ (automatic **AFM**-probe-particle contact detection): The **AFM**-probe is moved along the substrate until it detect the particle by the cantilever deflection detection, and is then stopped.

3. $3 \rightarrow 4$ The particle is pushed for a desired distance Δy by moving the substrate or the **AFM**-probe with constant speed.

4. $4 \rightarrow 5$ After completing the pushing operation, retracting back to the initial height occurs.
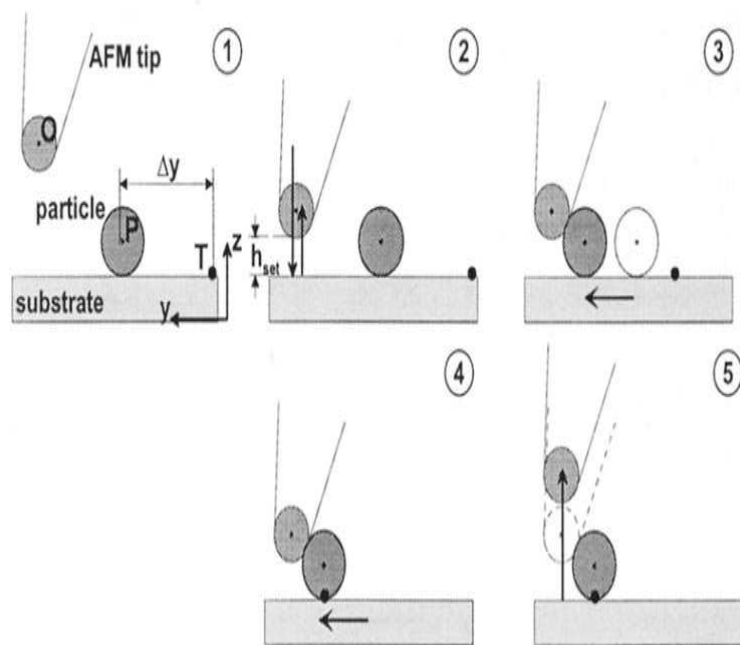
Figure 2.6: 1-D schematic strategy for particle pushing -adapted from [53]

2.3.3.2 Automatic pushing control scheme

Basics steps for an automatic control scheme to move micro/nano-objects can be summarised as follows:

1. Scan the substrate with semi-fixed micro/nano-objects on it, and get the 3-D tapping mode **AFM** image.

2. Detect a separate single micro/nano-object with an expected geometry and size using an unsupervised clustering object segmentation algorithm.

3. Position the **AFM**-probe with a pre-determined XYZ distance to the single micro/nano-object.

4. Get a small window **AFM** tapping mode scan over the micro/nano-object again to correct any positional error.

5. Automatically detect the peak height along the window, and compute the pushing line passing through the object centre.

6. Move the XYZ position along the pushing-line in 1-D with constant height h and linear speed V, push the object for a defined distance, and record the pushing force data.

Strengths and weaknesses of these three methods and their characteristics are summarised and presented in Table 2.1.

Table 2.1: Strength and weakness for three different pushing methods. $\cdot/-$ included/not included in the manipulation scheme.

Description	Method I	Method II		Method III
	Moving sub-strate with constant speed while AFM probe is in contact with particle.	(a) 2D AFM probe force sensing.	(b) 1D AFM probe force sensing.	Non-contact AFM mode
Flat substrate and parallel to the x-y position stage	•	•	•	•
Substrate random height	–	•	•	•
Frictional sticking	•	•	•	–
Tip-particle contact loss	•	•	•	•
Rotation spinning of particles along z axis	•	•	•	•
Close-loop control	–	•	•	•
Normal cantilever deflection measurement	•	•	•	–
Cantilever torsion twisting measurement	–	•	–	–
Acknowledge of the particle position during pushing	–	–	–	•

2.4 Interaction forces at nanoscale

Interactive forces between particles, molecules and atoms can be classified in four categories. Two of these categories correspond to *strong* and *weak* interactions which exist among neutrons, protons, electrons and other elementary particles. Their influence is limited by a short distance range (less than 10^{-5} nm). The remaining categories are the *electromagnetic* and the *gravitational* interactions. *Electromagnetic* and *gravitational* interactions have bigger distance influence and they can affect to the totality of the existent matter in the universe (atoms, molecules as well as between elementary particles, planets, etc...).

For instance, forces at the nanoscale correspond to *electromagnetic interactions*. These forces share essentially the same electrostatic origin. Moreover, for two charges the interactive force is related with the familiar inverse-square Coulomb force, whilst if the same charges are moving, they are related by electromagnetic forces. Electromagnetic forces are complex and rise due to the fluctuating charge distributions occurring inside and around atoms. Nevertheless, it could be possible to obtain and derive some inter-atomic and inter-molecular forces familiar to physics, chemistry and biology.

The value of electromagnetic forces can be obtained by solving the Schödinger equation. Solving the Schrödinger equation will predict the spatial distribution of the electron clouds. Unfortunately, solutions of this equation are not easy to come by. In fact, it is even too difficult to solve (exactly) something as simple as two hydrogen atoms interacting in a vacuum. For this reason, it has been found useful to classify intermolecular interactions into a number of different categories even though they all have the same fundamental electrostatic origin. Terms such as ionic bonds, metallic bonds, **Van der Waals forces**, hydrophobic interactions, hydrogen bonding and solvation forces are the result of this classification.

2.4.1   Intermolecular potentials

Intermolecular potential may be defined as how one particle will interact with others. Intermolecular potential has either a *repulsive component* and an *attractive component* or only one component which can be *attractive* or *repulsive*. The *repulsive component* prevents the collapse of molecules by repelling them as them get closer each other, whereas the *attractive component* will attract them to get closer as they are far away.

On the other hand, the interactive-based potential energy will result in an intermolecular force between the particles. This intermolecular force can be expressed as the variation of this interactive energy with respect to the distance between the particles. (**i.e.** the derivative of the resulted expression from the total interactive energy). Moreover, when the intermolecular potential is not monotonic (**i.e.** not purely attractive or repulsive) the experienced intermolecular force magnitude and direction will change according to the specific form of the long-range distance dependence and its particular interactive potential between them. As a consequence, the magnitude and direction of the interactive force in most cases are difficult to predict. Nevertheless, some interactive potential can be characterised by experimentation [56–58].

2.4.2   Intermolecular forces effects in a short-long range

Intermolecular forces magnitudes have different values and effects at short and long range. *Short range means at or very close to molecular contact (< 1 nm)*, whereas *long range forces are rarely important beyond 100 nm (0.1 μ m)* as its magnitude decreases. Therefore, the magnitude of intermolecular forces between particles (**i.e.** particle-particle or particle-surface) could change its magnitude according to

1. The total interaction energy is proportional to the size (**i.e.** radius) of the particles, so that the energy can be very much larger than an energy interaction barrier of **kT**[1] even a separations of 100 nm or more.

---

[1]kT is the product of the Boltzmann constant, *k*, and the temperature *T*.

2. The interactive energy and force decay much more slowly with the increased separation between the particles.

Consequently, interactions between micro/nano particles are effective at much longer range than those between molecules, even though the same basic type of force may be operating in both cases.

2.4.3   Interaction energy difference between molecular and sized particles

Different interactive potentials are shown in Figure 2.7. In particular it shows the purely attractive interaction potential shown in Figure 2.7-(a), when both molecules or sized particles experience the same type of interaction, both will be attracted to each other. Thus, the thermodynamic properties of an assembly of molecules in the gas or condensed phase will be determined by the depth of the potential at contact (global minimum in the curve), as it will be the corresponding adhesion energy of two particles.

For the energy law represented in Figure 2.7-(b), two molecules will still attract each other since the interaction energy barrier is negligibly small compared to **kT**[2], but two micro/nano particles will effectively repel each other since the energy barrier is now too high. Consequently, if the particles are dissolved in a medium, they will remain dispersed even though the ultimate thermodynamic equilibrium state is the aggregated state.

Another important difference between molecular and particle interactions is that particles can be (and often are) trapped in some kinetic or metastable state (**i.e.** equilibrium condition). Thus, if there is a sufficiently high energy barrier over some reasonable time, which prevents them from accessing all parts of their potential interaction, there will not be any change in their current state.

---

[2]kT is the product of the Boltzmann constant, k, and the temperature T.
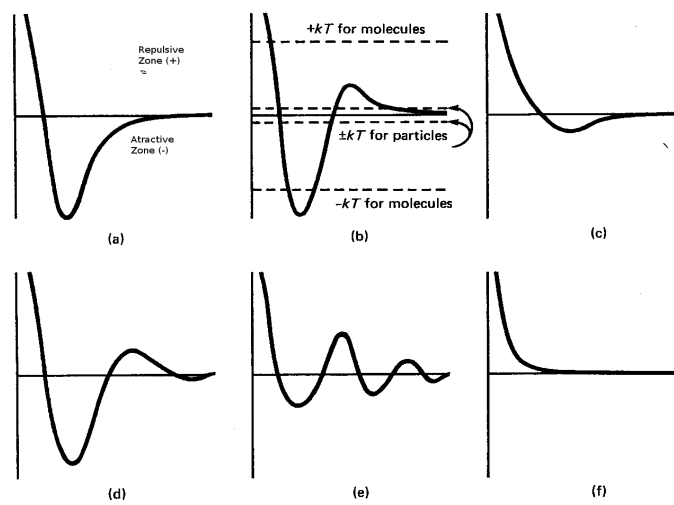
Figure 2.7: Typical interactive potentials encountered between molecules and macroscopic particles in a medium. (a) This potential is typical of vacuum interactions but is also common in liquids. Both molecules and particles attract each other. (b) Molecules attract each other; particles effectively repeal each other. (c) Weak minimum. Molecules repel, particles attract. (d) Molecules attract strongly, particles attract weakly. (e) Molecules attract weakly, particles attract strongly. (f) Molecules repel, particles repel -adapted from [59].

2.4.4 Van der Waals Forces

The **Van der Waals forces** are present in attractions between atoms, molecules, and surfaces in contact. It is also sometimes used as a synonym for the totality of intermolecular forces that will interact at macro, micro, nano and atomic levels. **Van der Waals forces** are relatively weak compared to normal chemical bonds. They are different from covalent and ionic bonding as they are caused by correlations in the fluctuating polarisations of nearby particles.

The magnitude of the **Van der Waals forces** is defined by the inter-molecular potential (the energy of interaction between the two entities). Broadly speaking, the **Van der Waals forces** consist of three different elements:

1. The *electrostatic interaction* between charges (in the case of molecular ions), dipoles (in the case of molecules without inversion centre), quadrupole (all molecules with symmetry lower than cubic), and in general between permanent multi-poles. The electrostatic interaction is sometimes called the Keesom interaction or Keesom force after Willem Hendrik Keesom.

2. The second source is *inductive attraction* (also known as polarisation), which is the interaction between the permanent multi-pole on the molecule with an induced multi-pole on another. This interaction is sometimes measured in Debbys after Peter J.W. Debye.

3. The third interaction force is usually named after Fritz London who himself called it *dispersion interaction*. This is the attraction experienced by non-polar atoms, but it is operative between any pair of molecules, irrespective of their symmetry.

Dispersion forces or **London forces** are the major contribution to the total **Van der Waals force** between atoms, molecules and particles. Also, they are always present in all materials

in contrast to the other two mentioned types of forces that might or might not be present depending on the properties of the molecules.

In addition, **Dispersion forces** are host of important phenomena such as *adhesion*, *surface tension*, *physical adsorption*, *wetting*, *the properties of gases*, *liquids and thin films*, *the strengths of solids*, *the fluctuation of particles in liquids*, and *the structures of condensed macromolecules* such as proteins and polymers.

From the London's theory, the interactive energy **w**, between two identical atoms or molecules is expressed as:

$$w(z) = -\frac{3}{4}\frac{\alpha_0^2 I}{(4\pi\varepsilon_0)^2 r^6} = -\frac{3}{4}\frac{\alpha_0^2 h v}{(4\pi\varepsilon_0)^2 r^6} = -\frac{C}{r^6} \tag{2.12}$$

where C is a constant that summarise some of the follows parameters h is the Planck constant, v the orbiting frequency of the electron, ε_0 is the medium dielectric constant, α_0 is the electric polarisability or magnetic constant. r is the distance between the atoms. The hv is equal to the energy needed to ionise the atom or the first ionisation potential I. Equation 2.12 can be used to calculate the interaction energy between particles based on the principle of summation. Finally, **Dispersion forces** main features are summarised as

1. They are long range forces and depending on the situation, can be effective from large distances (greater than 10 nm) down to inter atomic spacings (about 0.2 nm).

2. The forces may be repulsive or attractive, and in general the dispersion force between two molecules or large particles does not follow a simple power law.

3. Dispersion force not only brings molecules together but also tends to mutually align or orient them, though this orienting effect is usually weak.

4. The dispersion interaction of two bodies is affected by the presence of other bodies nearby (known as the non-additive of an interaction).

2.5 Van der Waals force magnitude between particles at contact and short range distance

The Van der Waals force magnitude between particles can be calculated based on the total interaction energy as mentioned before in Section 2.4.1. For instance, for two particles located a distance D apart, the summation principle (or pair-wise additive) will calculate the interaction energy between an elementary element of one particle and all counterpart elementary elements from the second particle. Carrying out the same process for all elementary elements is done for both particles [60].

In this research, the magnitude of the *Van der Waals* force is calculated assuming that the pair potential between two atoms or small molecules is purely attractive and of the form

$$w(r) = -C/r^n \tag{2.13}$$

where $n = 6$ is the power law corresponding to the Van der Waals, $\mathbf{r}$ the interactive distance between the *particles*, C is the constant defined in previously in Equation (2.12) and $\mathbf{w}$ denotes the interacting energy, which is in function of the distance. Examples of the principle taken from [59] are shown below.

2.5.1 Molecule-surface energy and interaction force

Firstly, assume that the surface is planar and made up of like molecules. Secondly, the surface will be divided into infinitesimal elemental volume sections which are constituted by molecules. By doing this, the total energy due to its interactive potential will be similar to calculate to the interactive potential energy interaction between two molecules. Thirdly, define the geometrical parameters as shown in Figure 2.8. They will define how the sum of all its interactions of all the molecules in the body will be carried out (**i.e.** integrating function and integrating limits). Therefore, molecules in a circular ring of cross-sectional area dx dz and radius x, the ring volume is $2\pi x dx dz$, and the number of molecules in the ring will be $2\pi \rho x dx dz$, where ρ is the number density of molecules in the solid. The total interaction energy for a molecule at a distance D away from the surface is calculated by

$$w(D) = -2\pi C\rho \int_{z=D}^{z=\infty} dz \int_{x=0}^{x=\infty} \frac{xdx}{(z^2+x^2)^{n/2}} = \frac{2\pi C\rho}{(n-2)} \int_D^\infty \frac{dz}{z^{n-2}} \qquad (2.14)$$

$$w(D) = -\frac{2\pi C\rho}{(n-2)(n-3)D^{n-3}} \qquad for \quad n > 3 \qquad (2.15)$$

which for $n = 6$ (van der Waals forces) becomes

$$w(D) = -\pi C\rho/6D^3 \qquad (2.16)$$

The corresponding force is then,

$$F = -\delta w(D)/\delta D = -\pi C\rho/2D^4 \qquad (2.17)$$
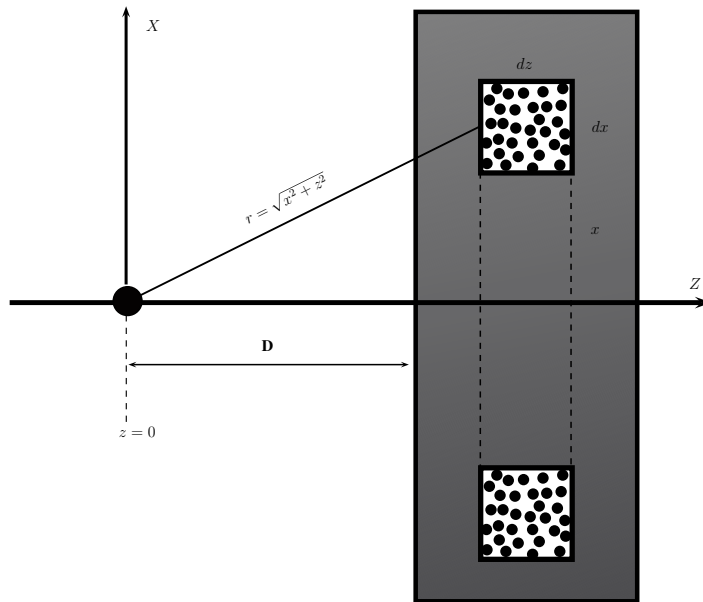
Figure 2.8: Molecule near to vertical surface or wall.
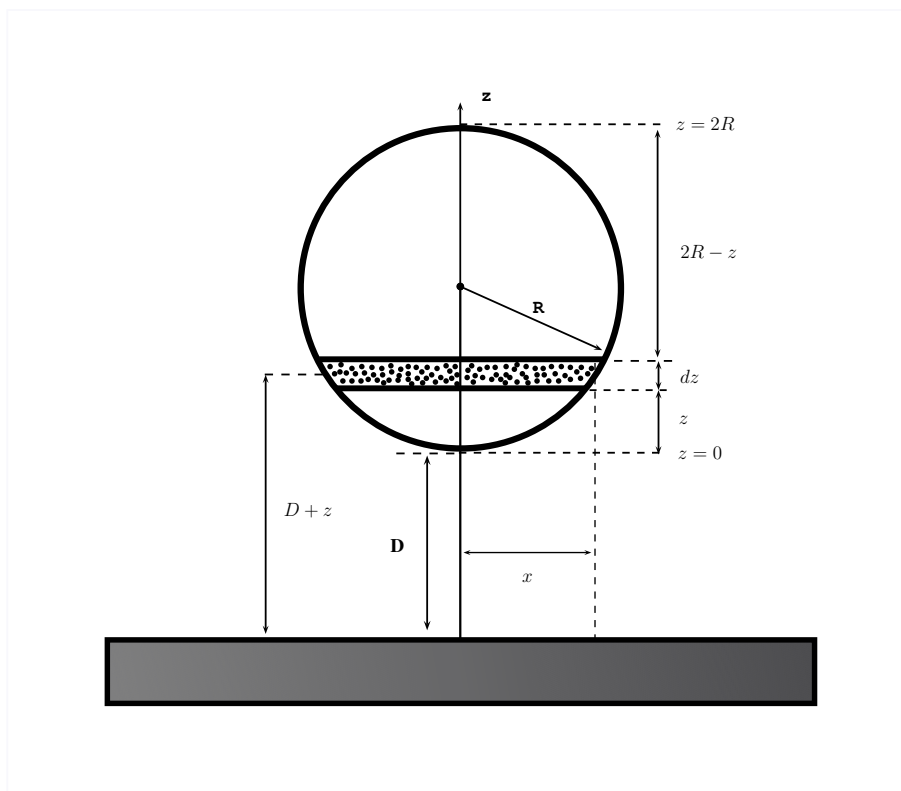
Figure 2.9: Spherical particle near to horizontal surface (R » D).

33

2.5.2 Sphere-surface energy and interaction force

The above analysis can be applied to different object geometry to calculate the adhesive force due to the London's Van der Waals forces. The interaction energy of a micro/nano sphere of radius R and flat surface is shown in Figure 2.9. Thus, from the chord theorem is known that for a circle: $x^2 = (2R - z)z$, the volume of a thin circular section of area πx^2 and thickness dz is therefore $\pi x^2 dz = \pi (2R - z)z dz$. The number of molecules contained within this section is $\pi \rho (2R - z)z dz$, where ρ is the number density of molecules in the sphere. From Equation (2.15) (interaction of a molecule or small sphere with a surface) and since all these molecules are at a distance $(D + z)$ from the planar surface, the total interaction energy is

$$w(D) = -\frac{2\pi^2 C \rho^2}{(n-2)(n-3)} \int_{z=0}^{z=2R} \frac{(2R - z)z dz}{(D + z)^{n-3}} \tag{2.18}$$

If **D** $\ll$ **R**, only small values of z (z $\approx$ D) contribute to the integral, thus

$$w(D) = -\frac{2\pi^2 C \rho^2}{(n-2)(n-3)} \int_0^\infty \frac{2Rz dz}{(D + z)^{n-3}} \tag{2.19}$$

$$w(D) = -\frac{4\pi^2 C \rho^2 R}{(n-2)(n-3)(n-4)(n-5)D^{n-5}} \tag{2.20}$$

which for n = 6 (Van der Waals forces) becomes

$$w(D) = -\pi^2 C \rho^2 R/6D \tag{2.21}$$

The corresponding force is then,

$$F = -\delta w(D)/\delta D = -\pi^2 C \rho^2 R/6D^2 \tag{2.22}$$

Note that the interaction energy is proportional to the radius of the micro/nano sphere and it decays as $1/D$, very much slower than the $1/r^6$ dependence of intermolecular pair interaction.

If $\mathbf{D} \gg \mathbf{R}$, is necessary to replace $(D + z)$ in the denominator of Equation (2.18) by D, then

$$w(D) = -\frac{2\pi^2 C\rho^2}{(n-2)(n-3)} \int_0^{2R} \frac{(2R-z)zdz}{(D+z)^{n-3}} = -\frac{2\pi C\rho(4\pi R^3\rho/3)}{(n-2)(n-3)D^{n-3}} \qquad (2.23)$$

Since $4\pi R^3\rho/3$ is simply the number of molecules in the sphere, the above equation is essentially the same as Equation (2.15) for the interaction of a molecule (or small Sphere) with a surface. Thus, for two spheres of equal radii R whose surfaces are at a small distance D a part (R $\gg$ D), their interaction energy is one half given by Equation (2.20) or Equation (2.21), while for two spheres far apart (D $\gg$ R) the energy varies as $-1/D^n$ as for two molecules. For an intermediate separation (R $\approx$ D) the expression for the interaction potential is more complicated but remains analytic in [60].

2.5.3   Surface-surface energy and interaction force

To calculate the interaction energy of two planar surfaces a distance D apartit is necessary to consider the energy per unit surface area, otherwise for two infinite surfaces, the result will be infinity. Starting with a thin sheet of molecules of unit area and thickness dz at a distance z away from an extended surface of larger area as shown in Figure 2.10 from Equation (2.15) the interaction energy of this sheet with the surface is

$$\frac{-2\pi C\rho(\rho dz)}{(n-2)(n-3)z^{n-3}}$$

Thus, for the two surfaces

$$w(D) = -\frac{2\pi^2 C\rho^2}{(n-2)(n-3)} \int_D^\infty \frac{dz}{z^{n-3}} = -\frac{2\pi C\rho^2}{(n-2)(n-3)(n-4)D^{n-4}} \qquad (2.24)$$

which for $n = 6$ becomes

$$w(D) = -\frac{\pi C \rho^2}{12 D^2} \qquad per \quad unit \quad area. \tag{2.25}$$

The corresponding force is then,

$$F = -\delta w(D)/\delta D = -\frac{\pi C \rho^2}{6 D^3} \qquad per \quad unit \quad area. \tag{2.26}$$

It is important to note that Equation (2.24) and Equation (2.25) are for unit area of one surface interacting with an infinite area of another surface. *In practice this usually amounts to two unit areas of both surfaces, but it is strictly applicable only when D is small compared to the lateral dimensions of the surfaces.* It can be observed from above paragraphs:

First, the interaction energy generally decays much more slowly with distance than it does for two molecules. For instance, the Van der Waals interaction energy between atoms and molecules is of short range and has an inverse sixth-power distance dependence. Nevertheless, the Van der Waals interaction energy between large condensed bodies decays more slowly with distance ($1/D$ for spheres and $1/D^2$ for planar surfaces) increasing its effect over a much longer distance range.

Second, the Van der Waals interaction energy of a small molecule of diameter σ with a flat surface is given by Equation (2.16) as

$$w(D) = -\frac{\pi C \rho}{6 D^3}$$

Therefore, **at contact** the value of distance $D \approx \sigma$ and $\rho \approx \sqrt{2}/\sigma^3$ (corresponding to a close packed solid) that results in

$$w(\sigma) \approx -\frac{\sqrt{2}\pi C}{6\sigma^6} \approx -\frac{0.74 C}{\sigma^6} \tag{2.27}$$
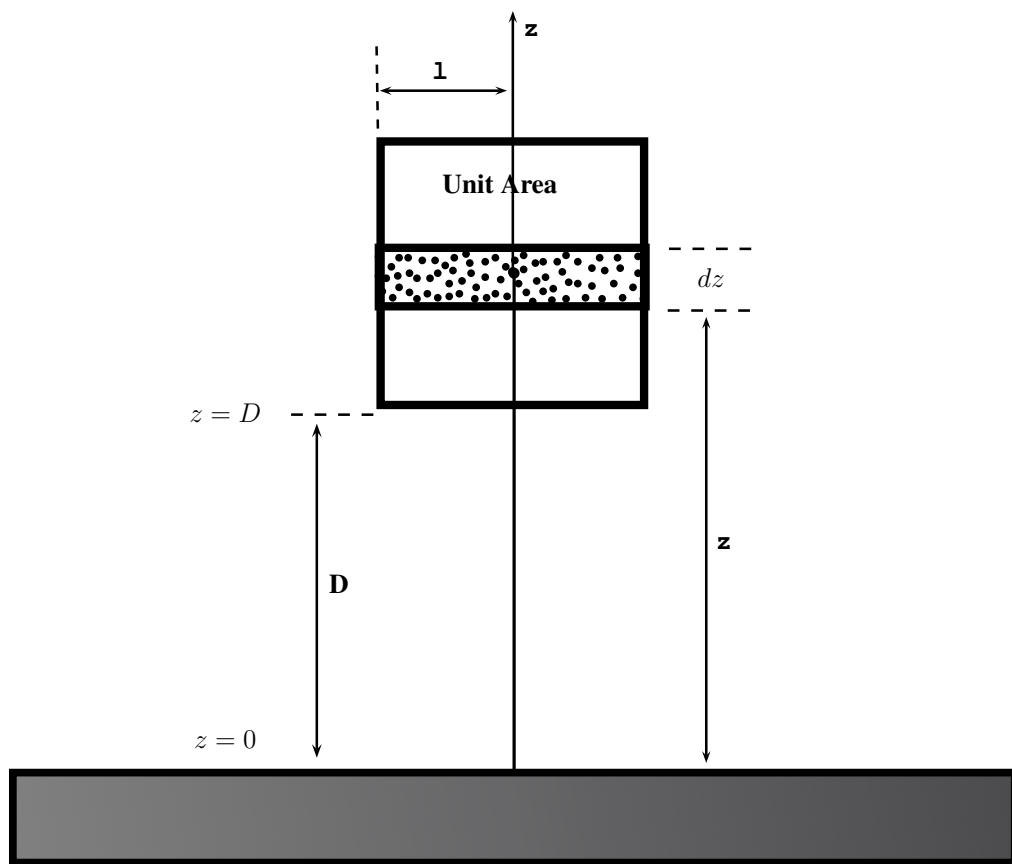
Figure 2.10: Interactive energy for two planar surfaces at distance D apart.

which is of the same order as $-C/\sigma^6$ for two small molecules at contact. In the same way, *for an atomic dimensions sphere* $(R = \sigma/2)$ **at contact with a flat surface** $(D = \sigma)$ Equation (2.21) changes to

$$w(\sigma) \approx -\frac{2\pi^2 C}{12\sigma^6} \approx -\frac{1.6C}{\sigma^6} \qquad (2.28)$$

while for two spheres of atomic dimensions

$$w(\sigma) \approx -\frac{0.8C}{\sigma^6} \qquad (2.29)$$

which again are very close to the *molecule-molecule pair potential* at **contact**. However, once the size of a sphere increases above the atomic dimensions (**i.e.** $R > \sigma$) and if they are in contact ($D = \sigma$). Equation (2.21) becomes

$$w(\sigma) \approx -\frac{2\pi^2 CR}{6\sigma^7} \approx -1.6(2R/\sigma)C/\sigma^6 \qquad (2.30)$$

which reduces to Equation (2.28) only for small radii, of the order $R \approx \sigma/2 \approx 0.1 - 0.2nm$, but increasing linearly with its radius R for larger spheres. Then, for a diameter 2R $\geq$ 0.5 nm a molecule must already be considered as a (small) particle or the strength of its interactions will be underestimated.

Finally, while for two atoms or small molecules the contact interaction energy has no explicit size dependence. it is quite the opposite, between larger particles, when the contact interaction increases linearly with their radius.

2.5.3.1 Work of adhesion and cohesion in vacuum

This is the free energy, or reversible work done, to separate unit areas of two medium 1 and 2 from contact to infinity in a vacuum (Figure 2.11(a) and 2.11(b)).

For two different mediums ($1 \neq 2$), this energy can be defined as the *work of adhesion W_{12}*, while for two identical mediums ($1 = 2$), it becomes the *work of cohesion W_{11}*. If medium 1 is a solid and medium 2 a liquid, then W_{12} is often denoted by W_{SL}. Note that since all mediums attract each other in a vacuum W_{11} and W_{12} are always positive.

2.5.3.2 Surface energy for solids and surface tension for liquids

Equation (2.31) can be used to calculate the surface energies in solids and liquids. For solids γ_1 is commonly denoted by γ_s and is given in units of energy per unit area: J/m^2 (the same as erg/cm^2). For liquids, γ_1 is commonly denoted by γ_L and is usually given in units of tension per unit length: N/m (the same as dyn/cm), which is numerically and dimensionally the same as the surface free energy.

$$\gamma_1 = \frac{1}{2}W_{11} \tag{2.31}$$

Therefore, the free energy in solids and liquids is the change in the surface area of a medium when it is increased by unit area. This is equivalent to separating two half-unit areas from contact (*see* Figure 2.11(b) and Figure 2.11(c)).

2.5.3.3 Inter-facial energy

When two immiscible liquids 1 and 2 are in contact, the free energy change in expanding their 'inter-facial' area by unit area is known as their *inter-facial energy* or *inter-facial tension γ_{12}*. The energies associated with this expansion process may be explained by splitting it in two hypothetical steps: first, unit areas of mediums 1 and 2 are created, and are then brought into contact (Figure 2.11(d) and Figure 2.11(e)). The total free energy change γ_{12} is therefore

$$\gamma_{12} = \frac{1}{2}W_{11} + \frac{1}{2}W_{22} - W_{12} = \gamma_1 + \gamma_2 - W_{12} \tag{2.32}$$

which is often referred to as the *Dupré equation*.

As shown in Figure 2.11(d), this energy is formally the same as that expected on separating two mediums medium 1 in medium 2 (W_{121}) or, conversely, of separating two medium in medium 1 (W_{212}). Thus, the next relation can be held

$$\gamma_{12} = \frac{1}{2}W_{121} = \frac{1}{2}W_{212} \tag{2.33}$$

For a solid-liquid interface, γ_{12} is commonly denoted by γ_{SL}, so that the Dupré equation may be written as

$$\gamma_{SL} = \gamma_S + \gamma_L - W_{SL} \tag{2.34}$$

If only dispersion forces are responsible for the interaction between medium 1 and medium 2, then an approximation could be

$$W_{SL} \approx \sqrt{W_{11}^d W_{22}^d} \approx 2\sqrt{\gamma_1^d \gamma_2^d} \tag{2.35}$$

where γ_1^d and γ_2^d are the dispersion force contributions to the surface tensions. This can provide good results for many hydrocarbon-water interfaces, but it lost accuracy for unsaturated hydrocarbons and for aromatic molecules such as benzene and toluene.

2.5.3.4 Work of adhesion in a third medium

Finally, the energy change arising from separating two mediums 1 and 2 in a medium 3 (*see* Figure 2.11(f)) is given by

$$W_{132} = W_{12} + W_{33} - W_{13} - W_{23} = \gamma_{13} + \gamma_{23} - \gamma_{12} \tag{2.36}$$

2.5.4 Adhesive force in metals

The adhesion force between metallic surfaces is strong. This strong adhesion could be the result of the short-range non-additive electron exchange interactions. These interactions can arise between conducting surfaces at *separations below 0.5 nm* and give rise to so-called *metallic bonds*, as the mobility of electrons in conductive materials is high. Therefore, the **interaction potential energy** w **of two similar metallic surfaces** is defined as

$$w(D) = -2\gamma \left[1 - \frac{(D - D_0)}{\lambda_M} \right] e^{-(D - D_0)/\lambda_M} \qquad per\ unit\ area. \qquad (2.37)$$

where λ_M is some characteristic decay length for metals [61]. Thus, the minimum energy occurs at inter-atomic distance $D = D_0$ where $w(D_0) = -2\gamma$. Typical measured values for metallic contacts are shown in Table 2.2 [3].

Surface energies and adhesive force values of metals are presented by Ferrante and Smith in [62]. Two cases were analysed: first, the case for similar metals when their lattices are not in perfect registry (incommensurate or mismatched lattices), as the contacting lattices are at some time in a twist angle relative to each other due its position. Second, when the metals lattices match perfectly (commensurate or matched lattices). In this case, atoms of two *incommensurate lattices* cannot pack together as closely as two commensurate lattices, and their adhesion energy is often significantly smaller than for *commensurate surfaces*. Summarised values are showed in Table 2.3 [3].

---

[3]See at the end of this Chapter.
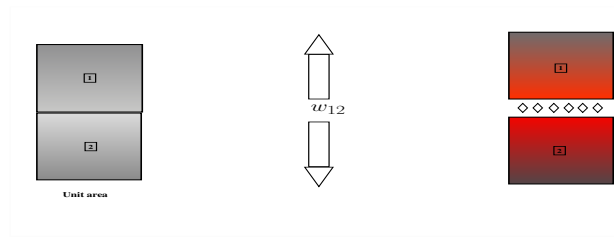
(a) Work of adhesion per unit area w_{12} for separating to surfaces at contact.
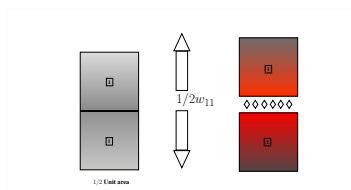
(b) Solid surface: $1/2w_{11} = \gamma_1 = \gamma s$
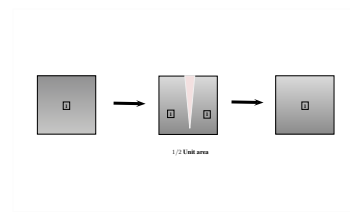
(c) Liquid surface (per unit area): $1/2w_{11} = \gamma_1 = \gamma l$
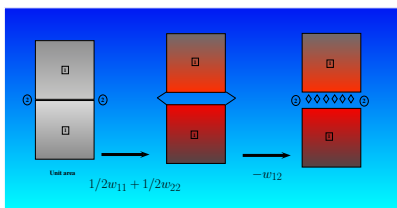
(d) Solid-solid interface in liquid: $\gamma_{12} = 1/2w_{121} = 1/2w_{11} + 1/2w_{22} - w_{12}$
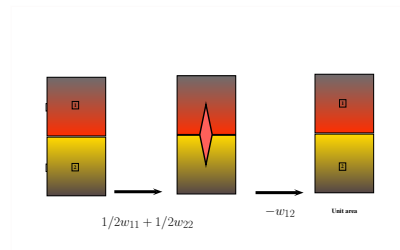
(e) Liquid-liquid interface: $\gamma_{12} = 1/2w_{11} = w_{11} + w_{22} - w_{12}$
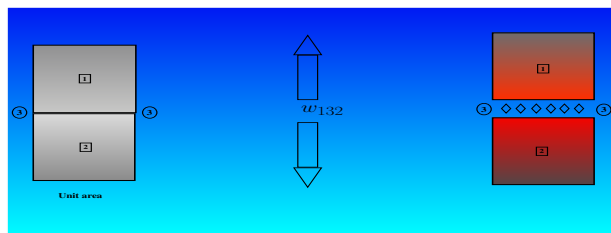
(f) Work of adhesion per unit area in a medium $w_{132} = w_{12} + w_{33} - w_{13} - w_{23}$

Figure 2.11: Work of adhesion per unit area for different medium.

2.5.5 Forces between surfaces with adsorbed layers

The non-retarded Van der Waals force between two surfaces 1 and 1' with absorbed layers 2 and 2' across medium 3 (Figure 2.12) is derived by Israelachvili and Tabor in [63] as

$$F(D) = \frac{1}{6\pi} \left[\frac{A_{232'}}{D^3} - \frac{\sqrt{A_{121}A_{32'3}}}{(D+T)^3} - \frac{\sqrt{A_{1'2'1'}A_{323}}}{(D+T')^3} + \frac{\sqrt{A_{1'2'1'}A_{121}}}{(D+T+T')^3} \right] \qquad (2.38)$$

when $medium1 = medium1'$, $medium2 = medium2'$, and $T = T'$ (symmetrical case), Equation (2.38) can be simplified using combining relations

$$F(D) = \frac{1}{6\pi} \left[\frac{A_{232}}{D^3} - \frac{2A_{123}}{(D+T)^3} + \frac{A_{121}}{(D+2T)^3} \right] \qquad (2.39)$$

At small separations, when $D << (T + T')$, Equation (2.38) becomes

$$F(D) = \frac{A_{2'32}}{6\pi D^3} \qquad (2.40)$$

while at large separations, when $D >> (T + T')$, we obtain

$$F(D) = \frac{A_{1'31}}{6\pi D^3} \qquad (2.41)$$

Thus, *the Van der Waals interaction is dominated by the properties of the bulk or substrate materials at large separations and by the properties of the absorbed layers at separations less than the thicknesses of the layers*. In particular, this means that the adhesion energy is largely determined by the properties of any absorbed films even when these are only a mono-layer thick. Note that with absorbed layers the long-range Van der Waals forces can change sign over certain distance regimes, depending on the properties of the medium [64]. However, for a symmetrical system it can be shown that the interaction is always attractive regardless of the number and properties of the layers.
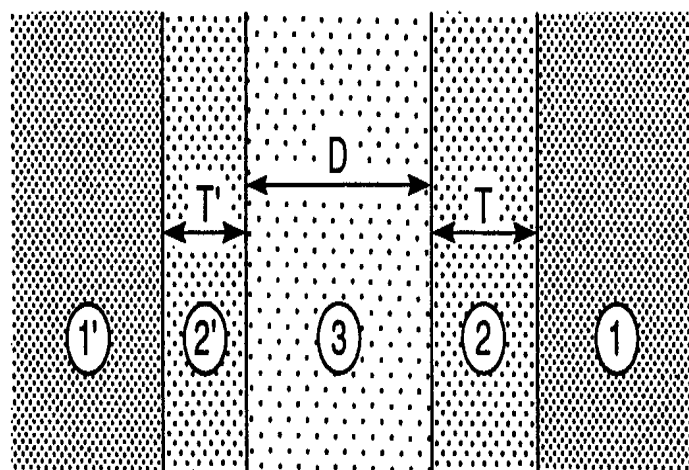
Figure 2.12: Non-retarded Van der Waals force between two surfaces 1 and 1' with absorbed layers 2 and 2' across medium 3 -adapted from [59].

2.5.6 Surface energies of materials in contact

There is always an energy change associated with transferring a molecule from one medium to another for small and higly curved surfaces. This can be expressed in terms of surface $4\pi a^2$ and **inter-facial energy** $4\pi a^2(\gamma_{13} - \gamma_{12})$, being **a** the molecule radius. Therefore, if w is the potential energy of two molecules in contact, then for a planar close-packed surface lattice with three unsaturated bonds per surface molecule, the surface energy is given for one of the derived forms of Equation (3.8) in Section 2.5.1 (see Equation (2.42))

$$\gamma \approx \frac{\sqrt{3}w}{\sigma^2} \tag{2.42}$$

Thus, for an isolated molecule, with 12 unsaturated bonds, its effective surface energy will be

$$\gamma \approx \frac{12w}{2}\left[4\pi\left(\frac{\sigma}{2}\right)^2\right] \approx \frac{1.9w}{\sigma^2} \tag{2.43}$$

while for a cluster of 13 molecules, with seven unsaturated bonds per each of the 12 surface molecules, its effective surface energy will be

$$\gamma \approx 12 \times \frac{7w}{2}\left[4\pi\left(\frac{3\sigma}{2}\right)^2\right] \approx \frac{1.5w}{\sigma^2} \tag{2.44}$$

It can be seen from the above analysis that *the magnitude of the **effective surface energy** γ of a very small cluster or hole, or even an isolated molecule is similar to that of a planar macroscopic surface. This is only true for molecules whose pair potential is additive, and when long-range forces and many-body effects are not important. While this condition holds for Van der Waals substances, it **does not apply to metallic, ionic and hydrogen-bonding compounds**.*

In the case of metals, the high latent heats, melting points, surface energies and electronic conductivities are believed to depend on the correlated (cooperative) interactions of many atoms. Thus, in a very small droplet this can not occur. As a consequence, metal clusters

with less than 15 - 30 atoms lose their bulk metallic properties [59]. In particular, the melting points of small droplets of gold are significantly lower than the bulk value of $1336\,°\mathrm{K}$, falling to $1000\,°\mathrm{K}$ for a cluster of diameter 4 nm and to about $500\,°\mathrm{K}$ for a diameter of 2.5 nm [65]. Note that these modified properties apply not only to isolated droplets but to any highly curved surfaces such as protruding asperities on a rough surface.

2.5.7 Adhesion force between solid particles: The JKR and Hertz theories

The adhesion force of two rigid (incompressible) spheres is simply related to their work of adhesion in a medium 3 W_{132} by

$$F = 2\pi \left(\frac{R_1 R_2}{R_1 + R_2} \right) W_{132} \tag{2.45}$$

This general result is a direct consequence of the Derjaguin approximation [4], and leads to the following special cases in different mediums:

$$
\begin{aligned}
F &= 2\pi R \gamma_{SL} & \text{(two identical spheres in liquid),} & \tag{2.46} \\
F &= 2\pi R \gamma_{S} & \text{(two identical spheres in vacuum),} & \tag{2.47} \\
F &= 4\pi R \gamma_{S} & \text{(sphere on flat surface in vacuum),} & \tag{2.48} \\
F &= 4\pi R \gamma_{SV} & \text{(sphere on flat surface in vapour).} & \tag{2.49}
\end{aligned}
$$

However, particles are never completely rigid (**Hertz** contact theory), as at contact they will *deform elastically* under the influence of any **externally applied load** as well as **the attractive inter-surface forces** that pull the two surfaces together as shown in Figure 2.13(a). Thus, this creates a finite contact area even under zero external load (**JKR** contact theory). Other mechanical contact models are the **Bradley** and the Derjaguin, Muller and Toporov model or the **DMT** model which are far outside the scope of this research.

---

[4]Derjaguin's approximation express the force profile acting between finite size bodies in terms of the force profile between two planar semi-finite walls.
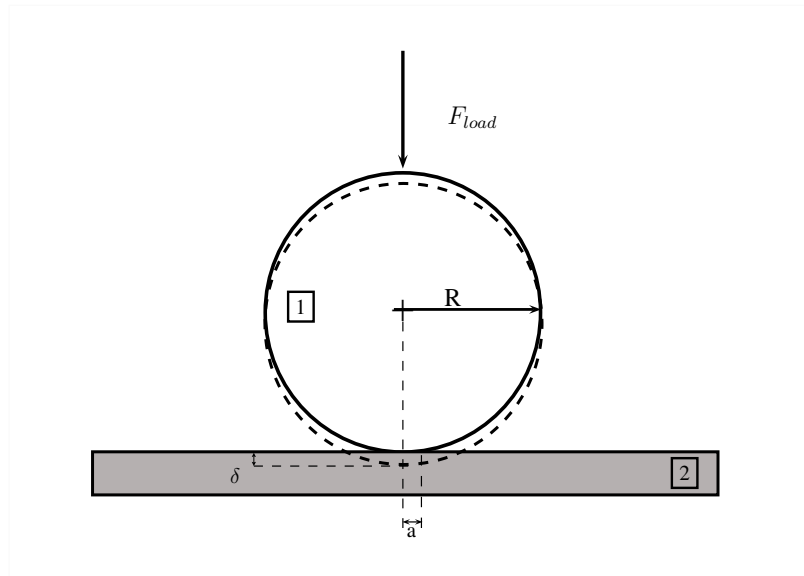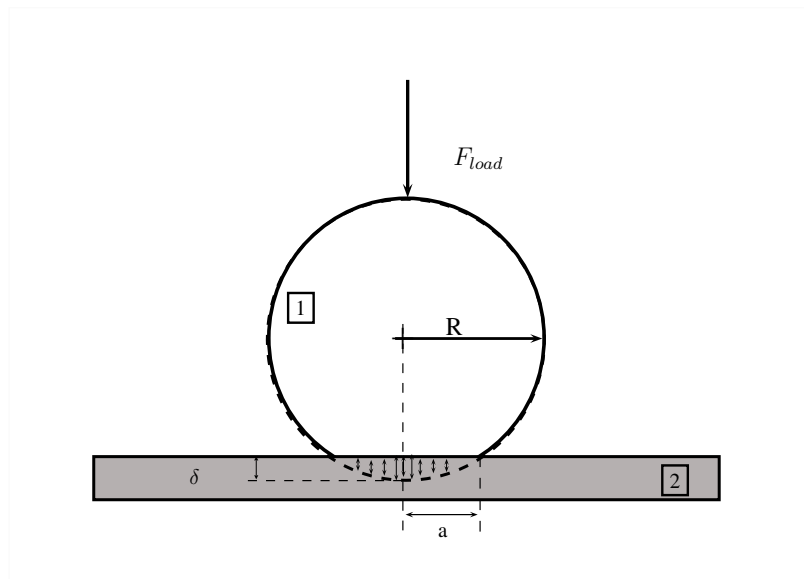
Figure 2.13: Contact models for a sphere and a flat surface. (a) **Hertz** model for elastic objects and (b) **JKR** for elastic objects and considering adhesion in the contact zone.

2.5.7.1 The Johnson, Kendal and Roberts (JKR) contact model

An analysis of adhesion of two spheres in contact which includes the Van der Waals force and the deformation area is presented by the **JKR** theory in [66]. In the case of two spheres of radii R_1 and R_2, elastic moduli K, and surface energy W_{12} per unit area, they will flattened when pressed together under an external load or force F. This flatten circular area or contact area has a radius a given by

$$a^3 = \frac{R}{K}\left[F + 3\pi R W_{12} + \sqrt{6\pi R W_{12} F + (3\pi R W_{12})^2}\right], \; with \; R = R_1 R_2/(R_1 + R_2) \quad (2.50)$$

For a sphere of radius R on a flat surface of the same material as shown in Figure 2.13(b), the value of R_2 is set to be $R_2 = \infty$, $R = R_1$ and $W_{12} = 2\gamma_{SV}$ in the above equation, so that under zero load $F = 0$ the contact radius is finite and given by

$$a_0 = (6\pi R^2 W_{12}/K)^{1/3} = (12\pi R^2 \gamma_{sv}/K)^{1/3} \quad (2.51)$$

Equation 2.50 further shows that under *small negative loads* (F < 0) the solids still adhere until at some negative force they *suddenly jump* apart. This force is given by

$$F_s = -3\pi R \gamma_{SV} \quad (2.52)$$

and an observed *separation occurs abruptly* once the contact radius has fallen to

$$a_s = \frac{a_0}{4^{1/3}} = 0.63 a_0 \quad (2.53)$$

The *central displacement* δ is given by

$$\delta = \frac{a^2}{R}\left[1 - \frac{2}{3}\left(\frac{a_0}{a}\right)^{3/2}\right] \quad (2.54)$$

Another useful equation gives the pressure or stress distribution within the contact circle as

$$P(x) = \frac{3Ka}{2\pi R}(1-x^2)^{1/2} - \left(\frac{3KW_{12}}{2\pi a}\right)^{1/2}(1-x^2)^{-1/2} \tag{2.55}$$

where $x = r/a$.

2.5.7.2 The Hertz contact model

The Hertz equations of contact can be obtained from the **JKR** equations if $w_{12} = 0$. Therefore,

$$Adhesion\,force: \qquad F_s = 0 \tag{2.56}$$

$$Contact\,radius: \qquad a^3 = RF/K \tag{2.57}$$

$$Displacement: \qquad \delta = a^2/R = F/Ka \tag{2.58}$$

$$Presure: \quad P(x) = \frac{3Ka(1-x^2)^{1/2}}{2\pi R} = \frac{3F(1-x^2)^{1/2}}{2\pi a^2} \tag{2.59}$$

From Equation (2.59) if $x = 0$ (the contact's centre) the pressure is $P(0) = \frac{3}{2}F/\pi a^2$, which is 1.5 times the mean pressure across the contact circle.

One difficulty with the **JKR** theory is that it predicts an infinite stress at the edge of the contact circle (at $x = 1$) where the surfaces are expected to bend infinitely sharply though 90°. This non-physical situation arises because the attractive forces between the two surfaces act over an infinitesimally small range. However, these infinities disappear as soon as the attractive force law between the surfaces is allowed to have a infinite range. Considering this breakdown within the last few nanometres of the bifurcation boundary, most of the equations of the **JKR** theory and all equations of the **Hertz** theory have been experimentally tested for molecularly smooth surfaces and have been found to apply extremely well. *The notion that even the simplest adhesion process may not always be reversible, but involves energy dissipation, has profound effects for understanding many adhesion phenomena and also provides a link between adhesion and friction.*

2.5.8   Effect of capillary condensation on adhesion

As the relative humidity (**RH**) increases, vapour will spontaneously condense on surfaces forming meniscuses on the material's surface. The curvature of these meniscuses is related to the relative vapour pressure, p/p_{sat} (or **RH** for water), by the Kelvin equation

$$\left(\frac{1}{r_1} + \frac{1}{r_2}\right) = r_k = \frac{\gamma V}{RT\log(p/p_{sat})} \tag{2.60}$$

where r_k is the Kelvin radius, γ is the surface tension of water, R is the gas constant value, and V is the molar volume. For instance, for a drop of water at 20° $r_k = 0.54$ nm. Figure 2.14 shows the case of a sphere and a surface. If the annular meniscus is at equilibrium ($r_1 = r_2 = r$), then its radius r is small and negative (concave) and x is large and positive (convex). For low humidity, r is small, thus the onset of capillary condensation with increasing **RH** first occurs at small values of r_k in cracks and pores.

The effect of a liquid condensation on the adhesion force magnitude can be calculated using the *Young-Laplace pressure* for a liquid ΔP. This describes the capillary pressure difference sustained across the interface between two static fluids, such as water and air, due to the phenomenon of surface tension. Therefore, if the interface is treated as a surface (zero thickness) $\Delta P = \gamma\left(\frac{1}{R_1} + \frac{1}{R_2}\right)$, where ΔP is the pressure difference across the fluid surface, γ is the surface tension, and R_1 and R_2 are the principle radii of curvature (these measure how the surface bends by different amounts in different directions), then

$$\Delta P = \gamma\left(\frac{1}{R_1} + \frac{1}{R_2}\right) \tag{2.61}$$

$$P = \gamma_L\left(\frac{1}{r_1} + \frac{1}{r_2}\right) \tag{2.62}$$

$$P \approx \frac{\gamma_L}{r_1} \quad \text{since } r_2 >> r_1 \tag{2.63}$$
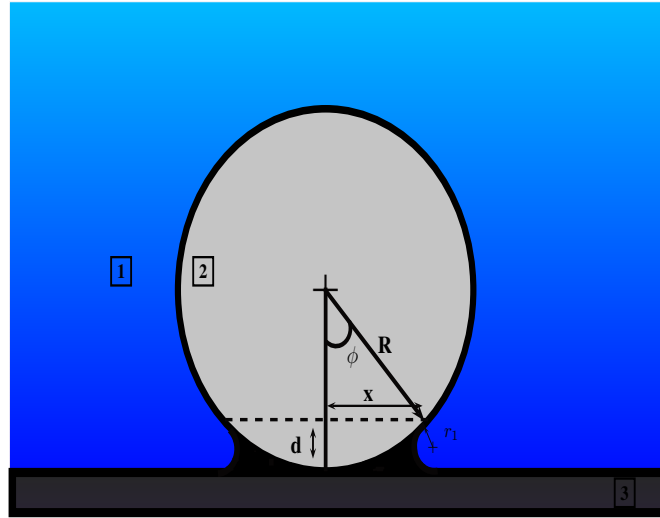
Figure 2.14: Sphere (2) and flat surface (3) at contact influence of meniscus formation in a condensed medium (1), $x = Rsin(\phi)$.
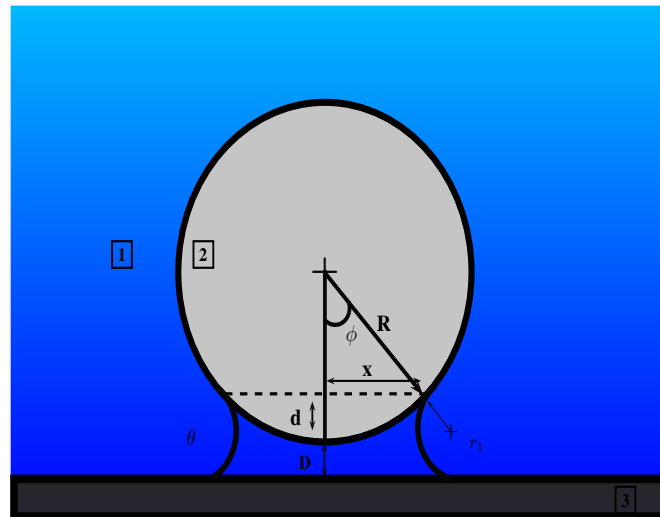
Figure 2.15: Sphere (2) and flat surface (3) at contact influence of meniscus formation in a condensed medium (1) for total surface energy derivation.

The Laplace pressure acts on an area $\pi x^2 \approx 2\pi R d$ between the two surfaces, thus pulling them together with a force $F \approx 2\pi R d(\gamma_L/r_1)$. For small ϕ, $d \approx 2r_1 \cos\theta$, this gives for the Laplace pressure contribution to the adhesion force

$$F \approx 4\pi R \gamma_L \cos\theta \tag{2.64}$$

The additional force arising from the resolved surface tension around the circumference is always small compared to the Laplace pressure contribution except for $\theta \approx 90^o$ when $\cos\theta \approx 0$.

An alternative derivation is to consider how the total surface free energy of the system W_{tot} changes with separation D (see Figure 2.15). For small ϕ,

$$\begin{aligned} W_{tot} &\approx 2\pi R^2 \sin^2\phi(\gamma_{SL} - \gamma_{SV}) + constant + smaller\ terms \\ &= -2\pi R^2\phi^2\gamma_L \cos\theta + constant \end{aligned} \tag{2.65}$$

so that

$$F = -dW_{tot}/dD = +4\pi R^2\phi\gamma_L \cos\theta(d\phi/dD) \tag{2.66}$$

If the liquid volume V remains constant, then

$$\begin{aligned} V &\approx \pi R^2 \sin^2\phi(D+d) - (\pi R^3/3)(1-\cos\phi)^2(2+\cos\phi) \\ &\approx \pi R^2 D\phi^2 + \pi R^3\phi^4/4 \qquad \text{for small } \phi \end{aligned} \tag{2.67}$$

also, if the $dV/dD = 0$, which gives

$$\frac{d\phi}{dD} = \frac{1}{(R\phi + 2D/\phi)} = 4\pi R^2\phi\gamma_L \cos\theta(d\phi/dD) \tag{2.68}$$

Thus, the attractive force between the sphere and the surface due to the liquid bridge is

$$F = \frac{4\pi R \gamma_L \cos\theta}{(1 + D/d)} \qquad (2.69)$$

and the maximum attraction occurs at $D = 0$, where

$$F = F_{max} = 4\pi R \gamma_L \cos\theta \qquad (2.70)$$

which is the same as Equation 2.64. Another important parameter must be included in the above expression. This parameter is the direct solid-solid contact adhesion *force inside* the liquid annulus, Equation (2.45). The final result for a meniscus of radius r_1 (where $R \gg r_1$) is therefore

$$F = 4\pi R(\gamma_L \cos\theta + \gamma_{SL}) = 4\pi R \gamma_{SV} \qquad (2.71)$$

In the absence of any condensing vapour (**i.e.** as $r_1 \to 0$) the above reduces to Equation (2.48): $F = 4\pi R \gamma_S$. For two spheres, R is replaced by $(1/R1 + 1/R_2)^{-1}$ in all the above equations.

Since $\gamma_S > \gamma_{SV}$ the adhesion force should be less in a vapour than in a vacuum. In practice, however one often has to compare γ_{SV_1} with γ_{SV_2}, depending on the relative adsorptions of different vapours from the atmosphere, and the adhesion force in air may *increase* with the relative humidity if γ_{SV_1} (moist air) $> \gamma_{SV_2}$(dry air).

Equation (2.37) shows that the adhesion force in vapour must exceed $4\pi R \gamma_L \cos\theta$. Often $\gamma_L \cos\theta$ greatly exceeds γ_{SL}, whence the adhesion force is determined solely, by the surface energy of the liquid (**i.e.** water) and is then adequately given by Equation (2.70). Equation (2.70) and Equation (2.71) are independent of the meniscus radius r_1. So it is of interest to establish below what radius, or relative pressure, these equations break down [67, 68].

Table 2.2: Surface energies of metals -adapted from [59].

| Material | Transition | temperatures | Surface energy (tension) $\gamma(mJm^{-2})^a$ | | |
	Boiling point $T_B(K)^b$	Melting point $T_M(K)^b$	Just above T_M	Just below T_M	At 300 $^\circ$ K
Metals					
Aluminium	2543	931	700	800	1100
Silver	2223	1233	1000	1200	1500
Coppel	2603	1356	1300	1600	2000
Iron	2773	1803	1500	1800	2400
Tungsten	5273	3653	2500	3600	4400
Semi-conductor					
Silicon	2623	1683	750	$\sim$1100	1400
Weak conductor					
Ice	373	273	75	110	71

[a]Values for solids $(T < T_M)$ are only approximate,
the exact value of γ depends on the crystallographic plane.
[b] At 760 mm Hg.

Table 2.3: Surface energies of metals for commensurate and incommensurate lattices -adapted from [62]

| Type of metal-metal interface | Surface energy $\gamma(J/m^2)$ | |
	Lattices in register (Commensurate)	Lattices out of register (Incommensurate)
Similar materials		
Al(111) - Al(111)	0.715	0.490
Zn(001) - Zn(001)	0.545	0.505
Al(111) - Al(111)	0.550	0.460
Dissimilar materials		
Al(111) - Zn(0001)		0.520
Zn(001) - Mg(0001)		0.490
Al(111) - Mg(0001)		0.505

2.6 Summary

This chapter concentrated on a review of techniques developed using an atomic force microscope (**AFM**) for the manipulation of objects at the nanoscale. Also, this Chapter introduced the concept of manipulation at the nanoscale and explored some areas of current research using the **AFM** as a robotic manipulator. Moreover, a description of the **AFM**'s principle of operation and its capabilities for force analysis involved at the nanoscale was presented. The description summarises methodologies and protocols used for accurate control of the position and orientation of nanoparticles on a surface by means of pushing operations at nanoscale. Finally, supported theory and description of interaction forces that exist at the nanoscale was reviewed.

Chapter 3

Analysis of rolling and sliding motion for pushed objects at the nanoscale

3.1 Introduction

This chapter presents the state of the art of the developed equations of motion of nanoscale objects being pushed for manipulation tasks. The derived set of equations is solved using high accuracy integration techniques. The programming computing language chosen was FORTRAN 77. FORTRAN 77 is one of the most popular languages in the area of high-performance computing. It was also chosen because of its ability to perform in a double precision arithmetic offering robust and high speed calculations. These characteristics are essential and necessary to model object's motions at the nanoscale. The shapes of the analysed nano-objects correspond to nanotubes' and nanobars' geometries. Two motions of nanoscale objects are characterised. They are sliding and rolling. Finally, the supported theory is enhanced when correction on adhesion parameters values are introduced to calculate contact areas on the above mentioned nano-objects.

During the first part of this research presented in this chapter, the case of rolling motion on nanotubes is studied. The proposed analysis will provide insight on answer to the question why should nanotubes roll? and what determines whether rolling or sliding will occur in any

56

given translation? These are two questions that were proposed by Falvo et al. in [69].

The second part of this chapter presents the analysis of motion that corresponds to sliding motion. Sliding motion is a combination of in-plane translations (pure sliding) and in-plane rotations. The sliding motion of nanoscale objects is related to their contact area. The contact area is assumed to be the geometrical region between the nano-object and the surface at contact. The analysis of sliding motion is divided into two parts. The first part corresponds to an object sliding over an smooth surface (**i.e.** zero frictional force). In the second part, the analysis will introduce derived expressions of friction to characterise sliding motion over a rough surface (**i.e.** motion characterised by friction).

3.1.1 Surface energy and adhesion force

Surface energies of materials γ are determined from the intermolecular forces between two molecules or atoms in contact that constitute them. For instance, the interaction energy between two identical objects (surface-surface interaction) obtained by the pairwise summation method is defined as Equation (2.25). On the other hand, if the summation method includes the interactive energy due to atoms in the inner objects, then an additional energy term needs to be added

$$w = -U + A/12\pi D_0^2 \tag{3.1}$$

where **A** is given in terms of the conventional Hamaker constant ($A = \pi^2 C \rho_1 \rho_2$) and U is *the molar lattice energy* or *the bulk cohesive energy* of a *Van der Waals* solid of the atoms with their immediate neighbours at $D = D_0$ as shown in Figure (3.1) and defined as

$$U \approx 7.22 N_0 \left[\frac{3\alpha_0^2 h v}{4(4\pi\varepsilon_0)^2 \sigma^6} \right] \tag{3.2}$$

where σ is now the equilibrium inter-atomic distance in the solid and α_0, h, v, and ε_0 are the same parameters as defined previously in Equation (2.12).

From Equation (3.1), the second (positive) term arises from the unsaturated bonds at the two surfaces. This term is always positive and shows that a free liquid will always tend to minimise its surface energy by minimising its surface area. Therefore, the total energy of two planar surfaces using the pairwise summation of the London dispersion energies between all atoms at a distance D apart (*see* Figure 3.1.(a)) is

$$w = \frac{A}{12\pi}\left(\frac{1}{D_0^2} - \frac{1}{D^2}\right) = \frac{A}{12\pi D_0^2}\left(1 - \frac{D_0^2}{D^2}\right) \qquad per \ \ unit \ \ area. \qquad (3.3)$$

From Equation (3.3), if $D \cong D_0$ (**two surfaces in contact or for a thin film**), then the total surface energy may therefore be written as

$$w = 2\,\gamma(1 - D_0^2/D^2) \tag{3.4}$$

whereas for $D = \infty$ (case of two isolated surfaces), the term $1 - D_0^2/D^2 \cong 1$ and the surface energy w become

$$w = \frac{A}{12\pi D_0^2} = 2\gamma \tag{3.5}$$

or in terms of surface energy

$$\gamma = \frac{A}{24\pi D_0^2} \tag{3.6}$$
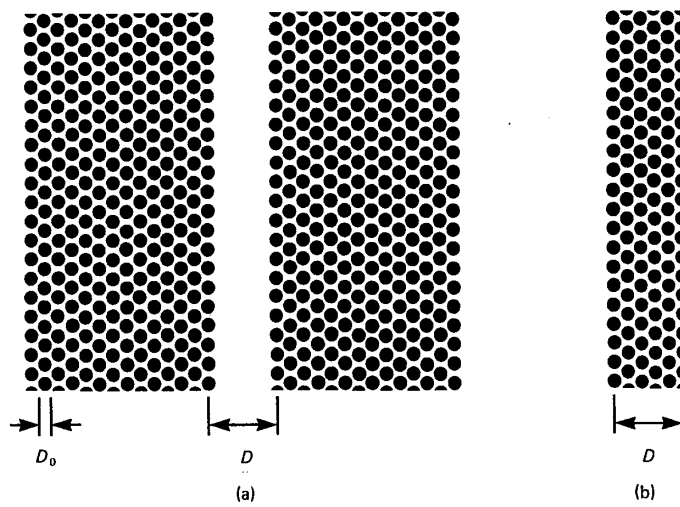
Figure 3.1: (a) Two planar surfaces or half-spaces at a distance D. (b) Two surfaces are close together $D \cong 0$ or for a thin film. -adapted from [59].

With reference to Equation (3.5), *the surface energy γ equals half the energy needed to separate two flat surfaces from contact to infinity $\gamma = w/2$,* Equation (3.5) and Equation (3.6) can provide the value of γ if and only if the inter-facial contact separation D_0 is chosen correctly. However, there are two problems: Firstly, while computing the Hamaker constants by the Hamaker summation method the structured surfaces were transformed into two smooth surfaces, and this *invalidates* the use of Equation (3.6) and Equation (3.5) at inter-atomic distances [60]. Secondly, the continuum Lifshitz theory, which predicts similar values for **A** as does the Hamaker summation method, is also *not expected to apply to atomic-scale distances*. Therefore, if $D_0 = \sigma$ values might be wrong and the problem then arises how to determine D_0 correctly.

3.1.2 Molecular approach to calculate the inter-facial contact distance or cut-off distance D_0

The molecular approach will use the pairwise additivity of individual atoms or molecules. Therefore, for an idealised planar close packed solid each surface atom (of diameter σ) will have only nine nearest neighbours instead of 12. So, *when it comes into contact with a second surface each surface* atom will gain $3w = 3C/\sigma^6$ in binding energy. For a closed-packed solid, each surface atom occupies an area of $\sigma^2 \sin(60^o)$, and the bulk density of atoms is $\rho = \sqrt{2}/\sigma^3$. Thus, the surface energy in terms of the Hamaker constant $A = \pi^2 C \rho^2$, should be approximately

$$\gamma \approx \frac{1}{2}\left(\frac{3w}{\sigma^2 \sin(60^o)}\right) \approx \frac{\sqrt{3}w}{\sigma^2} \approx \frac{\sqrt{3}C\rho^2}{2\sigma^2} \approx \frac{\sqrt{3}A}{2\pi^2\sigma^2} \tag{3.7}$$

$$\gamma \approx \frac{A}{24\pi(\sigma/2.5)^2} \tag{3.8}$$

3.1.3 Corrected surface energy values

Equation (3.8) can be used to approach surface energies if the **cut off distance** D_0 is less than the inter-atomic or intermolecular centre-to-centre distance σ. On the other hand, it has been reported that if $\sigma \approx 0.4nm$, and therefore the *cut-off distance* $D_0 \approx \sigma/2.5 \approx 0.16nm$, the predicted surface and adhesion energies of a variety of compounds are similar to those obtained experimentally. So, if the constant value of $\sigma \approx 0.4nm$ is placed on Equation (3.8) the resulted equation is

$$A \approx 1.9302x10^{-18}\gamma \tag{3.9}$$

where γ can be expressed in $J/m^2, dyn/cm\ or\ erg/cm^2$ units and **A** is giving in joules [J].

Equation (3.9) is a corrected equation of that obtained by Israelachvili [see 59, chap. 11], where the reported constant factor is $2.1x10^{-21}$. As a consequence, values for surface energies γ need to be re-calculated. These new γ values are presented in Table 3.1 which also shows the previous values.

Table 3.1: Corrected surface energies values.

Material (ε) in order to increase ε	Theoretical **A** $(10^{-20}J)$	Surface energy, $A/24\pi D_0^2$ $(D_0 = 0.165nm)$ old values - corrected values	$\gamma(mJm^{-2})$ $Experimental^a$ (20°)
Liquid helium(1.057)	0.057	0.28 - 0.2953	0.12-0.35(4-1.6 K)
n-Pentane(1.8)	3.750	18.3 - 19.4280	16.1
n-Octane(1.9)	4.50	21.9 - 23.3313	21.6
Cyclohexane(2.0)	5.20	25.3 - 26.9402	25.5
n-Dodecane(2.0)	5.00	24.4 - 25.9041	25.4
n-Hexadecane(2.1)	5.20	25.3 - 26.9402	27.5
PTFE(2.1)	3.80	18.5 - 19.6871	18.3
CCl_4(2.2)	5.5	26.8 - 28.4945	29.7
Benzene(2.3)	5.00	24.4 - 25.9041	28.8
Polystyrene(2.6)	6.60	32.1 - 34.1934	33
Polyvinyl chlorde(3.2)	7.80	38.0 - 40.4104	39
Acetone(21)	4.10	20.0 - 21.2413	23.7
Ethanol(26)	4.20	20.5 - 21.7594	22.8
Methanol(33)	3.60	18 - 18.6509	23
Glycol(37)	5.60	28 - 29.0126	48
Water(80)	3.70	18 - 19.1690	73
H_2O_2(84)	5.40	26 - 27.9764	76
Formamide(109)	6.10	30 - 31.6030	58

3.2 Rolling motion

When the position of the force is not through the object's centre of mass the force will produce a moment on the nano-object. This moment could produce either rolling or sliding motion. During experimental manipulation at the nanoscale it was observed that the manipulated nano-objects were rolling or sliding. In addition, the geometry of the nano-object could also play an important role influencing the resulted motion. Therefore, objects with cylindrical or spherical shape have more tendency to roll and objects with rectangular shape can easily slide.

3.2.1 Equations of rolling motion of nanotubes on a rough surface

Cylinder geometry is found in nanoscale elements such as **CNT**, **MWCNT**, **nanowires** and **nanorods**. Rolling resistance is directly related with contact deformation of the surface under a rolling load. In contact deformation, two different scenarios are possible: nanotube deformation over a rigid surface and rigid nanotube over a deformed surface. *Static frictional force f_s* is assumed to keep the nano-object in rolling motion. If its magnitude is higher than the pushing/pulling magnitude force, then the moment caused by it will turn the nanotube following the moment's laws.

3.2.1.1 CNT, MWCNT and Nanorod rolling motion in a rough horizontal plane

For instance, the analysis of rolling motion for a multi walled carbon nanotube **MWCNT** is shown in Figure 3.2. In general, the analysis of forces is simplified assuming a rigid and homogeneous **MWCNT** of radius *r* with mass *m*. It also represents a resultant force **F** parallel to the plane of motion acting upon it to cause the nano-object's motion. Force moments due to the friction and pulling/pushing force are taken about the nanotube centre of mass **C.M.**. Otherwise, accuracy in the analysis is compromised. A further discussion about how to choose the reference point of the moments in rolling motion can be found in [70].

In particular to the diagram of forces shown in Figure 3.2. A set of dynamic equations and its parameters definitions to describe the **MWCNT** for rolling motion are

$$\Sigma F_T = \qquad F - f_s \qquad = m\overline{a}_x \qquad (3.10)$$

$$\Sigma F_N = \quad N - (mg + F_{VdW} + F_{adhesion}) \quad = 0 \qquad (3.11)$$

$$\Sigma M_{C.M.} = \qquad F \times h + f_s \times r \qquad = I_{C.M.}\alpha_r \qquad (3.12)$$

where F is the resultant force being applied to the nano-object at point Q, f_s is the static frictional force, m is the mass of the nano-cylinder which is calculated from the relationship $\rho = m/V$, where ρ is the material density and V is its geometric volume, $\overline{a}_x$ is the linear acceleration of the **MWCNT** centre of mass, N is the normal force at the contact point between the plane and the **MWCNT**, g represents the constant of gravity of Earth taken as $9.81\ [m/s^2]$, F_{VdW} is the Van der Waals interaction force between the **MWCNT** object and the plane of motion, h is the distance between the **MWCNT** centre of mass **C.M.**, r is the **MWCNT** radius, $I_{C.M.}$ is its inertia moment equal to $1/2mr$ and α_r is its rolling angular acceleration.

Solving previous set of equations for *the static friction force f_s* will provide the true motion of the **MWCNT**. To start the analysis described by the above equations, pure rolling motion is first assumed. Thus, the moment magnitude due to the static frictional force is bigger than the moment magnitude of the applied force. Also, the linear acceleration of its centre of mass $\overline{a}_x$ is related to the rolling angular acceleration α_r by $\overline{a}_x = r\alpha_r$.

Then, substituting this relation into Equation (3.12)

$$F \times h + f_s \times r = \frac{1}{2}mr\bar{a}_x \tag{3.13}$$

and simplifying,

$$\frac{2Fh}{r} + 2f_s = m\bar{a}_x \tag{3.14}$$

Equating the left-hand sides of Equation (3.14) and Equation (3.10),

$$\frac{2Fh}{r} + 2f_s = F - f_s \tag{3.15}$$

Thus, solving for the *static frictional force* f_s,

$$f_s = \frac{1}{3}F\left(1 - 2\frac{h}{r}\right)$$

$$\tag{3.16}$$

The relationship expressed by Equation (3.16) is analysed in detail assuming three possible conditions about the position of the pushing force (point Q in Figure 3.2). Figure 3.3 shows the graphic generated by Equation (3.16) showing different phases of the static frictional force f_s described below.
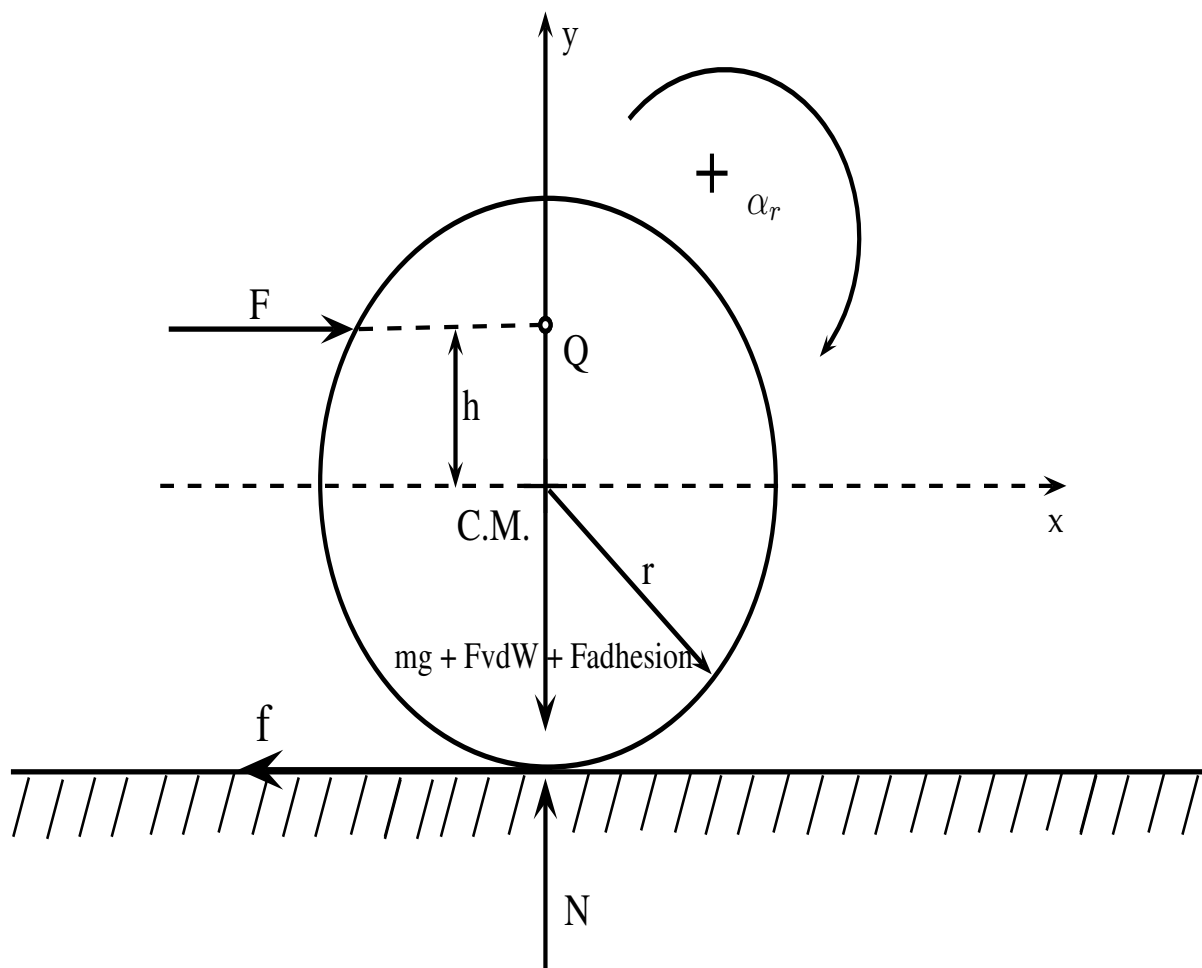
Figure 3.2: Free-body diagram for a rigid **MWCNT** resting on a horizontal plane.

Firstly, in the case when the pushing force **F** is applied at the point located in the middle of the **MWCNT** object's centre of mass to half-top **MWCNT**'s circumference (**i.e.** $h = \frac{1}{2}r \cong 0.675[nm]$). Substituting the value of h in Equation (3.16) will result in a magnitude of the *static frictional force* f_s equal to zero. From Equation (3.10) and Equation (3.12) a value of $f_s = 0$ indicates that the tangential and rolling accelerations will change according to the force and moment magnitude of the pushing force **F** respectively. As a consequence, the **MWCNT** will experience a combination of rolling and sliding motion.

Secondly, the case when the pushing force is located at the top of the **MWCNT** (**i.e.** $h = r = 13.5[nm]$). In this case, replacing $h = r$ in Equation (3.16) will give the value of the *static frictional force* equal to

$$f_s = -\frac{1}{3}(F)$$

The static frictional force f_s has now reversed itself and acts to the right. To determine the resulted **MWCNT**'s motion, the f_s value is then replaced in Equation (3.12)

$$F = \left(\frac{3}{4}\right)m\alpha_r \tag{3.17}$$

Equation (3.17) is satisfied if and only if α_r is positive, as the applied parallel force **F** should be in the same direction as the nano-object's movement (clockwise rolling *see force diagram on Figure 3.2*). Therefore, the **MWCNT** will keep rolling to the right. Thus, the effect of the reversed static frictional force is to change the static frictional moment direction (anti-clockwise), decreasing the **MWCNT**'s acceleration and favouring the conditions to start sliding motion.
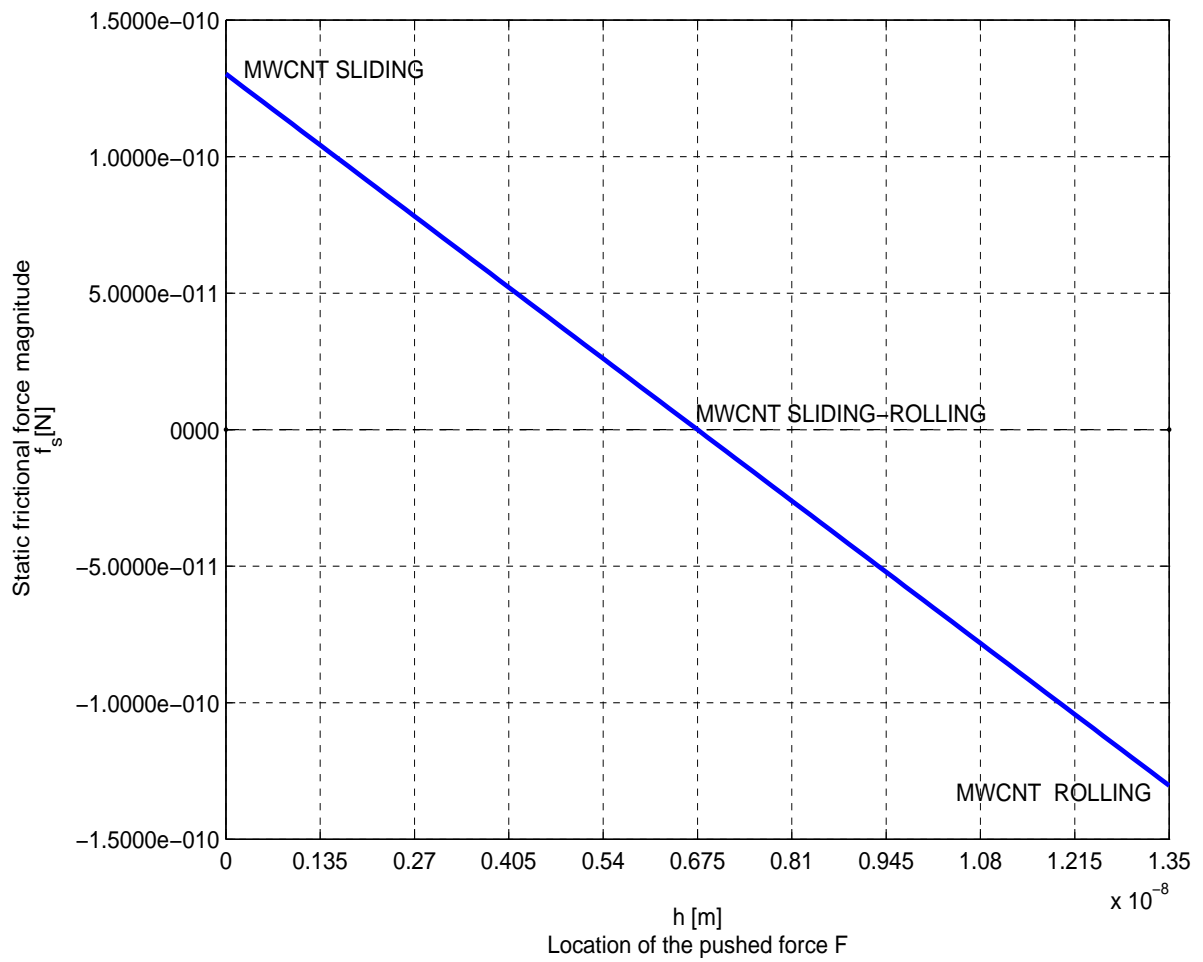
Figure 3.3: Different phases of the magnitude of the static frictional force f_s versus differ-ent locations of the pushing force **F** using a rolling frictional coefficient $k = 0.6$ [nm] for a **MWCNT** of length 590 [nm] and average radius of 13.5 [nm].

Finally, assuming that the location **h** of the applied force **F** is applied through the **MWCNT**'s centre of mass (**i.e.** $h = 0$) and eplacing this value in Equation (3.16)

$$f_s = \frac{1}{3}(F) \tag{3.18}$$

From Equation (3.18), f_s is a function of the pushing force **F** by one third of its magnitude acting to the left direction. Thus, as soon as the maximum possible value of the static friction force is exceeded, the *MWCNT will slip*. A new assumption then must be made, namely, that the static frictional force f_s will achieve the next phase, the *kinetic phase* (sliding motion). Moreover, pushing below the **MWCNT**'s mass centre the static frictional force magnitude will have a tendency to increase favouring the motion as *pure rolling*.

The kinetic frictional force f_k is the opposite force to that acting when a nanotube slides. The *kinetic frictional force* is defined by Coulomb's friction law. For Coulomb's friction law, the magnitude of the f_k is equal to the product of the coefficient of friction μ and the normal force N. The normal force N is now a function only of nanotube's weight and attractive Van der Waals force F_{VdW}. This is because there is no detachment involved on the surfaces in contact. Therefore, the dynamic equations of sliding motion need to be developed separately.

Generally speaking, substituting f_k in the rolling equations of motion Equation (3.10) and Equation (3.12) can be used to provide an idea about the motion of nanotubes. It should be noted that no detachment is involved during sliding. Thus, the modified equations of motion are re-written in terms of f_k as:

$$\Sigma F_T = \quad F - \mu N \quad = m\bar{a}_x \tag{3.19}$$

$$\Sigma F_N = \quad N - (mg + F_{VdW}) \quad = 0 \tag{3.20}$$

$$\Sigma M_{C.M.} = \quad F \times h + \mu N \times r \quad = I\alpha_r \tag{3.21}$$

Equation (3.19), Equation (3.20) and Equation (3.21) indicates the existence of both sliding displacements (linear acceleration $\overline{a}_x$) and in-plane rotations (angular acceleration). Sliding motion and in-plane rotations can be defined about a static point in the plane of motion called the *instantaneous centre of rotation* **iCOR**.

3.3 Determining the dimensions of the contact area

The contact area between cylindrical nano-particles (**i.e.** MWCNTs) is assumed to be a finite rectangle of width k and length L (**i.e.** nanotube length), where $L >> k$. The value of k is closely related to the surface adeshion energy γ of the involved materials at contact. Therefore, by combining the corrected values of γ and the continuum models for mechanical contacts, the deformation value of k (width) can be obtained. On the other hand, the contact dimensions for the nanobar corresponds to their given measured parameters.

3.3.1 Analysis of the static frictional force using different frictional rolling coefficients

Figure 3.4 shows the static frictional force for different frictional coefficients k. Using different values of k, the frictional force behaviour is consistent with the graphic shown in Figure 3.3. The minimum magnitude of the pushing/pulling force is determined by using the model of rolling frictional force when the **MWCNT** is deformed. Therefore, the relation $f_s = Wk/r$ will provide the minimum value of the force to be applied to generate the nanotube roll over the surface, where W corresponds to the total load acting between the **MWCNT** and the surface, r is the radius of the MWCNT and k is the half length of the deformed cylinder width contact.

In particular to the proposed analysis, the total load takes into consideration the total inter-molecular interaction forces during rolling of the nanotube over the plane. So, the proposed total load of the nanotube is defined as $(mg + F_{vdw} + F_{adhesion})$. The adhesion force $F_{adhesion}$ is due to the surface energy generated as rolling motion involves the separation of surfaces in contact. The Van der Waals forces F_{vdw} is the force due to the nanotube interaction with the surface and the nanotube weight mg represents the interaction that the gravitational force acts over it.

The value of the rolling deformation k is obtained using the **JKR** theory of contact defined by a cylinder and a surface [71] . Thus, using equation $W = [(3\pi K a^2 l/8R - P)]^2/(6\pi K a l^2)$ described in [72] where W is the adhesion energy of the two solids, K is the elastic modulus at contact, a is half length of the width deformation, l is half length of the nanotube length, R is the nanotube radius, P is the pressed contact force per unit length normal to the plane of contact (z direction). Thus, the length of the deformation value $k = 2a$ (width) of approximatly 3 [nm]. Using this value as a maximum width deformation, the minimum pushing force is calculated as: $F \approx f_s + 1\% f_s$, which can provide a value of its magnitude at different deformation values varing from zero (zero deformation) to the maximum of 3 [nm].

The values obtained shown in Figure 3.4 related to a deformation value of k with a *static frictional force*. It can be seen that for a big deformation k, the value of the *static frictional force* increases. The increment in this value is due to that in the contact area where the adhesive forces became dominant. Therefore, this increases the surface energy in order to separate the surfaces in contact by increasing the work of adhesion favouring the motion as sliding.
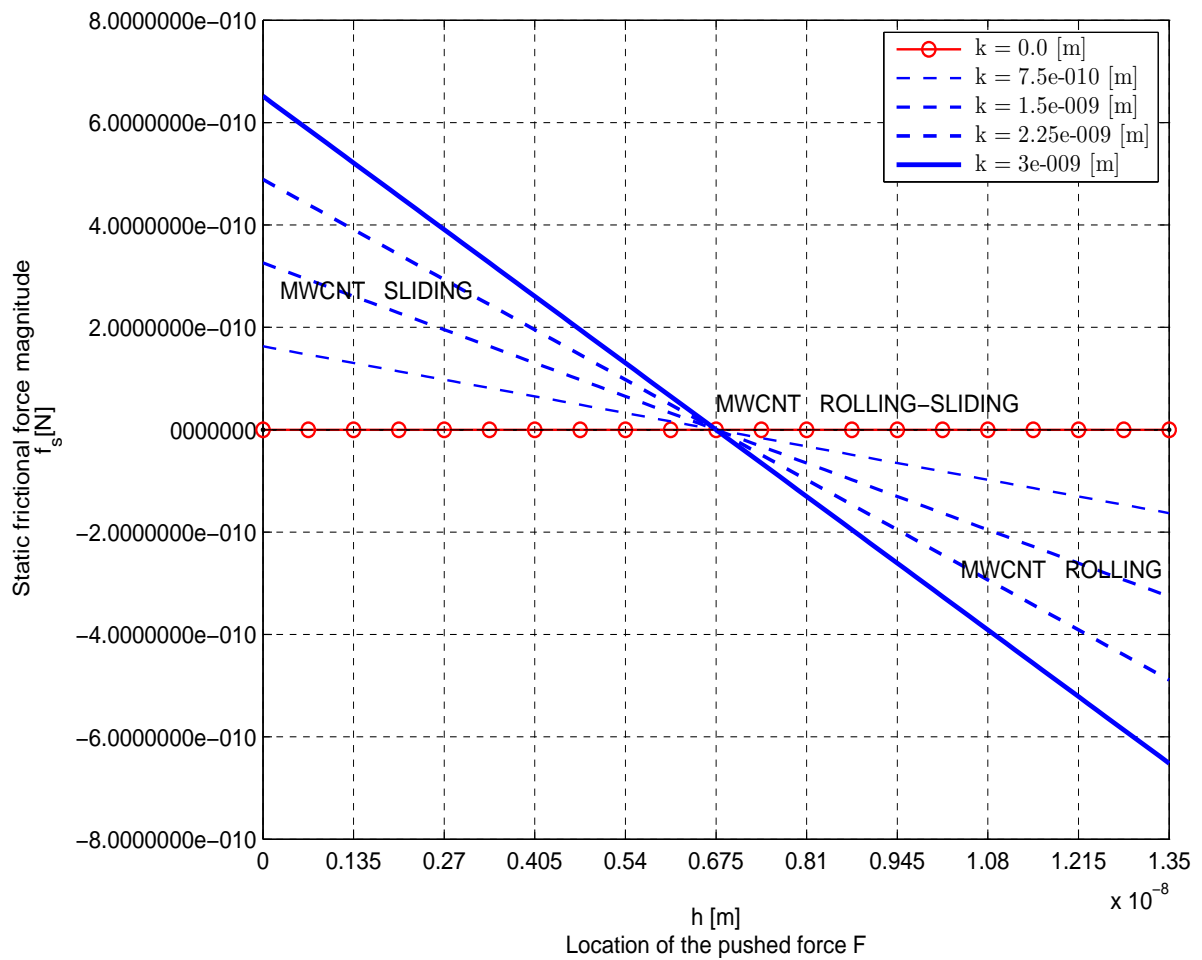
Figure 3.4: Magnitude of the static frictional force f_s versus locations of the pushing force **F** for different values of its rolling frictional coefficient k for a **MWCNT** of length 590 [nm] and average radius of 13.5 [nm].

3.4   Sliding motion

Sliding motion is the relative motion between two surfaces with reference to one fixed point. The motion could occur when one surface is fixed while the other is in motion or when both are moving in opposite directions. Therefore, the work of adhesion is minimised to have no influence on motion. In this research, the case of a mobile surface moving over a fixed surface is investigated. The analysis is for a nanobar using a proposed model where the adhesion force is excluded from the total load. As previously mentioned, a rectangular shape (nanobar) has a more stable sliding movement than nanotubes. In addition, the work of adhesion is minimal due to the non-separation of surfaces. Furthermore, the analysis defines the area of contact between the nanobar and the surface by accurate integrals. The model can be used to describe the motion of nanotubes going into sliding motion by modifying some of its parameters such as the moment of inertia and pressure distribution.

3.4.1   Equations of motion of nano-objects sliding on a smooth surface

This section derives the equation of motion for a rectangular nanobar sliding on a smooth flat surface under the action of a constant pushing force $\mathbf{F}$. Using the coordinate system as shown in Figure 3.5 to re-solve for motions in x and y directions and taking moments about the nanobar centre of mass (**C.M.**) its in-plane motion is characterised. So, the obtained group of second order differential equations absent of frictional forces are

$$m\ddot{x} = F\cos(\beta) \tag{3.22}$$

$$m\ddot{y} = F\sin(\beta) \tag{3.23}$$

$$I\ddot{\theta} = F \times d\cos(\theta - \beta + \phi) \tag{3.24}$$

where m is the mass of the nanobar, I is the inertia moment of the nanobar about it's centre of mass, $\mathbf{F}$ is the applied force, θ, β, ϕ and d are the geometrical parameters as defined in Figure 3.5.

73
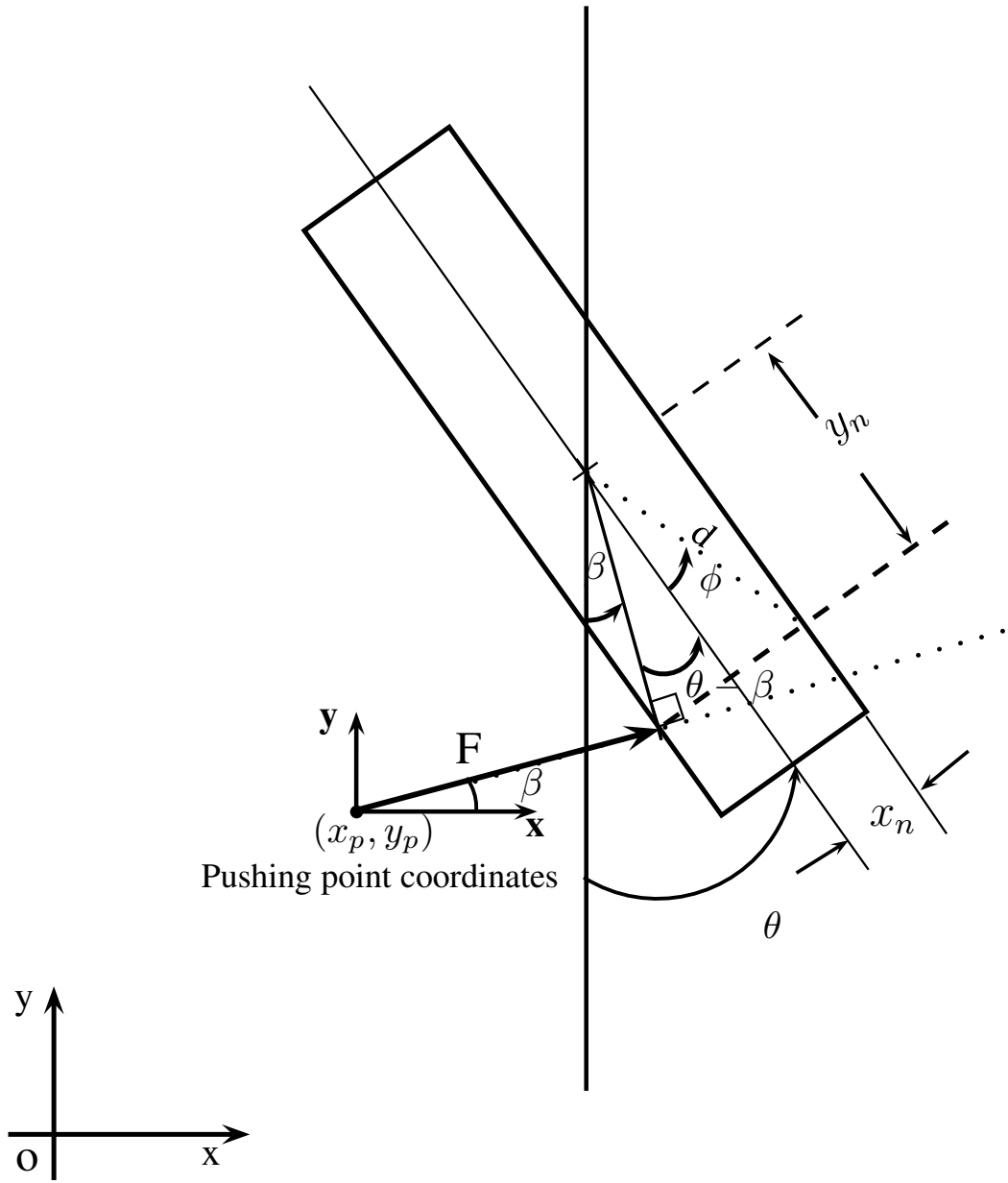
Figure 3.5: Geometrical parameters definition to model the dynamic of the nanobar being pushing at coordinates (x_p, y_p) by a force $\mathbf{F}$.

The group of second order differential equations (Equation (3.23) to Equation (3.24)) is a non-linear system of equations and has to be solved numerically by integration techniques.

3.4.2 Numerical integration routine

The numerical solution of one or more high-order *ordinary differential equations* (**ODE**) is obtained by reducing it's order. Thus, the system of equations can be represented in the form of one set of *n* simultaneous first-order differential equations of the form

$$\frac{\delta y_i(x)}{\delta x} = f_i(x, y_1, y_2, y_3, ..., y_n) \quad i = 1, 2, 3, ..., n \tag{3.25}$$

Equation (3.25) is called the canonical form of the differential equation system. The canonical form is achieved using a series of intermediate variables. For instance, the second order equation

$$\ddot{y} + q(x)\dot{y} = r(x)$$

can be written as two first order equations

$$\dot{y} = z(x)$$
$$\dot{z} = r(x) - q(x)z(x)$$

where z is a new variable (intermediate variable). Solving a group of second order differential equations using this technique, the problem is then reduced to solving a group of first order differential equations. The problem of solving first order differential equation belongs to the category of *initial value problem*. For an *Initial Value Problem* (*IVP*) all the y_i's are given as the starting value x_{t_0} (system's initial conditions), where $t_0 = 0.0[sec.]$ and it is required to find the y_i's at some point final x_{t_f}, where $t_f = final\ time$.

Thus, using the technique described above the reduction of the set of Equation (3.23) into a first order set of coupled equations are

$$
\left.
\begin{aligned}
m\dot{V}_x &= F\cos(\beta) \\
\dot{x} &= V_x \\
m\dot{V}_y &= F\sin(\beta) \\
\dot{y} &= F\cos(\beta) \\
I\dot{\omega} &= F \times d\cos(\theta - \beta + \phi) \\
\dot{\theta} &= \omega
\end{aligned}
\right\}
\tag{3.26}
$$

where V_x, V_y and ω are the new variables introduced to reduce the **ODE** order. The values of the new introduced variables are the components of the nanobar's linear speed in the x and y directions and it's angular velocity, respectively.

To solve the reduced set of first order **ODE** equations (Group of Equations (3.26)) a fast, robust and high accuracy numerical technique is needed. The three major numerical techniques to solve initial value problems (*IVP*) for a set of ordinary differential equations are: Runge-Kutta, Richardson extrapolation and predictor corrector methods. In this research, the Richardson extrapolation method was used to produce a higher accuracy method called the **Bulirsch-Stoer Method** [73].

The **Bulirsch-Stoer method** is the result of combined a Richardson extrapolation method with a particular way of taking individual steps (the modified midpoint method) and a particular kind of extrapolation (rational function extrapolation). The **Bulirsch-Stoer method** is coded using the FORTRAN programming language.

76

3.4.2.1 Results from simulation

This section summarises the results of simulation when the nanobar is pushed under different conditions. Simulated nanobar dimensions are taken from Wiley et al. [74]. Smooth surface motion is similar to having the nanobar moving at space. For instance, the simulated nanobar dimension's are: 100[nm] x 55[nm] x 50[nm] length, width and height, respectively. Eight different cases are simulated for a different initial nanobar orientation sliding on a smooth surface. The cases corresponds to a initial orientation of: $\theta_1 = -0.5$[rad], $\theta_2 = 0.0$[rad], $\theta_3 = 0.5$[rad], $\theta_4 = 0.75$[rad], $\theta_5 = 1.25$ [rad], $\theta_6 = 1.50$ [rad], $\theta_7 = 1.02$ [rad], and $\theta_8 = 0.0$ [rad], respectively as described below.

Figure 3.6 shows the eight cases simulated for different inital angles θ_i , $i = 1, 2, 3 \ldots 8$. The set of parameters for all simulations are: x_n= 27.5000E-09[m] y_n= 45.0000E-09[m], cm_x= 0.00E+00[m] cm_y= 0.00E+00[m], $V_{x_0} = 0.00$E+00[m/s], V_{y_0}= 0.00E+00[m/s], ω_0= 0.00E+00[rad/s], m= 0.623425E-18[kg]. Where m is the nanobar mass. x_n, y_n are the co-ordinates of the application force F. cm_x and cm_y are the coordinates of the nanobar **C.M.**. V_{x_0},V_{y_0} are the initial conditions of velocity in x, initial velocity in y, and ω_0 the initial angular velocity of the nano-object.

In addition, Figure 3.6 shows an oscillating behaviour of the nanobar. Oscillating behaviour could be explained in terms of rotational energy $E_\omega = 1/2\, I_G\omega^2$ and the nano-objects symmetry. The rotational energy E_ω is the energy generated as the force turn the nano-object and it will gain angular speed. However, the nano-object will go to zero rotation when the resulted applied force is going through the object's centre of mass **C.M.** (translation). The Energy due to the sliding motion (translation) is defined as $E_{\dot{x}} = 1/2\, mV_x^2$. Therefore, at the instant that the applied force goes trough the centre of mass **C.M.** its initial speed is zero and its final linear speed is more likely to be an impulse response.
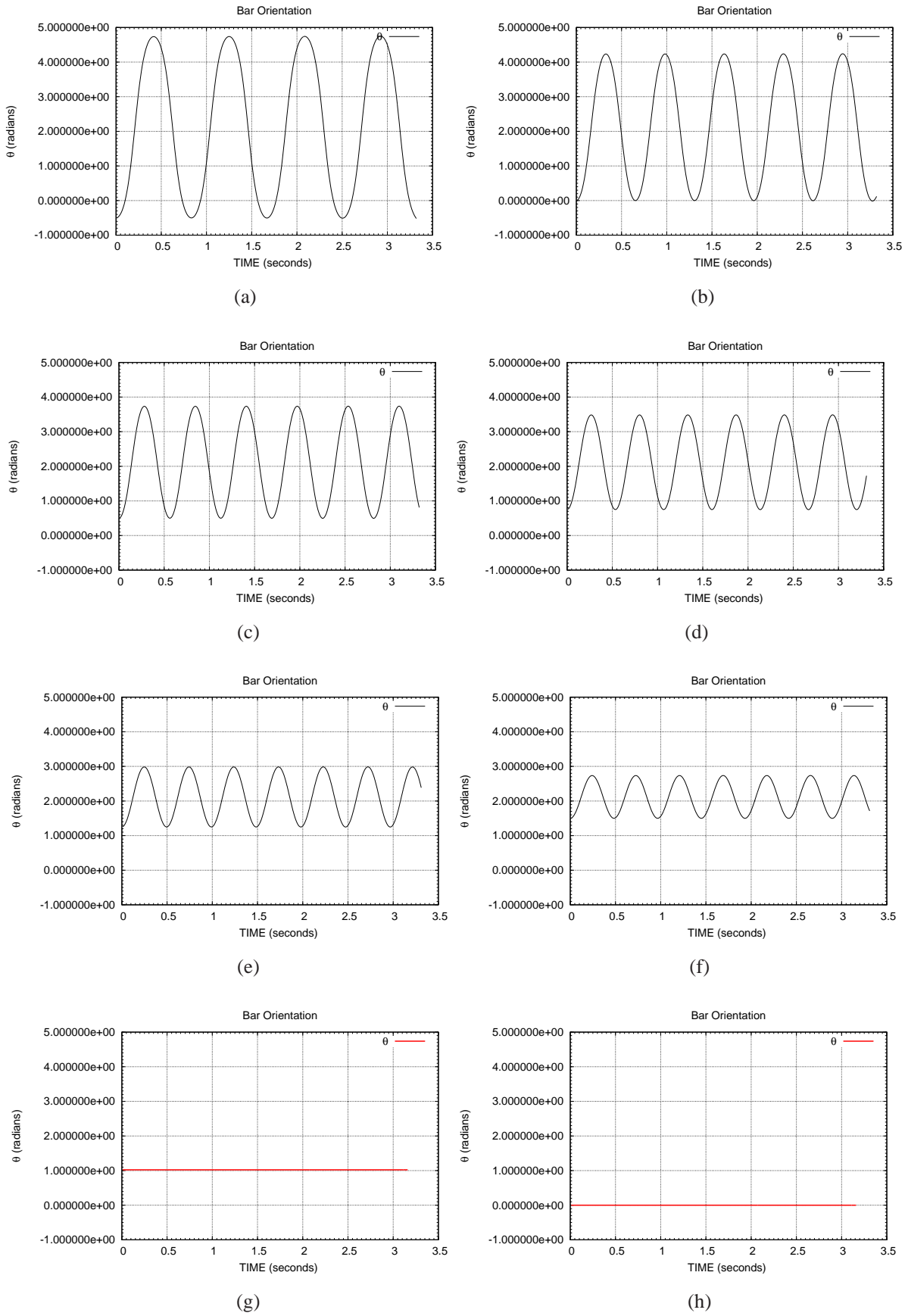
Figure 3.6: Simulated cases for a nanobar being pushed.

This impulse response is directly related to the linear distance achieved, which is generally very small. Also, this implies that forwards translation will move the application force location at the point which the object will be rotating one more time. As a result, there is still enough rotational energy that will keep the nano-object in its rotational motion. On the other hand, the only resistance that the body can experience under these conditions is due to its mass, which in terms of rotational motion is the moment of inertia $I_{C.M.}$ of the nanobar. The nano-object's moment of inertia produces the only rotational resistance. When the mass and the inertial moment values are calculated for the nanobar mentioned above, it was observed that both translational and rotational energy are function of their linear and angular speed respectively. Comparing these values results in greater values for angular speed than linear speed. As a consequence, the energy to keep the nanobar in motion is consistent with the main energy supplier which corresponds to the rotational energy E_ω.

In terms of the objects symmetry, if the action line of the applied force passes over the **C.M.** the force will try a different point of application this time in inverse mode. Then, as the energy stored has to be the same as that consumed. The nano-object's motion will not stop until the same amount of energy will is applied, in other words, until it achieves the same induced moment. This could explain the constants amplitudes shown through the different simulations and also, their different magnitudes.

In Figure 3.6(a) the nanobar was initially at a negative angle and, the amplitude of oscillation is greatest. This is due to the fact that the nanobar has more time to accelerate and thus achieve a higher angular momentum. In Figure 3.6(b) the nanobar was initially at zero angle (vertical position). A decrease in magnitude of the amplitude of oscillation was observed. Following decreases in this amplitude are shown in Figures 3.6 (c) - (g). This can be explained in terms of the nanobar oscillation period. Thus, the nanobar will take less time to achieve its oscillating period as the initial angle is bigger.

3.4.2.2 Special case: Action line of the pushed force passing through the nanobar's centre of mass

Figure 3.6(g) shows the special case when during the manipulation of the nanobar the line of action of the pushing force passes through the nanobar's **C.M**. This special angle corresponds to the values of $\theta_{transation} = \pi/2 - \arctan(x_n/y_n) \cong 1.022246$[rad]. Thus, the nanobar will slide keeping the same angle (orientation) as there is no moment which provides rotation. A second case of zero moment is illustrated on Figure 3.6(h). The obtained graphic results arise from applying a force through the nanobar's **C.M.**. To achieve this graphic, the simulation parameters of the pushing force are set to: x_n= 27.50E-09[m] and $y_n = 0$ with an initial nanobar orientation of $\theta_0 = 0$ [rad]. The rest of the parameters have the same values as those previously defined.

3.4.3   Equations of sliding motion of nano-objects on a rough surface

The kinetic frictional force is the tangential resistive force that the nano-object will experience when it slides over a rough surface. The kinetic frictional force direction is opposed to the direction of the movement. Therefore, expressions to describe their influence need to be derived and added in Equations (3.26) for full modelling of the dynamics of the sliding nanobar. The total load (weight) **W** is equal to $(mg + F_{VdW})$. To calculate the attraction force due to the Van der Waals forces F_{VdW} an equation which models the interaction between a rectangular nanobar and a plane has been developed using the pair-wise summation method described in Israelachvili [59]. The developed equation is based on an attractive potential. Also, the applied pushing force **F** is calculated to be the enough to keep the sliding motion of the nano-object.

3.4.3.1 Expressions for frictional force and moment

This section describes the derivation of expressions for friction force f and friction moment m_f experienced by the manipulated nano-object (nanobar) for an even support during its motion. The expressions of friction are defined over a contact area in a region $\Re$. These expressions are based on expressions developed by Cheung in [76]. Assuming the nanobar is in in-plane motion on a planar supporting surface and let

S be the contact region defined by the edge of the contact zone ($\Re_{ABCD}$) between the nano-object and surface,

$\vec{x}$ be the position vector of an element of area dA defined in the region S,

$\vec{m}$ be the position vector of the nanobar's centre of mass,

$\mathbf{p}(\vec{x})$ be the pressure at $\vec{x}$, and

$\vec{v}(\vec{x})$ be the velocity of the nanobar relative to the supporting surface.

Moreover, using Coulomb frictional law model with coefficient of friction μ, *the frictional force* at $\vec{x}$ is given by

$$f(\vec{x}) = -\mu \frac{\vec{v}(\vec{x})}{|\vec{v}(\vec{x})|} p(\vec{x}) \delta A \tag{3.27}$$

and *the frictional moment m_f about C.M.* is

$$m_f(\vec{x}) = -(\vec{x} - \vec{m}) \times \mu \frac{\vec{v}(\vec{x})}{|\vec{v}(\vec{x})|} p(\vec{x}) \delta A \tag{3.28}$$

The total frictional force over the area which belongs to the region S is

$$f = \iint_{\mathbf{S}} -\mu \frac{\vec{v}(\vec{x})}{|\vec{v}(\vec{x})|} p(\vec{x}) \delta A \tag{3.29}$$

and the total friction moment about **C.M.** is

$$m_f = \iint_{\mathbf{S}} -(\vec{x} - \vec{m}) \times \mu \frac{\vec{v}(\vec{x})}{|\vec{v}(\vec{x})|} p(\vec{x}) \delta A \tag{3.30}$$

81

3.4.3.2 Expression for contact area defined in a region $\Re$ for a nanobar with even support

Figure 3.7 shows the reference planes to characterise the motion of the nano-object in coordinate space. The plane OXY is the fixed reference frame. The plane $O'X'Y'$ is a frame of reference associated with the nanobar and hence with the moving frame. The origin of the moving frame is at the instantaneous centre of rotation **iCOR** of the nanobar. Also the moving frame's axis is parallel to the sides of the nanobar. **R** is the distance between the **iCOR** location and the object's centre of mass **C.M.** The coordinates (x_c, y_c) and (x_m, y_m) refer to the location of the **iCOR** and object's **C.M.**. These coordinates are defined with respect to the fixed or reference plane OXY. V_x and V_y are the components of velocity resolved along OX and OY. $V_{x'}$ and $V_{y'}$ are the components of velocity resolved along $O'X'$ and $O'Y'$. In Figure 3.8, where only the moving frame $O'X'Y'$ is represented, the following relations hold

$$h_1 = R\sin(\alpha) - b \tag{3.31}$$

$$h_2 = R\cos(\alpha) + a \tag{3.32}$$

$$h_3 = R\sin(\alpha) + b \tag{3.33}$$

$$h_4 = R\cos(\alpha) - a \tag{3.34}$$

Let the follows angles be defined by

$$\beta_1 = \angle CO'X' = \arctan(h_1/h2) \tag{3.35}$$

$$\beta_2 = \angle BO'X' = \arctan(h_1/h4) \tag{3.36}$$

$$\beta_3 = \angle DO'X' = \arctan(h_3/h2) \tag{3.37}$$

$$\beta_4 = \angle AO'X' = \arctan(h_3/h4) \tag{3.38}$$

As $\vec{v}(\vec{x})$ is the velocity at $\vec{x}$,

$$\hat{v}(\vec{x}) = -\frac{\vec{v}(\vec{x})}{|\vec{v}(\vec{x})|} \qquad (3.39)$$

is the unit vector direction $\hat{v}$ of the frictional force f at $\vec{x}$.

For the nanobar/nanotube area of contact shown in Figure 3.8, it is possible to express the direction of frictional force using a re-defined signum function as in [75]. Therefore

$$sgn(\dot{\theta}) = \begin{cases} +1 & \text{if } \dot{\theta} > 0 \\ -1 & \text{if } \dot{\theta} \leq 0 \end{cases} \qquad (3.40)$$

the area of contact for the nanobar is a rectangular base of dimensions $2a \times 2b$, the pressure function is given by

$$p(x) = \frac{(mg + F_{VdW})}{4ab} \qquad (3.41)$$

If $f_{x'}$ and $f_{y'}$ are the components of the frictional force along the moving axis $O'X'$ and $O'Y'$ respectively. Thus,

$$f_{x'} = \frac{\mu(mg + F_{VdW})}{4ab} sign(\dot{\theta}) \iint_{\mathbf{S}} \sin(\gamma) r \, dr \, d\gamma \qquad (3.42)$$

$$f_{y'} = \frac{-\mu(mg + F_{VdW})}{4ab} sign(\dot{\theta}) \iint_{\mathbf{S}} \cos(\gamma) r \, dr \, d\gamma \qquad (3.43)$$

$$m_f = \frac{-\mu(mg + F_{VdW})}{4ab} sign(\dot{\theta}) \iint_{\mathbf{S}} (R\cos(\alpha - \gamma) - r) r \, dr \, d\gamma \qquad (3.44)$$

After integrating (see Appendix B for details)

$$f_{x'} = \frac{\mu(mg + F_{VdW})}{8ab} sign(\dot{\theta}) \left[h_2 \left(\sqrt{h_2^2 + h_3^2} - \sqrt{h_1^2 + h_2^2} \right) + h_4 \left(\sqrt{h_1^2 + h_4^2} - \sqrt{h_3^2 + h_4^2} \right) \right.$$

$$\left. - h_1^2 \ln\left[\left(\sqrt{h_1^2 + h_4^2} - h_4 \right) / \left(\sqrt{h_1^2 + h_2^2} - h_2 \right) \right] + h_3^2 \ln\left[\left(\sqrt{h_3^2 + h_4^2} - h_4 \right) / \left(\sqrt{h_2^2 + h_3^2} - h_2 \right) \right] \right]$$

(3.45)

$$f_{y'} = \frac{\mu(mg + F_{VdW})}{8ab} sign(\dot{\theta}) \left[h_1 \left(\sqrt{h_1^2 + h_4^2} - \sqrt{h_1^2 + h_2^2} \right) + h_3 \left(\sqrt{h_2^2 + h_3^2} - \sqrt{h_3^2 + h_4^2} \right) \right.$$

$$\left. + h_2^2 \ln\left[\left(\sqrt{h_2^2 + h_3^2} + h_3 \right) / \left(\sqrt{h_1^2 + h_2^2} + h_1 \right) \right] - h_4^2 \ln\left[\left(\sqrt{h_3^2 + h_4^2} + h_3 \right) / \left(\sqrt{h_1^2 + h_4^2} + h_1 \right) \right] \right]$$

(3.46)

$$m_f = \frac{\mu(mg + F_{VdW})}{4ab} \left[R\cos(\alpha)\frac{C_1}{2} + R\sin(\alpha)\frac{C_2}{2} - \frac{C_3}{3} - \frac{C_4}{6} \right] \qquad (3.47)$$
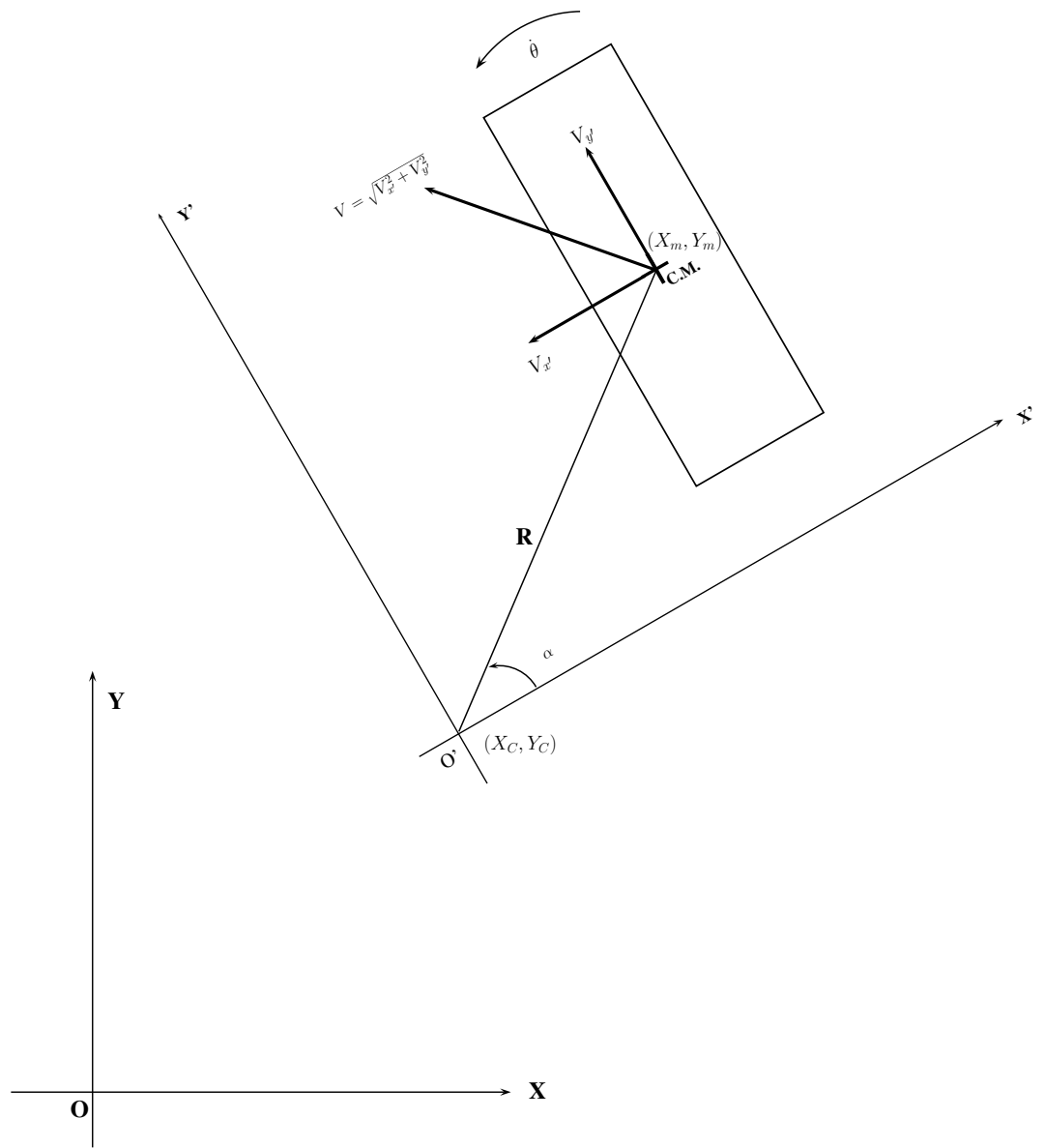
Figure 3.7: Characterisation of the motion of the nano-object referenced to the static frame **OXY** (reference frame) and its moving frame **X'O'Y'** (dynamic frame).
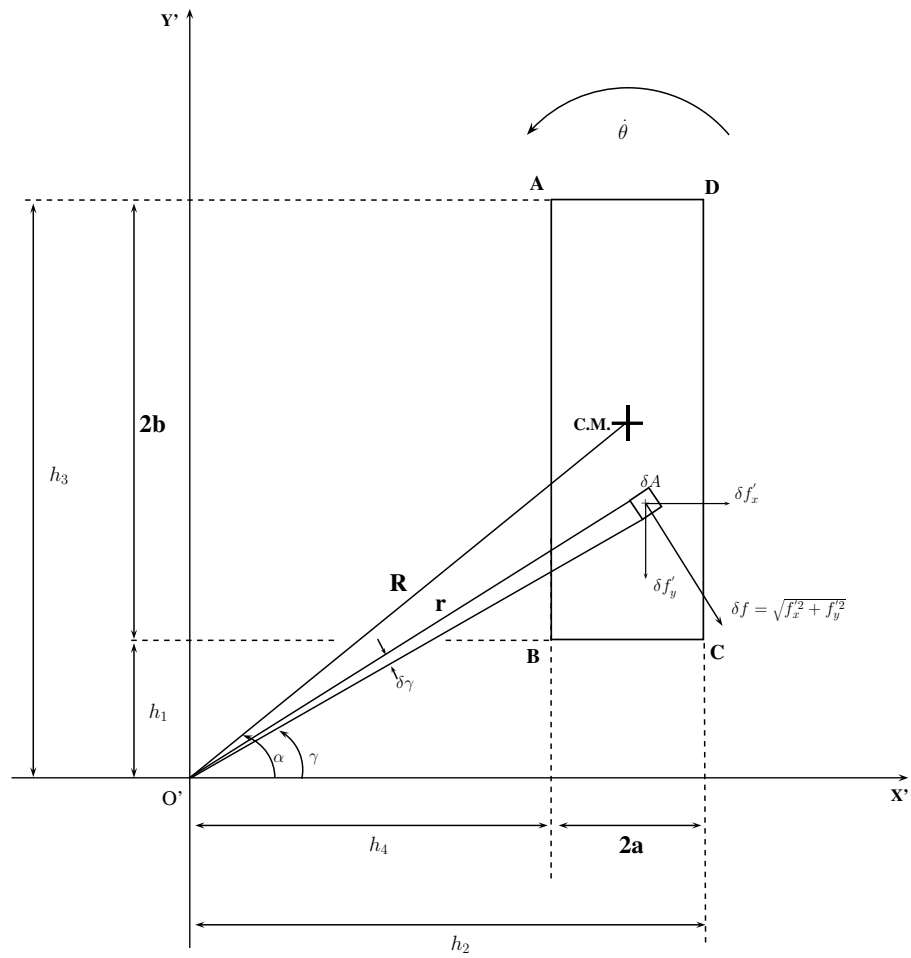
Figure 3.8: Geometrical parameters definitions reference to the mobile frame **X'O'Y'**.

where

$$C1 = h_1\left(\sqrt{h_1^2 + h_4^2} - \sqrt{h_1^2 + h_2^2}\right) + h_3\left(\sqrt{h_2^2 + h_3^2} - \sqrt{h_3^2 + h_4^2}\right)$$
$$+ h_2^2 \ln\left[\left(\sqrt{h_2^2 + h_3^2} + h_3\right)/\left(\sqrt{h_1^2 + h_2^2} + h_1\right)\right]$$
$$- h_4^2 \ln\left[\left(\sqrt{h_3^2 + h_4^2} + h_3\right)/\left(\sqrt{h_1^2 + h_4^2} + h_1\right)\right]$$

$$C2 = h_2\left(\sqrt{h_2^2 + h_3^2} - \sqrt{h_1^2 + h_2^2}\right) + h_4\left(\sqrt{h_1^2 + h_4^2} - \sqrt{h_3^2 + h_4^2}\right)$$
$$+ h_3^2 \ln\left[\left(\sqrt{h_3^2 + h_4^2} - h_4\right)/\left(\sqrt{h_2^2 + h_3^2} - h_2\right)\right]$$
$$- h_1^2 \ln\left[\left(\sqrt{h_1^2 + h_4^2} - h_4\right)/\left(\sqrt{h_1^2 + h_2^2} - h_2\right)\right]$$

$$C3 = -h_1h_2\sqrt{h_1^2 + h_2^2} + h_2h_3\sqrt{h_2^2 + h_3^2} - h_3h_4\sqrt{h_3^2 + h_4^2} + h_1h_4\sqrt{h_1^2 + h_4^2}$$

$$C4 = h_1^2 \ln\left[\left(\sqrt{h_1^2 + h_2^2} - h_2\right)/\left(\sqrt{h_1^2 + h_4^2} - h_4\right)\right]$$
$$+ h_2^2 \ln\left[\left(\sqrt{h_2^2 + h_3^2} + h_3\right)/\left(\sqrt{h_1^2 + h_2^2} + h_1\right)\right]$$
$$+ h_3^2 \ln\left[\left(\sqrt{h_3^2 + h_4^2} - h_4\right)/\left(\sqrt{h_2^2 + h_3^2} - h_2\right)\right]$$
$$+ h_4^2 \ln\left[\left(\sqrt{h_1^2 + h_4^2} + h_1\right)/\left(\sqrt{h_3^2 + h_4^2} + h_3\right)\right]$$

(3.48)

the component of the friction force in the OX direction is

$$f_x = f_{x'}\cos(\theta) - f_{y'}\sin(\theta) \tag{3.49}$$

87

the component of the friction force in the OY direction is

$$f_y = f_{x'}\sin(\theta) - f_{y'}\cos(\theta) \tag{3.50}$$

The total frictional force magnitude $f = \sqrt{f_{x'}^2 + f_{y'}^2} = \sqrt{f_x^2 + f_y^2}$. Therefore, for a given coefficient of friction μ and nano object mass m, the frictional force f and its moment m_f are both functions of the geometrical parameters R and α as in [76].

3.4.3.3 Variation of frictional force and moment with R

The frictional force f and its frictional moment m_f are normalised to study their behaviour during the nanobar motion. Figure 3.9 plots the normalised values of the friction force and moment of friction for different values of R and $\alpha = 0$ for the analysed case of a rectangular contact area with uniform pressure distribution. Similar variations were observed with different values of α.

Firstly, at $R = 0$ the case when the nanobar was rotating about its centre of mass **C.M.** (pure rotation) the frictional moment magnitude was maximum, whereas the frictional force was zero (no sliding at all).

Secondly, it may be seen that as the value of R approaches its maximum (infinity), the nanobar undergoes pure translation. In pure translation, the frictional force magnitude approaches its maximum and the frictional moment magnitude to zero (no rotation at all). This is because all of its components have cancelled out one another and there is no net friction force.

Finally, it may be seen that when the value of R is between its minimum and its maximum, the motion of the nanobar is a combination of in-plane translation and in-plane rotation, so the frictional force increase and the frictional moment decreases. Therefore, *the curves presented in Figure 3.9 explicity demostrate the coupling of forces and moments in sliding as the magnitude of force required for sliding decreases as the applied moment increases, and vice versa*.

88
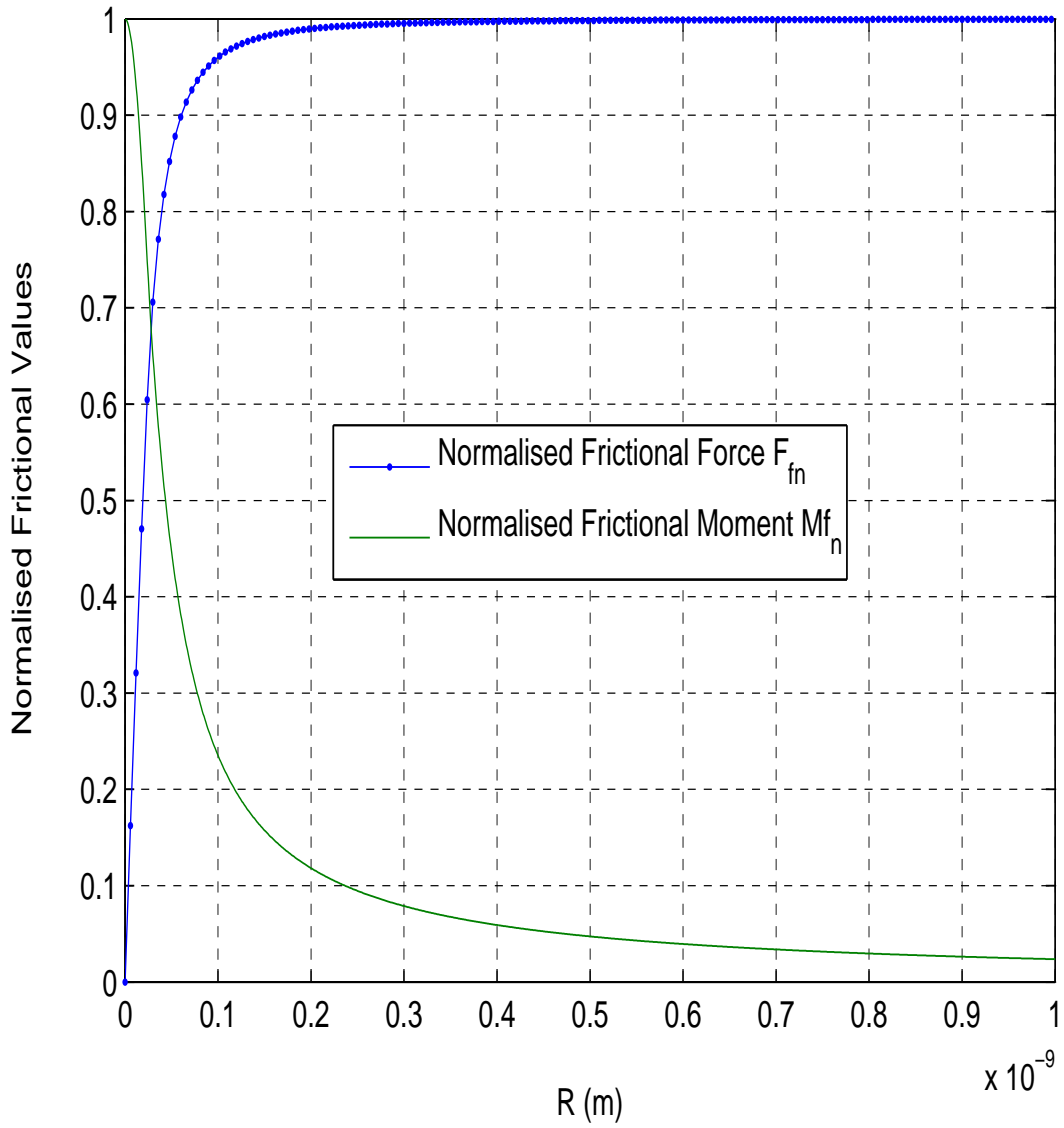
Figure 3.9: Normalised frictional force F_{f_n} and frictional moment Mf_n versus locations of its **COR** for nanobar of dimensions $100 \times 50 \times 55$[nm]. The nanobar is assumed to be made from carbon sliding over a graphite surface.

3.4.3.4 Variation of the friction force and moment over the contact area with location of iCOR in inplane-rotation motion

The magnitude of the normalised frictional force and friction moment extended over the contact are shown in Figure 3.10 and Figure 3.11 respectively during in-plane sliding motion. The centre of pressure of the contact area is located at its geometrical centre which coincides with the centre of mass of the nanobar. For instance, Figure 3.10 shows that the contribution of the frictional force at contacts near to the centre of pressure are less in magnitude than for those contacts near the contact edge.

On the other hand, Figure 3.11 shows that the distributions of the normalised frictional moment at contacts near to the centre of pressure are higher in magnitude. This result is consistent with the graph shown on Figure 3.9, where the value of the frictional force is minimum favouring the motion of the nanobar as pure rolling.

Pure sliding motion of the nanobar can be seen from the normalised frictional force for locations of **iCOR** far from the centre of pressure as the value of the normalised increase at it maximum. However, from Figure 3.11 the normalised frictional moment magnitude decreases when the **iCOR** is positioned far from the centre of pressure. Intermediate values on the **iCOR** location present a combination of in-plane translation and in plane rotation in their normalised frictional values.

Finally, these graphics can also be used to find the motion, both translational and rotational, that results for a given applied force and moment. This is important for the dynamic simulation of manipulation tasks, and for planning and controlling contact tasks where the forces need to be generated to complete the manipulation task. Therefore, for any combination of force or moment in the graphics there is an unique **iCOR** associated, and thus the instantaneous motion of the contact is specified.
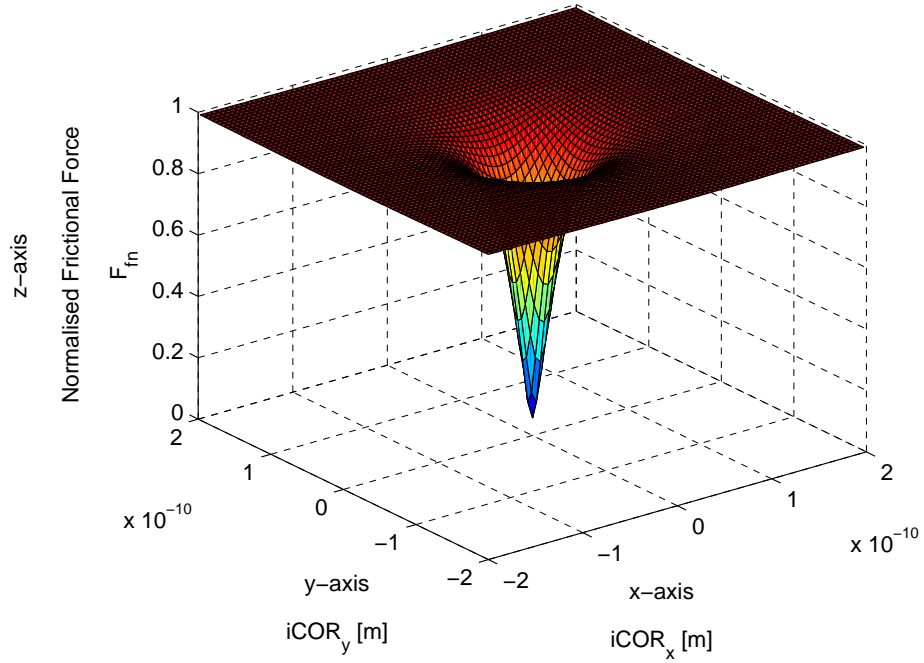
(a) 3D Variation of the normalised frictional force with iCOR position.
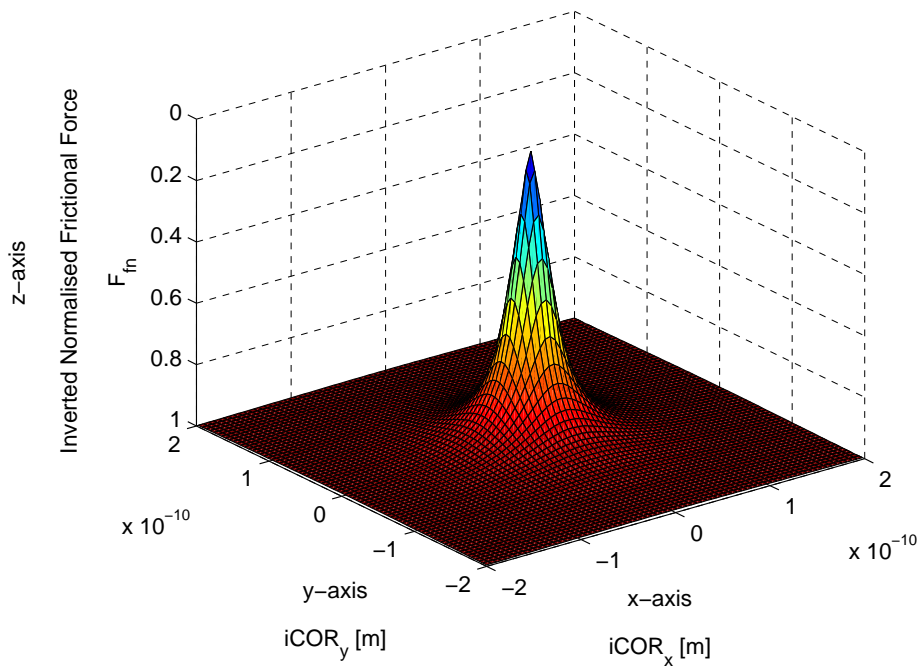
(b) 3D Variation of the inverted of the normalised frictional force with iCOR position.

Figure 3.10: 3D visualisation of the normalised frictional force with iCOR location over the contact area.
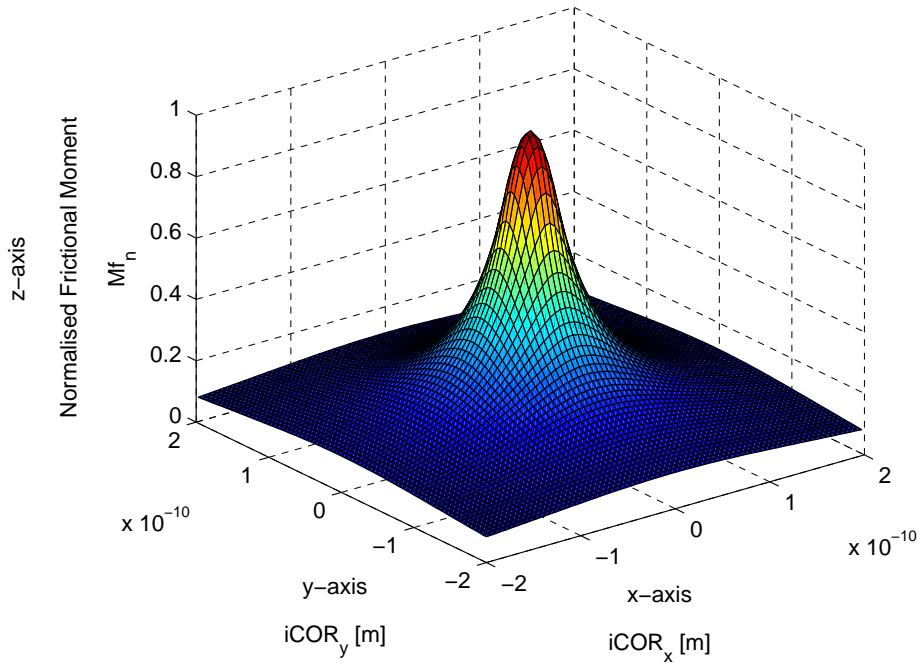
(a) 3D Variation of the inverted of the normalised frictional moment with iCOR position.
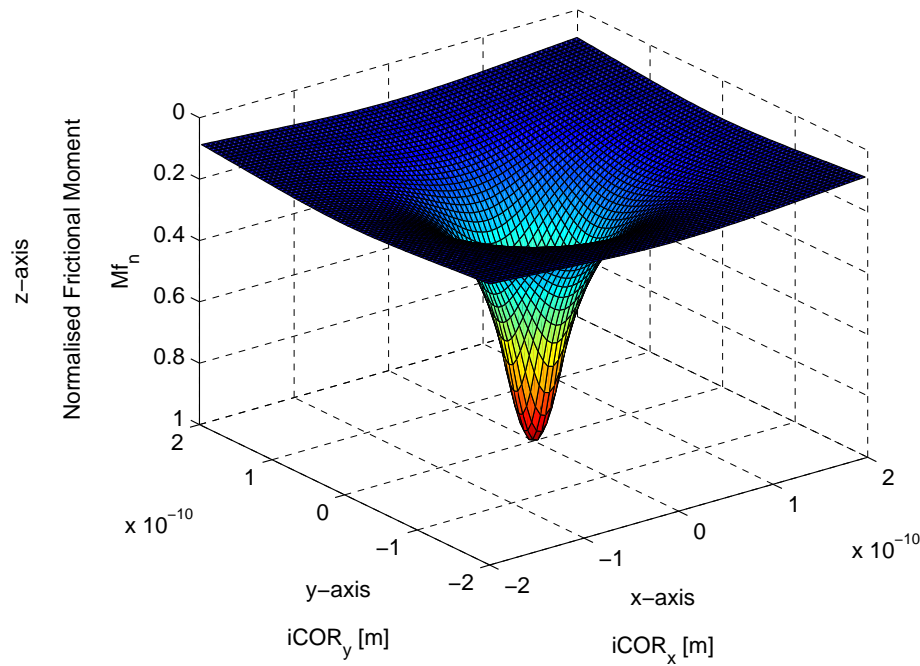
(b) 3D Variation of the inverted of the normalised frictional moment with iCOR position.

Figure 3.11: 3D visualisation of the normalised frictional moment force with iCOR location over the contact area.

3.4.4 Equations of motion of rectangular nanobar on rough surfaces

Using the expressions of friction Equation (3.45), Equation (3.46), and Equation (3.47) into Equations (3.26) full equations of nanobar motion are obtained. Therefore,

$$m\dot{V}_x = F\cos(\beta) + f_x(R, \alpha) \tag{3.51}$$

$$\dot{x} = V_x \tag{3.52}$$

$$m\dot{V}_y = F\sin(\beta) + f_y(R, \alpha) \tag{3.53}$$

$$\dot{y} = F\cos(\beta) \tag{3.54}$$

$$I\dot{\omega} = F \times d\cos(\theta - \beta + \phi) + f_x(R, \alpha) \tag{3.55}$$

$$\dot{\theta} = \omega \tag{3.56}$$

It should be noted that Equation (3.51) to Equation (3.56) the frictional terms are added to be positive as the sense of its value is characterised by Equation (3.40). In addition, the values of R and α depend on values of $\dot{x}$, $\dot{y}$, and $\dot{\theta}$. Therefore, the written program in Fortran, that uses the numerical integration method described in section (3.4.2), is updated with a function that takes into account the geometrical parameters of the friction and friction moment [76].

3.4.4.1   Results from simulations

This section presents a detailed analysis of the frictional force and frictional moment over a contact area for a nanobar in sliding motion. Twenty graphs summarised in Figure 3.12 to Figure 3.32 give nanobar motion and frictional values. A variation in the coefficient of friction μ from zero to 0.20 is simulated. All experimental values are in double precision arithmetic using Equation (3.51) to Equation (3.56) and using the developed programming code in FORTRAN which is implemented in the **Bulirsch-Stoer method**. Simulations were running on O.S. Linux environment (Ubuntu 12.04 LTS) on a CPU AMD Turion64x2, 4Gb in RAM and using double precision arithmetic.

Also, in all cases the nanobar's initial orientation is zero and the simulation parameters are described in their respective labels. The first analysis is presented in Figure 3.12. This case corresponds to the case when the coefficient of friction is zero (no frictional force). Thus, frictional force and its moment are equal to zero as shown in Figure 3.12(b) and Figure 3.12(c), and the amplitude of the nanobar is at its maximum value as shown in Figure 3.12(a) respectively.

Nanobar orientation under different coefficients of friction

Figures 3.12(a) to 3.32(a) shows the orientation of the nanobar in radians for different values of coefficient of friction. These coefficients of friction are taken from $\mu = 0.0$ to $\mu = 0.20$ at 0.01 step increments while the pushing force magnitude is kept constant. It has been observed from the orientation graphics that the nanobar orientation has a decrement in its magnitude. The decrement in this orientation became bigger as the value in the coefficient of friction increased (small oscillations). When the coefficient of friction μ was big enough, the nanobar had no motion in it's orientation. Thus, the friction coefficient magnitude is related with the decrement in the nanobar ocillation. Finally, the nanobar is at its fixed and stable orientation during the rest of the simulated period. Therefore, the nanobar is in steady translation.

Frictional moment

Figures 3.12(b) to 3.32(b) show the magnitude of the frictional moment M_f that exists at each in-plane nanobar rotation. Low values of the frictional moment are observed for different values in the coefficient of friction μ. Small ripples are observed that correspond to each amplitude during the oscillation of the nanobar. For high values of frictional coefficient of friction (**i.e.** $\mu = 0.15$), the ripples became less in amplitude approximating to a flat line (no rotation). It was also observed that the maximum value of the frictional moment occurs at the start of nanobar rotation for all cases. In general, values of the observed frictional moment were less in magnitude than those shown in the components of the friction force f_x and f_y.

Frictional force component in x

Figures 3.12(c) to 3.32(c) show the magnitude of the component in x of the frictional force f_x. In all the simulated cases, the component of the frictional force in x f_x has the biggest values. This force component presents a consistent clock signal shape with negative and positive values. Negative values in its magnitude correspond to increments of in-plane rotation (in an anti-clockwise direction). After all, the direction of f_x should be in the opposite direction to the motion. Thus, the nanobar is rotating from an initial orientation of zero $\theta_o = 0$[rad] until it will achieve its maximum orientation. The maximum orientation θ_{max} is a function of the coefficient of friction μ value. Whereas positive values in the f_x magnitude corresponds to clockwise motion of the nanobar (negative in-plane rotation). It has also been noticed that the first peak in the f_x graphs presents a small ripple which vanishes after that point.

Constant values of f_x are observed for the rest of the peaks and its magnitude in all graphics generated during the simulations. Furthermore, this graphic could introduce the stick-slip motion. Stick-slip motion could appear for a missing part of the total frictional force, as the measured forces could only represent a component f_x in the magnitude from the total frictional force f for the manipulated system. In addition, these results strongly suggest that the nano-object goes into a combination of translation and rotation motion. Thus, the friction force can be modelled using the Coulomb frictional model.

Frictional force component in y

Figures 3.12(d) to 3.32(d) shows the magnitude of the component of the frictional force f_y. Values less in magnitude than the frictional component f_x and bigger in magnitude than the frictional moment m_f are presented in all these graphics. Here the magnitude of the frictional forces with the frictional moment is being compared for appreciation of the contribution of their magnitude in the nano-object's motion, respectively. The frictional force f_y presents a high value in magnitude which decreases after the nanobar changes its orientation from anti-clockwise (positive in-plane rotations) to clockwise (negative in-plane rotations) direction for the first time in its corresponding orientation graphic (Figures 3.12(a) to 3.32(a)). Finally, an increment in its magnitude force and a clock signal shape appears for increments in the coefficient of friction value μ when the nanobar is in slliding motion.

Frictional force magnitude

Frictional force magnitude is presented in Figures 3.12(e) to 3.32(e). The magnitude is calculated as the root square of the sum of the squares of component friction in the x and y directions. This graphic shows the phases which the frictional force go through. Also, it can be compared with a classic model of friction where two phases are present. These phases correspond to static and kinetic phases. In the first part, which corresponds to the static case, the nanobar is in rotation. The second phase, which corresponds to the kinetic case, the nanobar is in in-plane translation. Finally, a comparison of the frictional force and its moment is shown in Figures 3.12(f) to 3.32(f), which summarises the magnitude of the frictional forces involved when the in-plane nanobar rotation takes places for a comparative magnitude analysis. As observed before, the component of the frictional force f_x is the major contribution of the total frictional force present in the system. On the other hand, the frictional moment m_f has the lowest influence onto the total friction. Therefore, a bigger value of frictional force is atribuited to sliding displacements whereas low value of the frictional moment to its rotations.

Figure 3.12: Coordinates of Application Force: Xn= 0.275000E-07[m] Yn= 0.450000E-07[m]. Initial Coordinates of C.M: CMx= 0.00E+00[m] CMy= 0.00E+00[m]. Initial orientation: Angle= 0.000000E+00[rad]. Initial velocity in x: Vx= 0.000000E+00[m/s]. Initial velocity in y: Vy= 0.000000E+00[m/s]. Initial angular velocity: $\omega_o = 0.000000E+00$[rad/s]. Pulling/Pushing Force Applied: F= 0.500000E-05[N]. Adhesion Force (VdW): Fvdw= 0.400252E-04[N]. Coefficient Friction: μ= 0.000000E+00 . Object mass: m= 0.623425E-18[kg]. Object dimensions: sa= 0.550000E-07[m] sb= 0.100000E-06[m] sc= 0.550000E-07[m].

97

Figure 3.13: Coordinates of Application Force: Xn= 0.275000E-07[m] Yn= 0.450000E-07[m]. Initial Coordinates of C.M: CMx= 0.00E+00[m] CMy= 0.00E+00[m]. Initial orientation: Angle= 0.000000E+00[rad]. Initial velocity in x: Vx= 0.000000E+00[m/s]. Initial velocity in y: Vy= 0.000000E+00[m/s]. Initial angular velocity: ω_o = 0.000000E+00[rad/s]. Pulling/Pushing Force Applied: F= 0.500000E-05[N]. Adhesion Force (VdW): Fvdw= 0.400252E-04[N]. Coefficient Friction: μ= 0.100000E-01 . Object mass: m= 0.623425E-18[kg]. Object dimensions: sa= 0.550000E-07[m] sb= 0.100000E-06[m] sc= 0.550000E-07[m]

98

(a)

(b)

(c)

(d)

(e)

(f)

Figure 3.14: Coordinates of Application Force: Xn= 0.275000E-07[m] Yn= 0.450000E-07[m]. Initial Coordinates of C.M: CMx= 0.00E+00[m] CMy= 0.00E+00[m]. Initial orientation: Angle= 0.000000E+00[rad]. Initial velocity in x: Vx= 0.000000E+00[m/s]. Initial velocity in y: Vy= 0.000000E+00[m/s]. Initial angular velocity: $\omega_o = 0.000000E+00$[rad/s]. Pulling/Pushing Force Applied: F= 0.500000E-05[N]. Adhesion Force (VdW): Fvdw= 0.400252E-04[N]. Coefficient Friction: μ= 0.200000E-01 . Object mass: m= 0.623425E-18[kg]. Object dimensions: sa= 0.550000E-07[m] sb= 0.100000E-06[m] sc= 0.550000E-07[m]

99

Figure 3.15: Coordinates of Application Force: Xn= 0.275000E-07[m] Yn= 0.450000E-07[m]. Initial Coordinates of C.M: CMx= 0.00E+00[m] CMy= 0.00E+00[m]. Initial orientation: Angle= 0.000000E+00[rad]. Initial velocity in x: Vx= 0.000000E+00[m/s]. Initial velocity in y: Vy= 0.000000E+00[m/s]. Initial angular velocity: ω_o = 0.000000E+00[rad/s]. Pulling/Pushing Force Applied: F= 0.500000E-05[N]. Adhesion Force (VdW): Fvdw= 0.400252E-04[N]. Coefficient Friction: μ= 0.300000E-01 . Object mass: m= 0.623425E-18[kg]. Object dimensions: sa= 0.550000E-07[m] sb= 0.100000E-06[m] sc= 0.550000E-07[m]

100

Figure 3.16: Coordinates of Application Force: Xn= 0.275000E-07[m] Yn= 0.450000E-07[m]. Initial Coordinates of C.M: CMx= 0.00E+00[m] CMy= 0.00E+00[m]. Initial orientation: Angle= 0.000000E+00[rad]. Initial velocity in x: Vx= 0.000000E+00[m/s]. Initial velocity in y: Vy= 0.000000E+00[m/s]. Initial angular velocity: $\omega_o = 0.000000E+00$[rad/s]. Pulling/Pushing Force Applied: F= 0.500000E-05[N]. Adhesion Force (VdW): Fvdw= 0.400252E-04[N]. Coefficient Friction: μ= 0.400000E-01 . Object mass: m= 0.623425E-18[kg]. Object dimensions: sa= 0.550000E-07[m] sb= 0.100000E-06[m] sc= 0.550000E-07[m]

101

Figure 3.17: Coordinates of Application Force: Xn= 0.275000E-07[m] Yn= 0.450000E-07[m]. Initial Coordinates of C.M: CMx= 0.00E+00[m] CMy= 0.00E+00[m]. Initial orientation: Angle= 0.000000E+00[rad]. Initial velocity in x: Vx= 0.000000E+00[m/s]. Initial velocity in y: Vy= 0.000000E+00[m/s]. Initial angular velocity: ω_o = 0.000000E+00[rad/s]. Pulling/Pushing Force Applied: F= 0.500000E-05[N]. Adhesion Force (VdW): Fvdw= 0.400252E-04[N]. Coefficient Friction: μ= 0.500000E-01 . Object mass: m= 0.623425E-18[kg]. Object dimensions: sa= 0.550000E-07[m] sb= 0.100000E-06[m] sc= 0.550000E-07[m]

(a)

(b)

(c)

(d)

(e)

(f)

Figure 3.18: Coordinates of Application Force: Xn= 0.275000E-07[m] Yn= 0.450000E-07[m]. Initial Coordinates of C.M: CMx= 0.00E+00[m] CMy= 0.00E+00[m]. Initial orientation: Angle= 0.000000E+00[rad]. Initial velocity in x: Vx= 0.000000E+00[m/s]. Initial velocity in y: Vy= 0.000000E+00[m/s]. Initial angular velocity: $\omega_o = 0.000000E+00$[rad/s]. Pulling/Pushing Force Applied: F= 0.500000E-05[N]. Adhesion Force (VdW): Fvdw= 0.400252E-04[N]. Coefficient Friction: μ= 0.600000E-01 . Object mass: m= 0.623425E-18[kg]. Object dimensions: sa= 0.550000E-07[m] sb= 0.100000E-06[m] sc= 0.550000E-07[m]

103

(a)

(b)

(c)

(d)

(e)

(f)
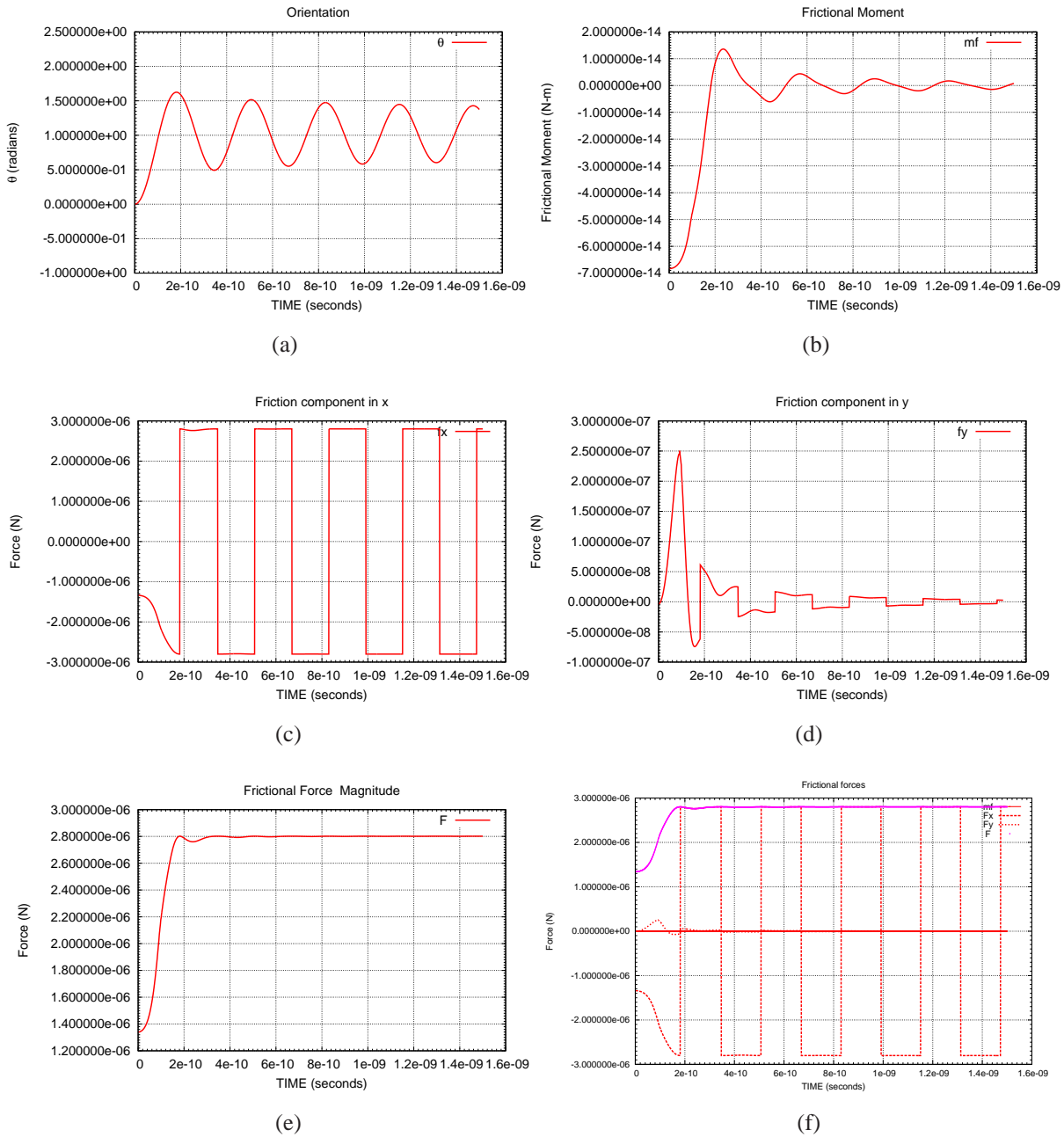
Figure 3.19: Coordinates of Application Force: Xn= 0.275000E-07[m] Yn= 0.450000E-07[m]. Initial Coordinates of C.M: CMx= 0.00E+00[m] CMy= 0.00E+00[m]. Initial orientation: Angle= 0.000000E+00[rad]. Initial velocity in x: Vx= 0.000000E+00[m/s]. Initial velocity in y: Vy= 0.000000E+00[m/s]. Initial angular velocity: ω_o = 0.000000E+00[rad/s]. Pulling/Pushing Force Applied: F= 0.500000E-05[N]. Adhesion Force (VdW): Fvdw= 0.400252E-04[N]. Coefficient Friction: μ= 0.700000E-01 . Object mass: m= 0.623425E-18[kg]. Object dimensions: sa= 0.550000E-07[m] sb= 0.100000E-06[m] sc= 0.550000E-07[m]

104

(a)

(b)

(c)

(d)

(e)

(f)
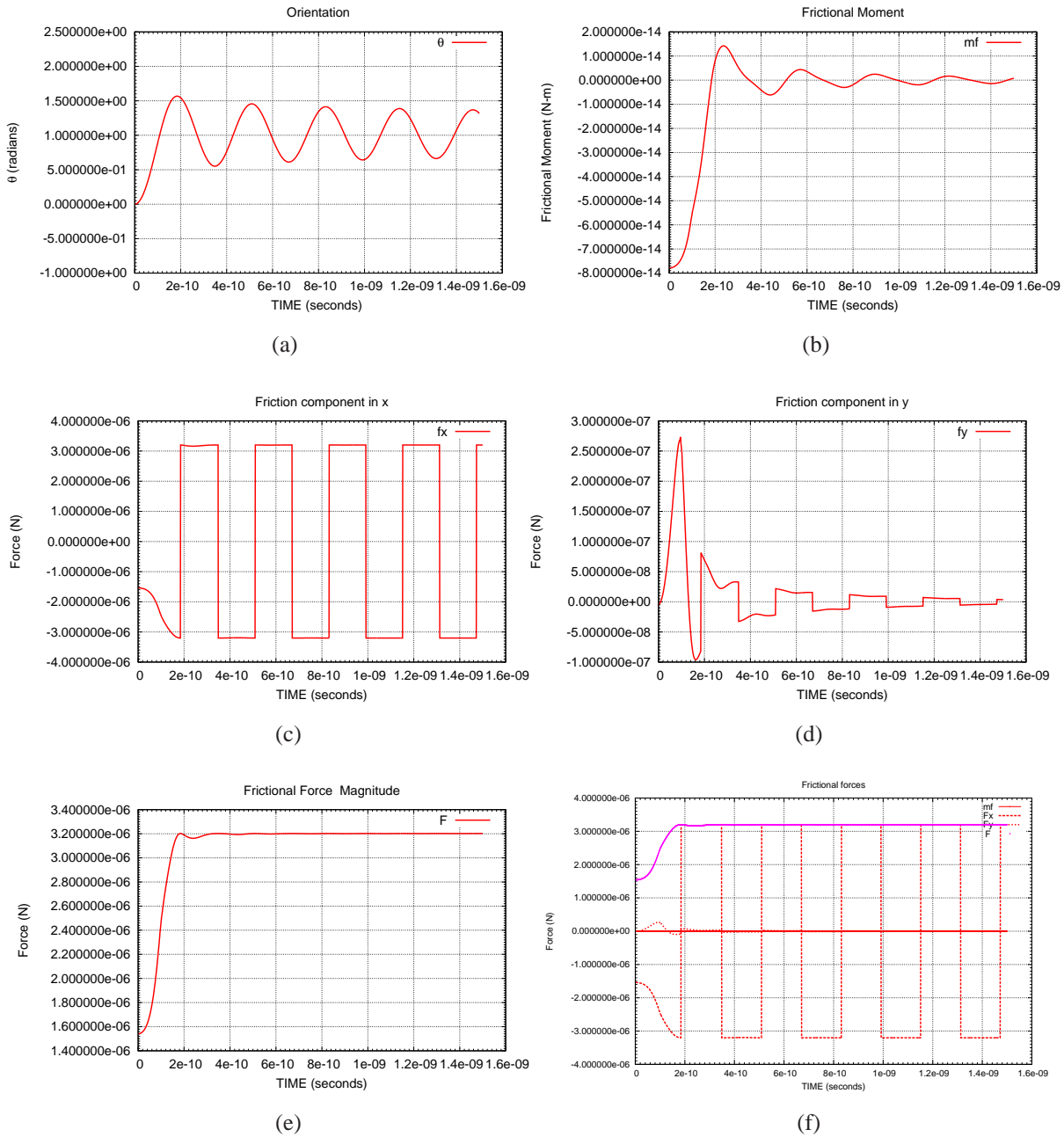
Figure 3.20: Coordinates of Application Force: Xn= 0.275000E-07[m] Yn= 0.450000E-07[m]. Initial Coordinates of C.M: CMx= 0.00E+00[m] CMy= 0.00E+00[m]. Initial orientation: Angle= 0.000000E+00[rad]. Initial velocity in x: Vx= 0.000000E+00[m/s]. Initial velocity in y: Vy= 0.000000E+00[m/s]. Initial angular velocity: ω_o = 0.000000E+00[rad/s]. Pulling/Pushing Force Applied: F= 0.500000E-05[N]. Adhesion Force (VdW): Fvdw= 0.400252E-04[N]. Coefficient Friction: μ= 0.800000E-01 . Object mass: m= 0.623425E-18[kg]. Object dimensions: sa= 0.550000E-07[m] sb= 0.100000E-06[m] sc= 0.550000E-07[m]

105
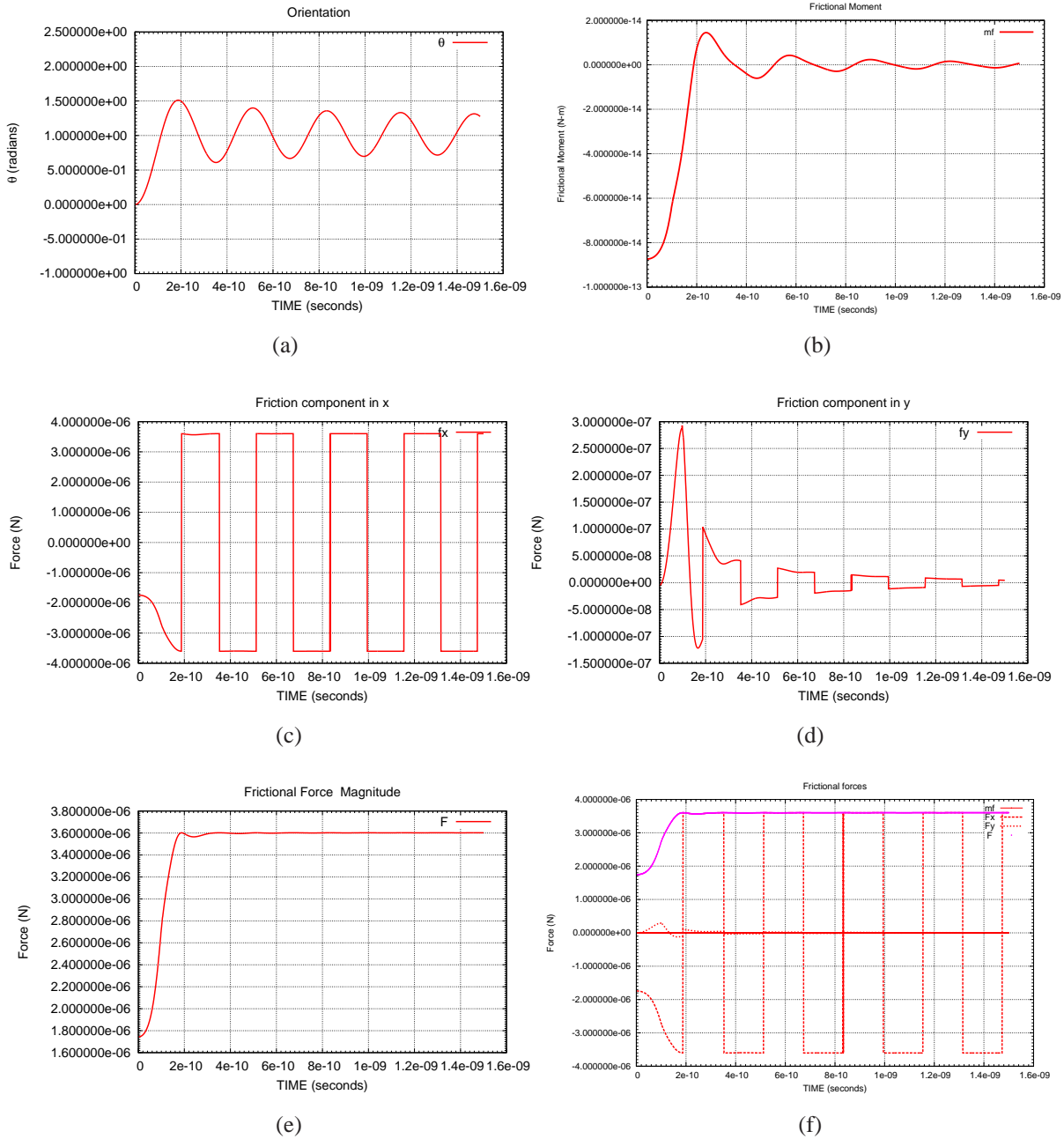
Figure 3.21: Coordinates of Application Force: Xn= 0.275000E-07[m] Yn= 0.450000E-07[m]. Initial Coordinates of C.M: CMx= 0.00E+00[m] CMy= 0.00E+00[m]. Initial orientation: Angle= 0.000000E+00[rad]. Initial velocity in x: Vx= 0.000000E+00[m/s]. Initial velocity in y: Vy= 0.000000E+00[m/s]. Initial angular velocity: ω_o = 0.000000E+00[rad/s]. Pulling/Pushing Force Applied: F= 0.500000E-05[N]. Adhesion Force (VdW): Fvdw= 0.400252E-04[N]. Coefficient Friction: μ= 0.900000E-01 . Object mass: m= 0.623425E-18[kg]. Object dimensions: sa= 0.550000E-07[m] sb= 0.100000E-06[m] sc= 0.550000E-07[m]
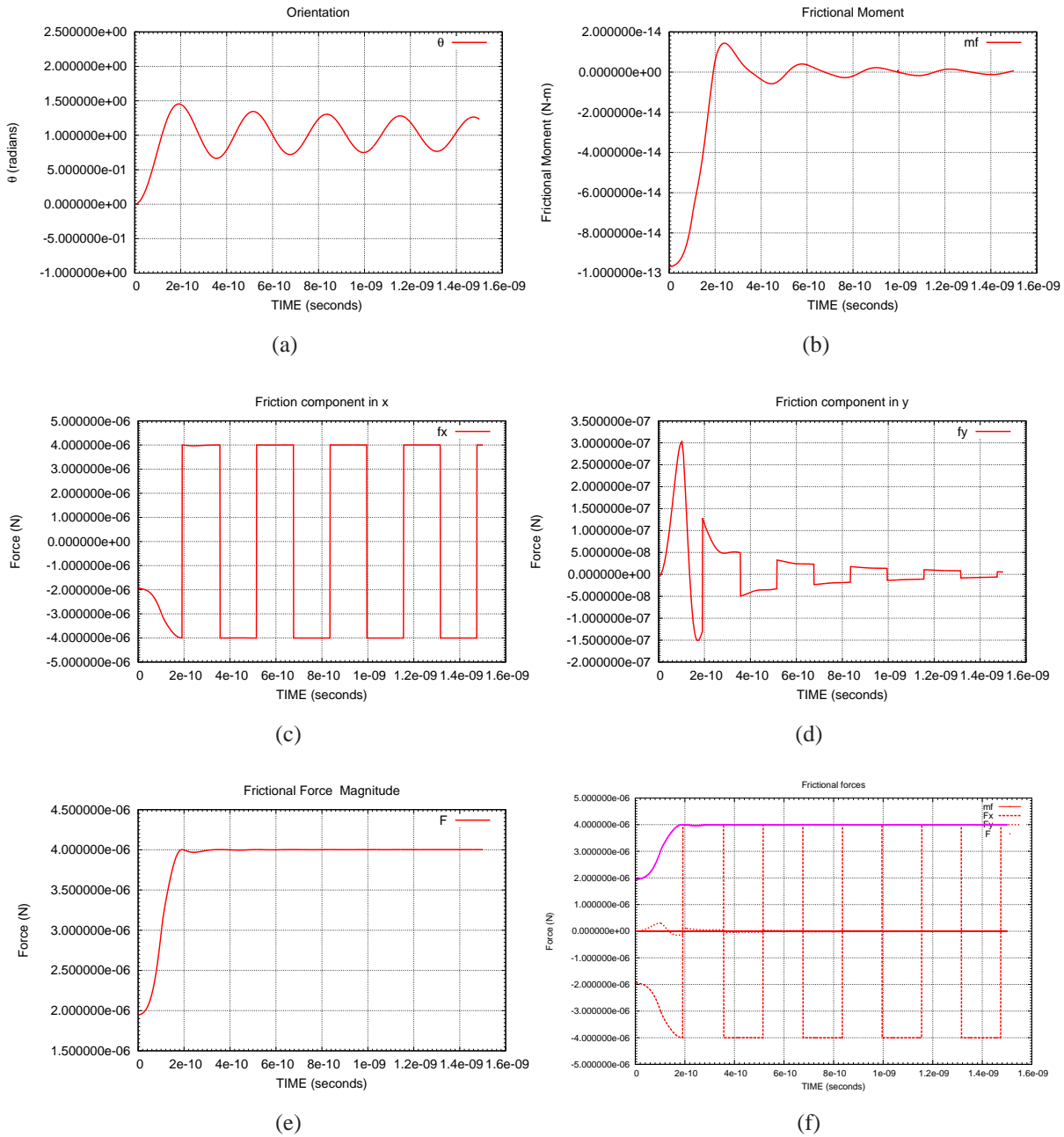
Figure 3.22: Coordinates of Application Force: Xn= 0.275000E-07[m] Yn= 0.450000E-07[m]. Initial Coordinates of C.M: CMx= 0.00E+00[m] CMy= 0.00E+00[m]. Initial orientation: Angle= 0.000000E+00[rad]. Initial velocity in x: Vx= 0.000000E+00[m/s]. Initial velocity in y: Vy= 0.000000E+00[m/s]. Initial angular velocity: ω_o = 0.000000E+00[rad/s]. Pulling/Pushing Force Applied: F= 0.500000E-05[N]. Adhesion Force (VdW): Fvdw= 0.400252E-04[N]. Coefficient Friction: μ= 0.100000E+00 . Object mass: m= 0.623425E-18[kg]. Object dimensions: sa= 0.550000E-07[m] sb= 0.100000E-06[m] sc= 0.550000E-07[m]

107
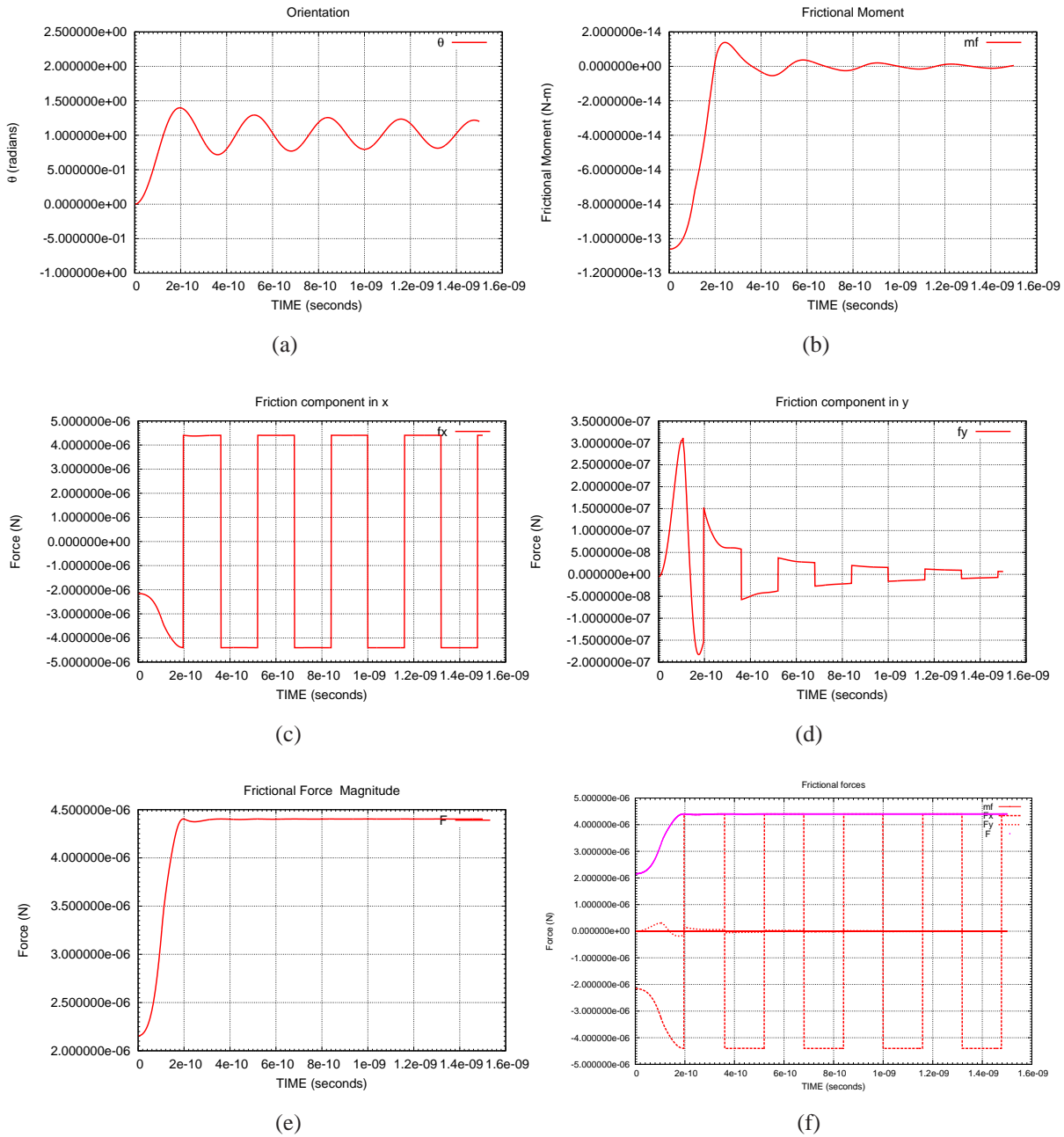
Figure 3.23: Coordinates of Application Force: Xn= 0.275000E-07[m] Yn= 0.450000E-07[m]. Initial Coordinates of C.M: CMx= 0.00E+00[m] CMy= 0.00E+00[m]. Initial orientation: Angle= 0.000000E+00[rad]. Initial velocity in x: Vx= 0.000000E+00[m/s]. Initial velocity in y: Vy= 0.000000E+00[m/s]. Initial angular velocity: ω_o = 0.000000E+00[rad/s]. Pulling/Pushing Force Applied: F= 0.500000E-05[N]. Adhesion Force (VdW): Fvdw= 0.400252E-04[N]. Coefficient Friction: μ= 0.110000E+00 . Object mass: m= 0.623425E-18[kg]. Object dimensions: sa= 0.550000E-07[m] sb= 0.100000E-06[m] sc= 0.550000E-07[m]

108

(a)

(b)

(c)

(d)

(e)

(f)
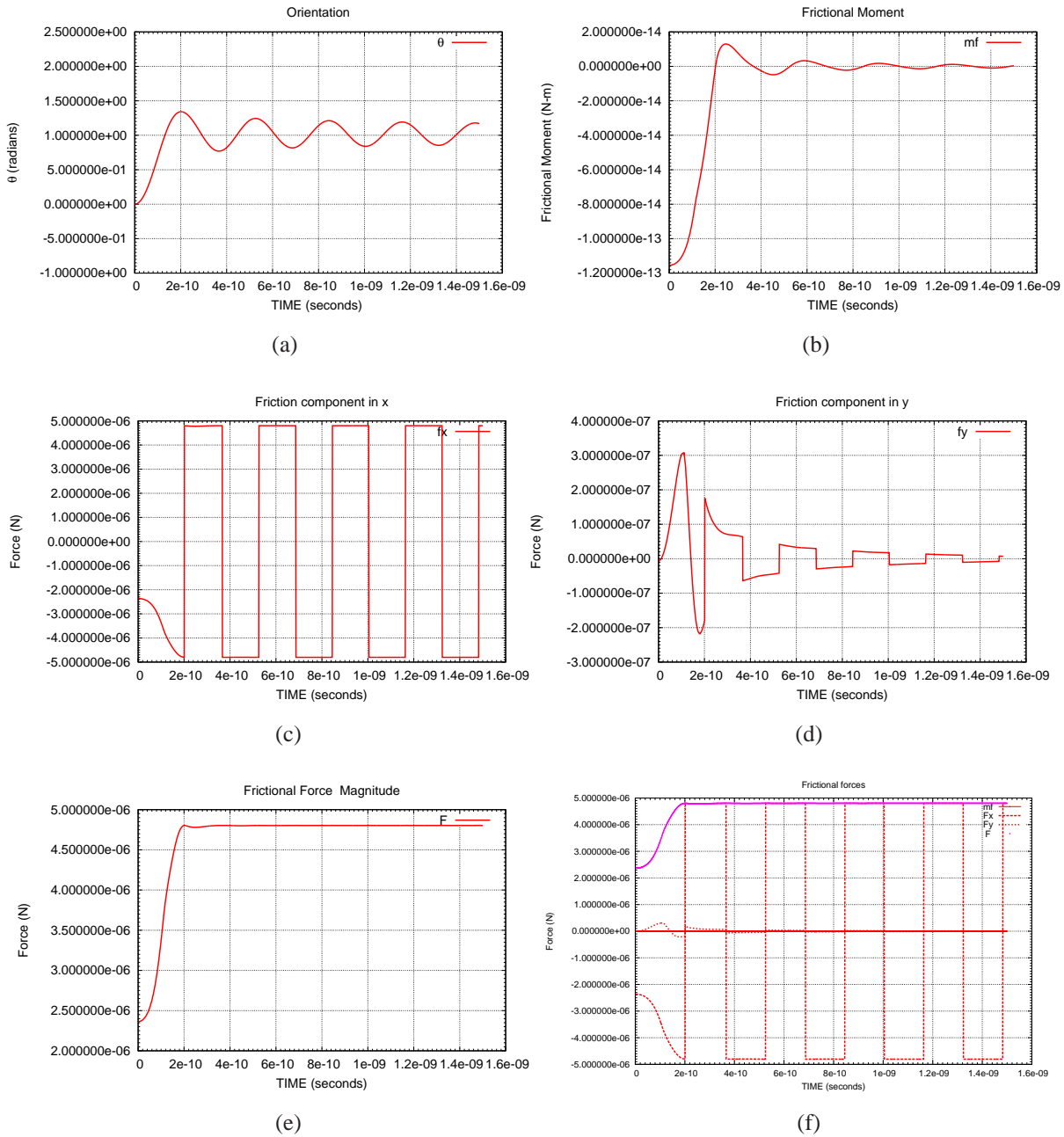
Figure 3.24: Coordinates of Application Force: Xn= 0.275000E-07[m] Yn= 0.450000E-07[m]. Initial Coordinates of C.M: CMx= 0.00E+00[m] CMy= 0.00E+00[m]. Initial orientation: Angle= 0.000000E+00[rad]. Initial velocity in x: Vx= 0.000000E+00[m/s]. Initial velocity in y: Vy= 0.000000E+00[m/s]. Initial angular velocity: ω_o = 0.000000E+00[rad/s]. Pulling/Pushing Force Applied: F= 0.500000E-05[N]. Adhesion Force (VdW): Fvdw= 0.400252E-04[N]. Coefficient Friction: μ= 0.120000E+00 . Object mass: m= 0.623425E-18[kg]. Object dimensions: sa= 0.550000E-07[m] sb= 0.100000E-06[m] sc= 0.550000E-07[m]
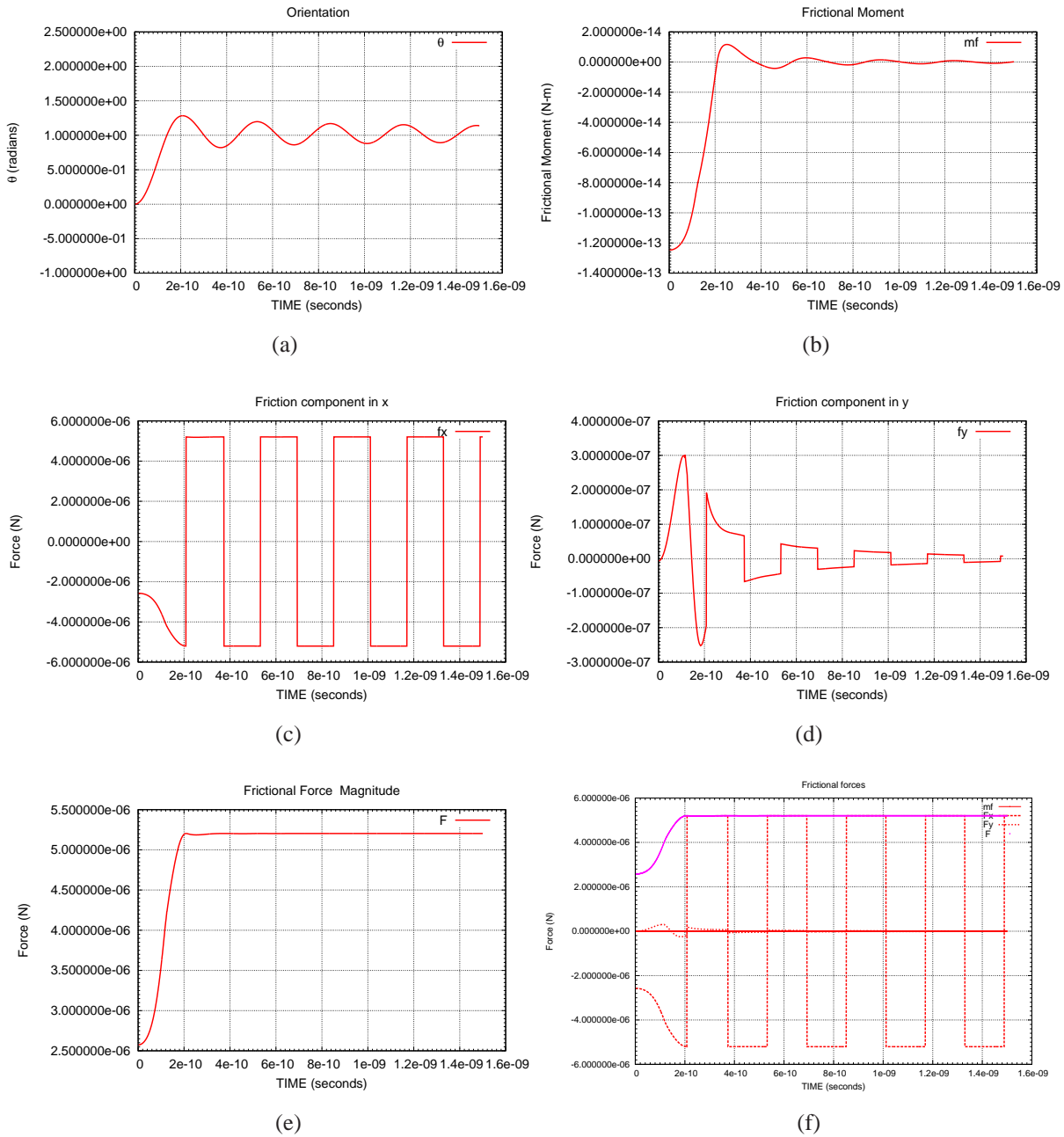
Figure 3.25: Coordinates of Application Force: Xn= 0.275000E-07[m] Yn= 0.450000E-07[m]. Initial Coordinates of C.M: CMx= 0.00E+00[m] CMy= 0.00E+00[m]. Initial orientation: Angle= 0.000000E+00[rad]. Initial velocity in x: Vx= 0.000000E+00[m/s]. Initial velocity in y: Vy= 0.000000E+00[m/s]. Initial angular velocity: ω_o = 0.000000E+00[rad/s]. Pulling/Pushing Force Applied: F= 0.500000E-05[N]. Adhesion Force (VdW): Fvdw= 0.400252E-04[N]. Coefficient Friction: μ= 0.130000E+00 . Object mass: m= 0.623425E-18[kg]. Object dimensions: sa= 0.550000E-07[m] sb= 0.100000E-06[m] sc= 0.550000E-07[m]
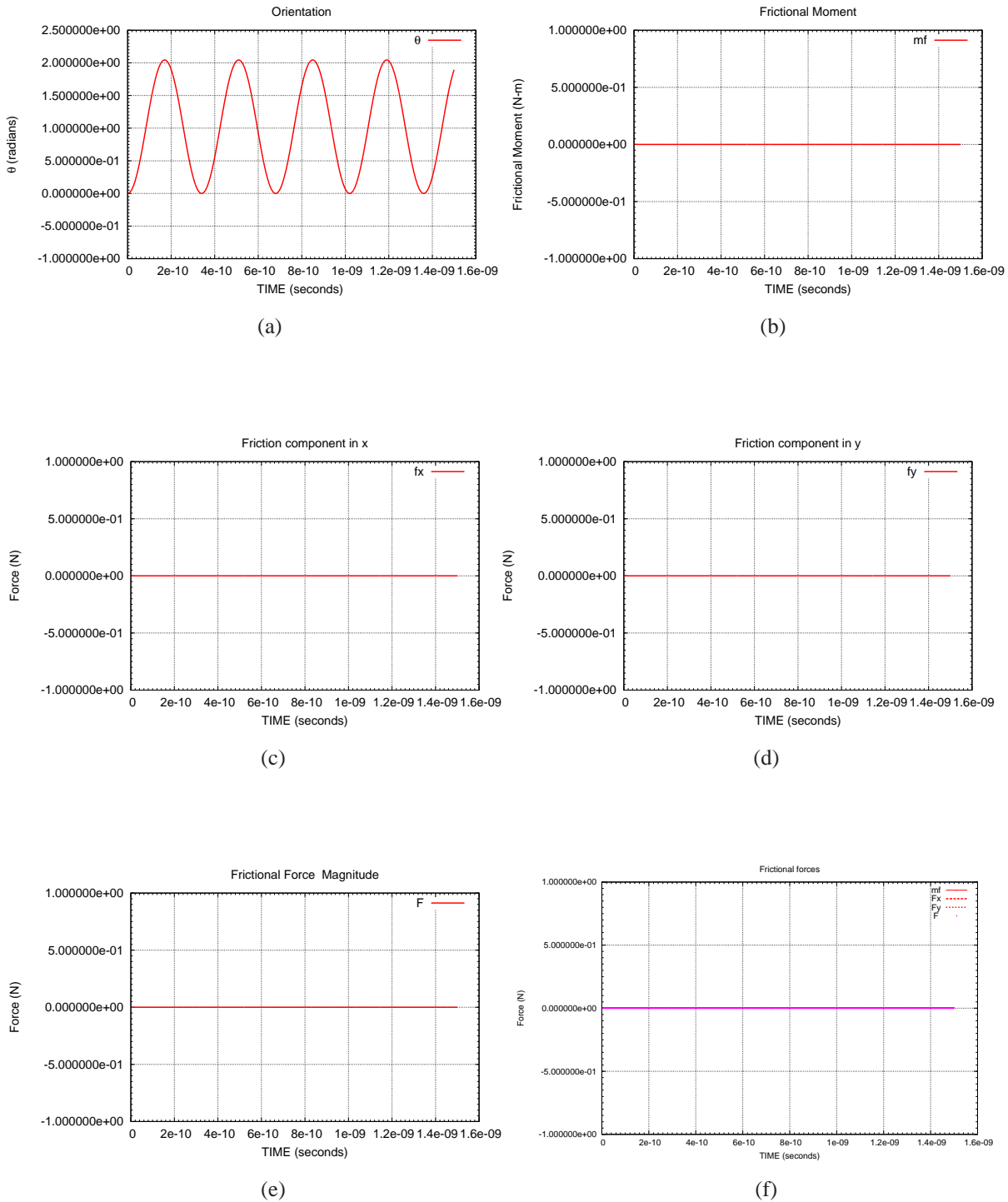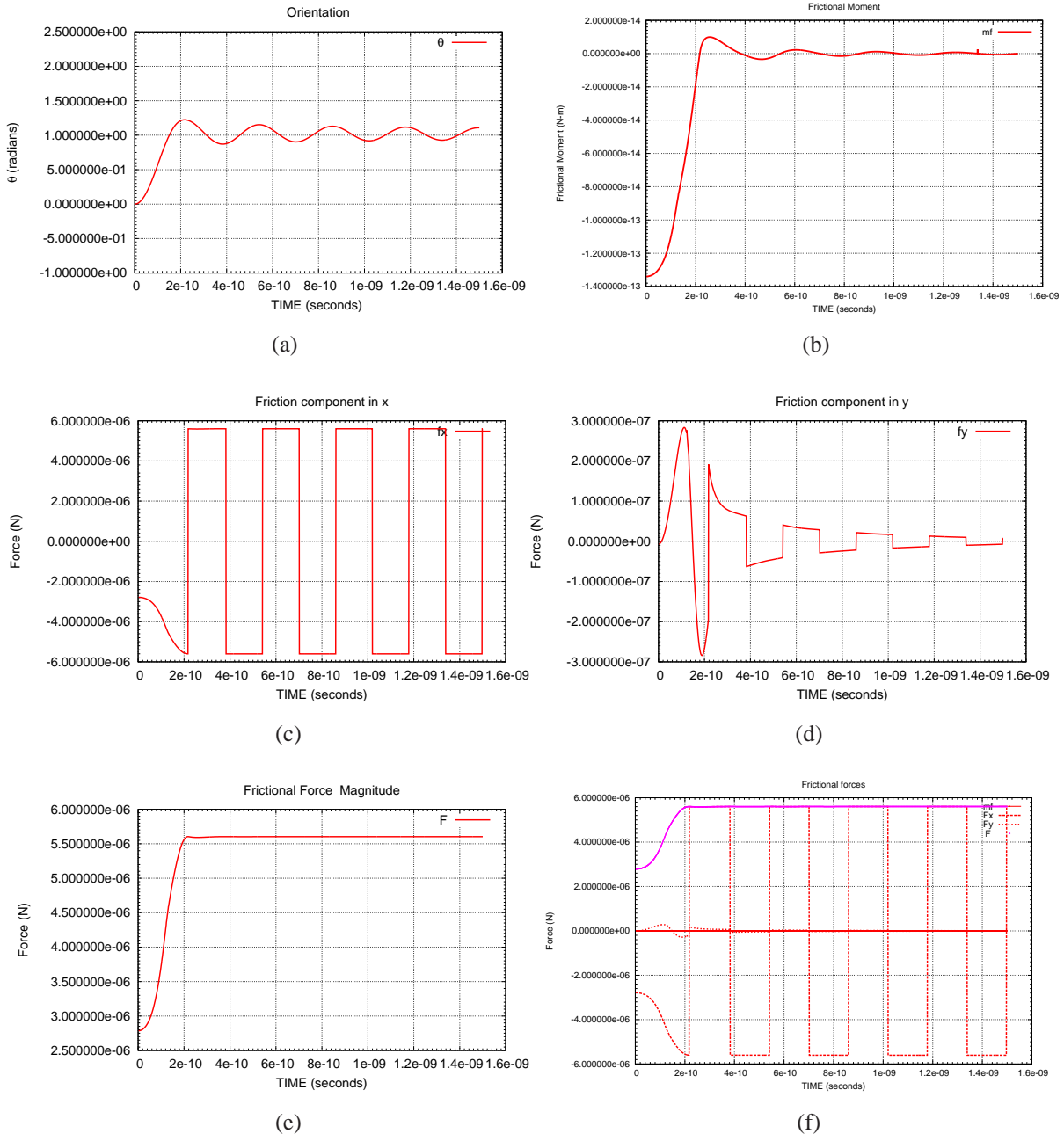
Figure 3.26: Coordinates of Application Force: Xn= 0.275000E-07[m] Yn= 0.450000E-07[m]. Initial Coordinates of C.M: CMx= 0.00E+00[m] CMy= 0.00E+00[m]. Initial orientation: Angle= 0.000000E+00[rad]. Initial velocity in x: Vx= 0.000000E+00[m/s]. Initial velocity in y: Vy= 0.000000E+00[m/s]. Initial angular velocity: ω_o = 0.000000E+00[rad/s]. Pulling/Pushing Force Applied: F= 0.500000E-05[N]. Adhesion Force (VdW): Fvdw= 0.400252E-04[N]. Coefficient Friction: μ= 0.140000E+00 . Object mass: m= 0.623425E-18[kg]. Object dimensions: sa= 0.550000E-07[m] sb= 0.100000E-06[m] sc= 0.550000E-07[m]
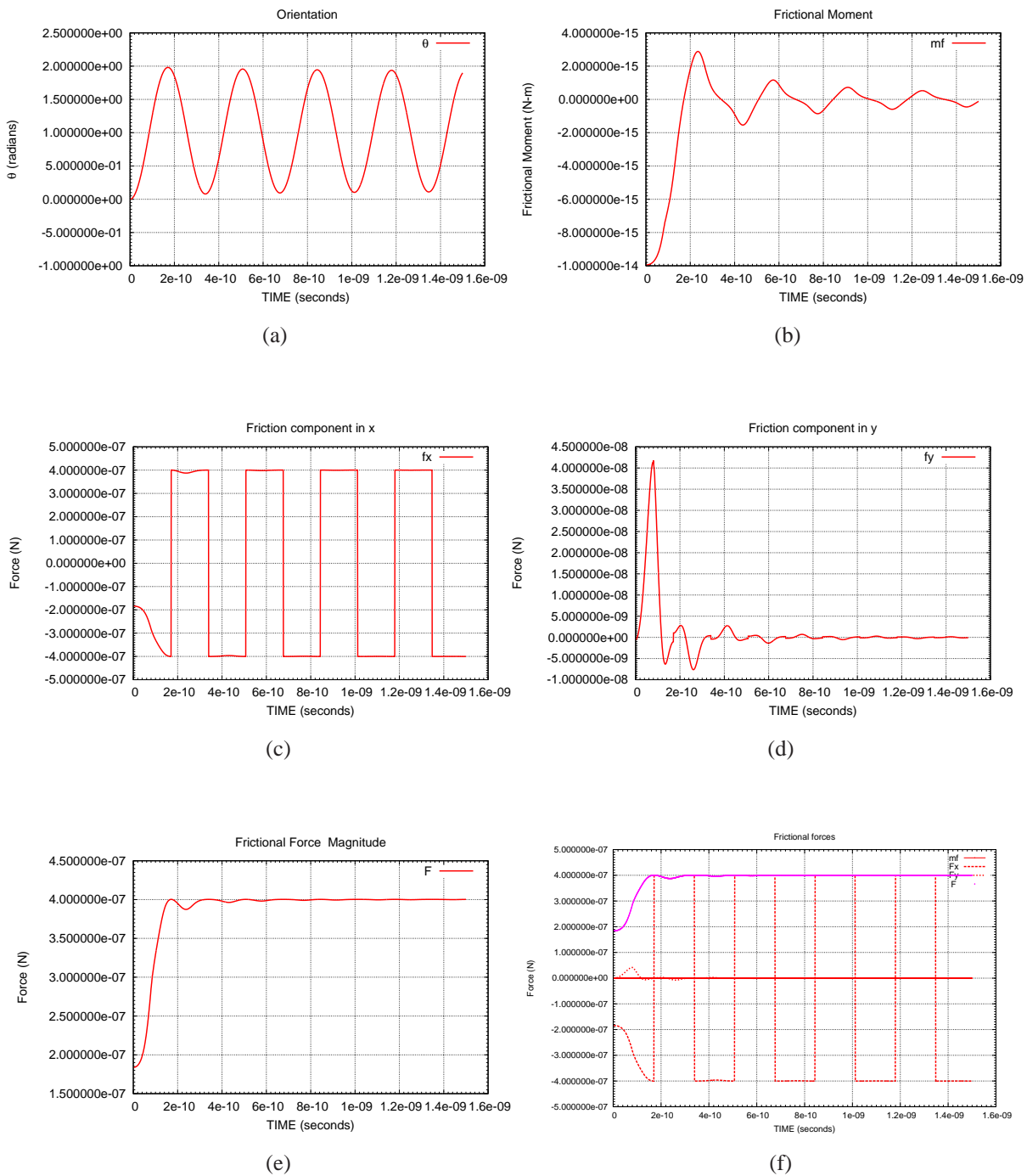
111

(a)

(b)

(c)

(d)

(e)

(f)
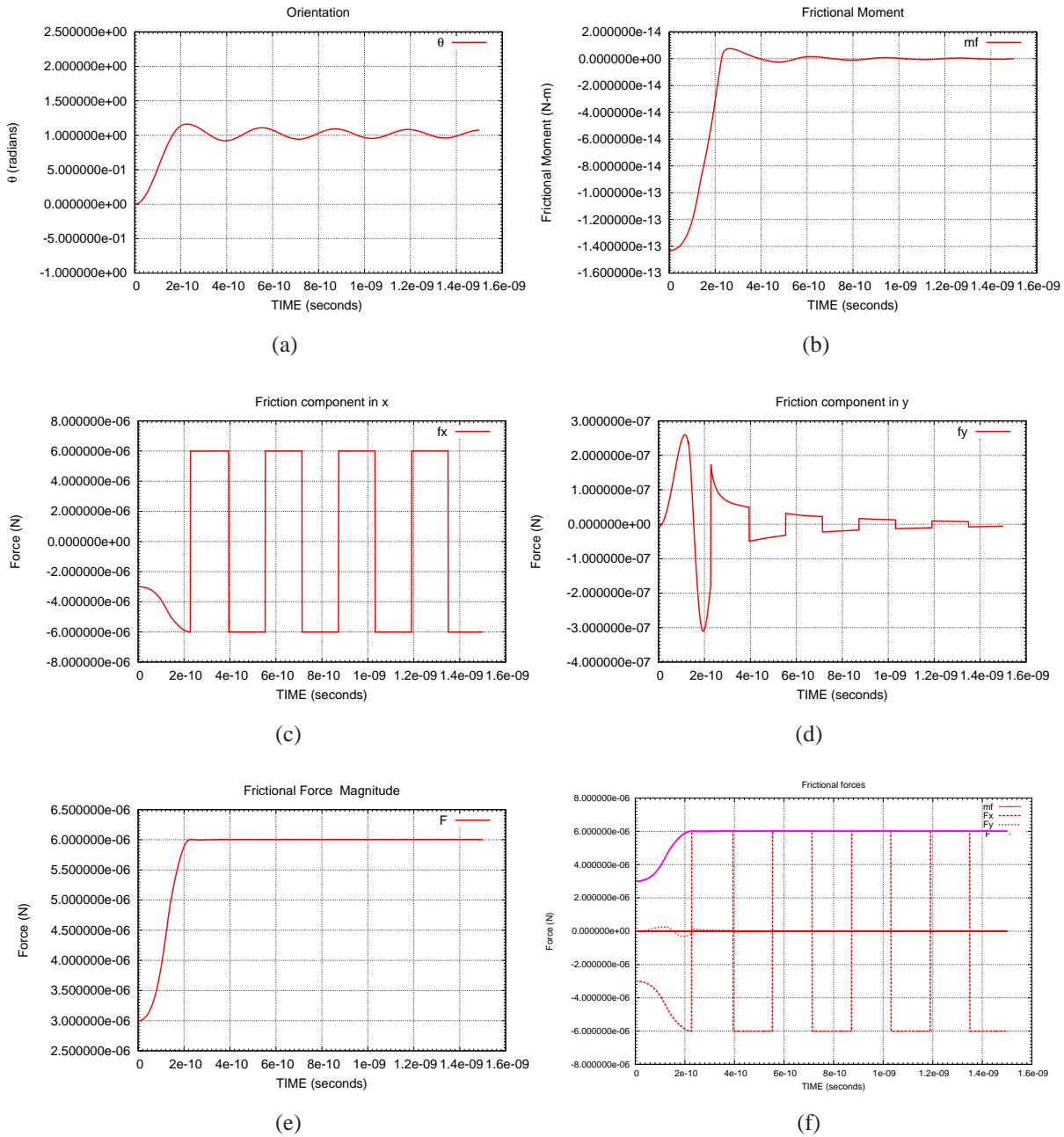
Figure 3.27: Coordinates of Application Force: Xn= 0.275000E-07[m] Yn= 0.450000E-07[m]. Initial Coordinates of C.M: CMx= 0.00E+00[m] CMy= 0.00E+00[m]. Initial orientation: Angle= 0.000000E+00[rad]. Initial velocity in x: Vx= 0.000000E+00[m/s]. Initial velocity in y: Vy= 0.000000E+00[m/s]. Initial angular velocity: ω_o = 0.000000E+00[rad/s]. Pulling/Pushing Force Applied: F= 0.500000E-05[N]. Adhesion Force (VdW): Fvdw= 0.400252E-04[N]. Coefficient Friction: μ= 0.150000E+00 . Object mass: m= 0.623425E-18[kg]. Object dimensions: sa= 0.550000E-07[m] sb= 0.100000E-06[m] sc= 0.550000E-07[m]
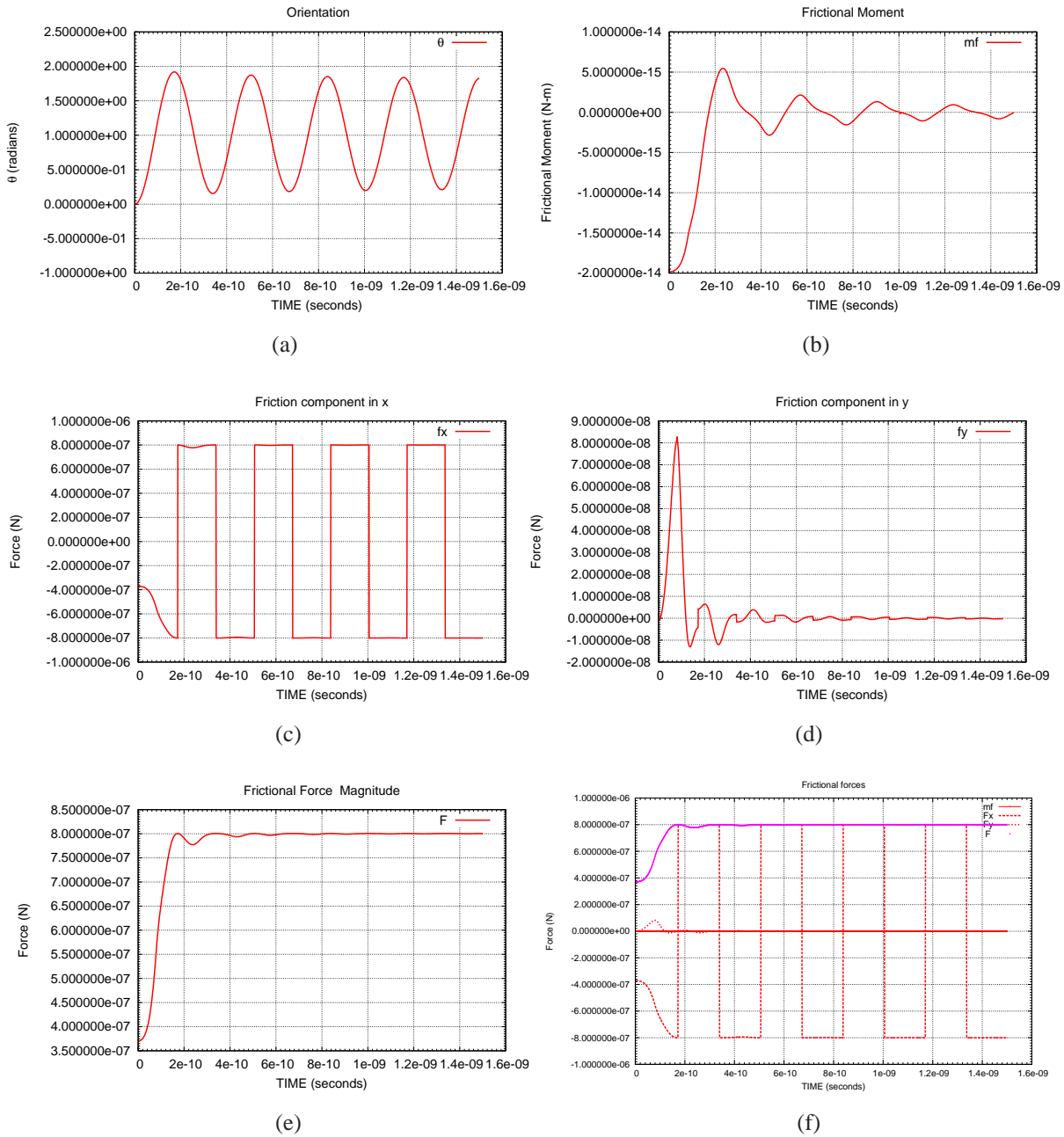
112

(a)

(b)

(c)

(d)

(e)

(f)
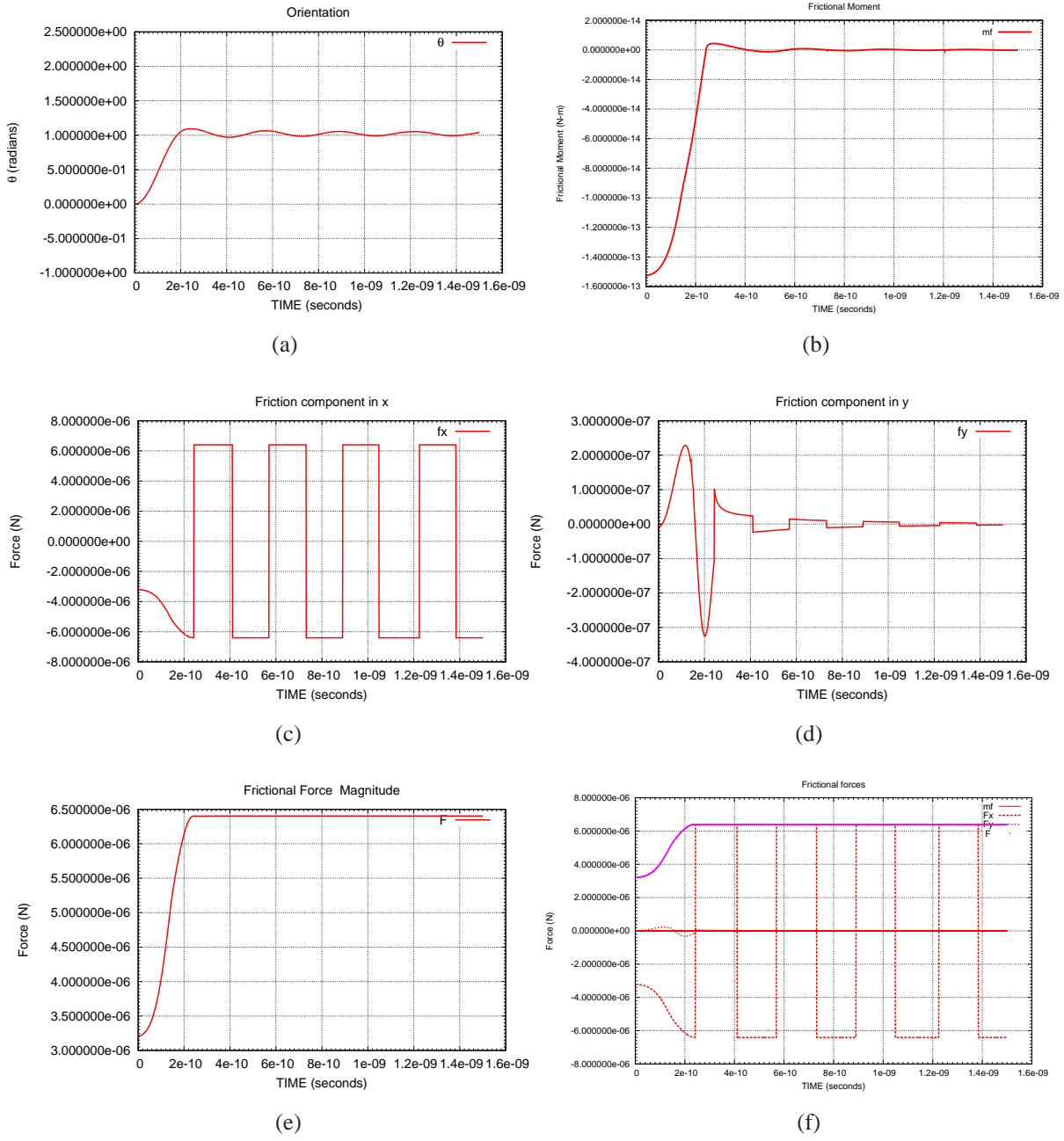
Figure 3.28: Coordinates of Application Force: Xn= 0.275000E-07[m] Yn= 0.450000E-07[m]. Initial Coordinates of C.M: CMx= 0.00E+00[m] CMy= 0.00E+00[m]. Initial orientation: Angle= 0.000000E+00[rad]. Initial velocity in x: Vx= 0.000000E+00[m/s]. Initial velocity in y: Vy= 0.000000E+00[m/s]. Initial angular velocity: ω_o = 0.000000E+00[rad/s]. Pulling/Pushing Force Applied: F= 0.500000E-05[N]. Adhesion Force (VdW): Fvdw= 0.400252E-04[N]. Coefficient Friction: μ= 0.160000E+00 . Object mass: m= 0.623425E-18[kg]. Object dimensions: sa= 0.550000E-07[m] sb= 0.100000E-06[m] sc= 0.550000E-07[m]
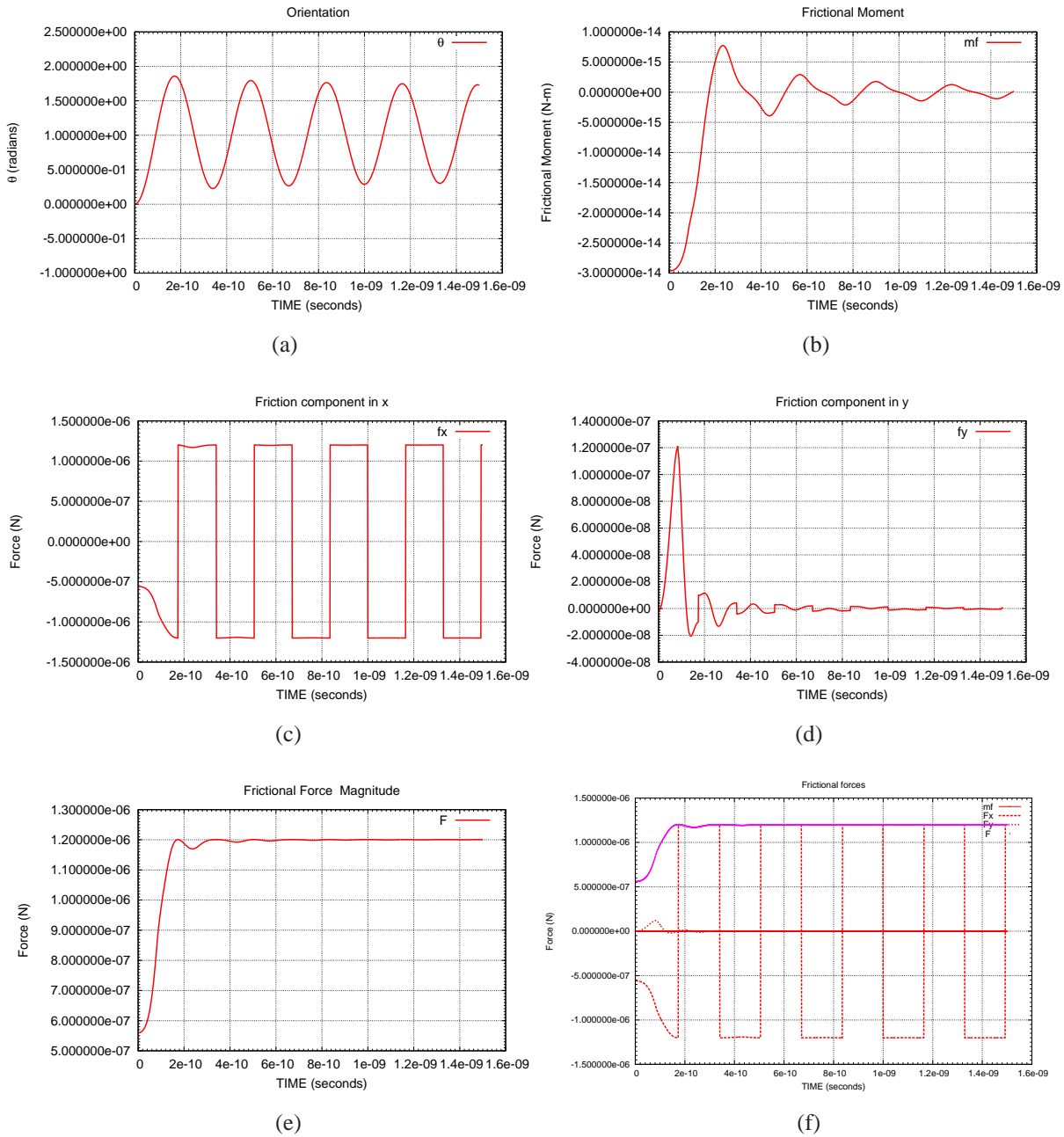
113
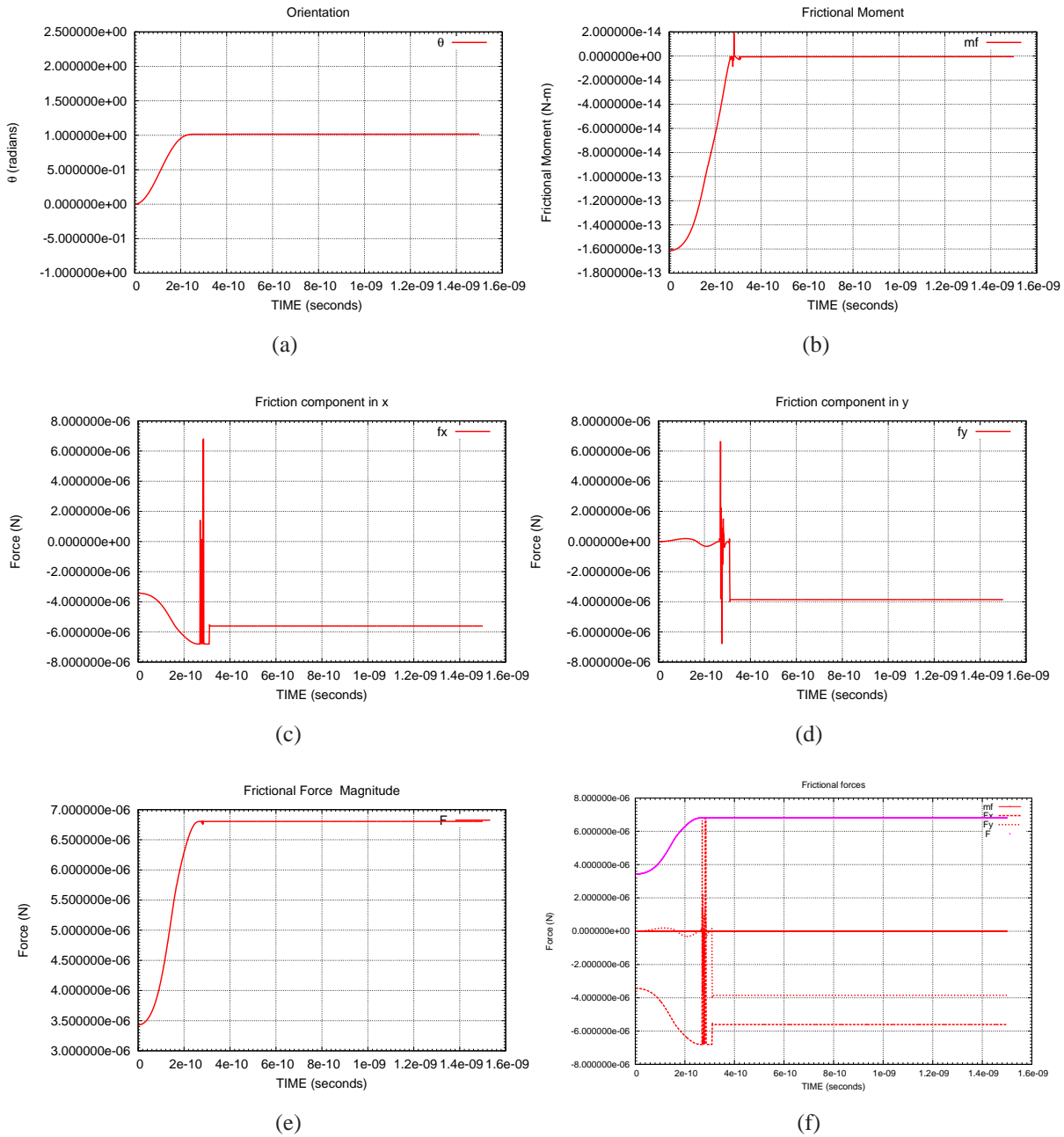
Figure 3.29: Coordinates of Application Force: Xn= 0.275000E-07[m] Yn= 0.450000E-07[m]. Initial Coordinates of C.M: CMx= 0.00E+00[m] CMy= 0.00E+00[m]. Initial orientation: Angle= 0.000000E+00[rad]. Initial velocity in x: Vx= 0.000000E+00[m/s]. Initial velocity in y: Vy= 0.000000E+00[m/s]. Initial angular velocity: ω_o = 0.000000E+00[rad/s]. Pulling/Pushing Force Applied: F= 0.500000E-05[N]. Adhesion Force (VdW): Fvdw= 0.400252E-04[N]. Coefficient Friction: μ= 0.170000E+00 . Object mass: m= 0.623425E-18[kg]. Object dimensions: sa= 0.550000E-07[m] sb= 0.100000E-06[m] sc= 0.550000E-07[m]

114

Figure 3.30: Coordinates of Application Force: Xn= 0.275000E-07[m] Yn= 0.450000E-07[m]. Initial Coordinates of C.M: CMx= 0.00E+00[m] CMy= 0.00E+00[m]. Initial orientation: Angle= 0.000000E+00[rad]. Initial velocity in x: Vx= 0.000000E+00[m/s]. Initial velocity in y: Vy= 0.000000E+00[m/s]. Initial angular velocity: ω_o = 0.000000E+00[rad/s]. Pulling/Pushing Force Applied: F= 0.500000E-05[N]. Adhesion Force (VdW): Fvdw= 0.400252E-04[N]. Coefficient Friction: μ= 0.180000E+00 . Object mass: m= 0.623425E-18[kg]. Object dimensions: sa= 0.550000E-07[m] sb= 0.100000E-06[m] sc= 0.550000E-07[m]
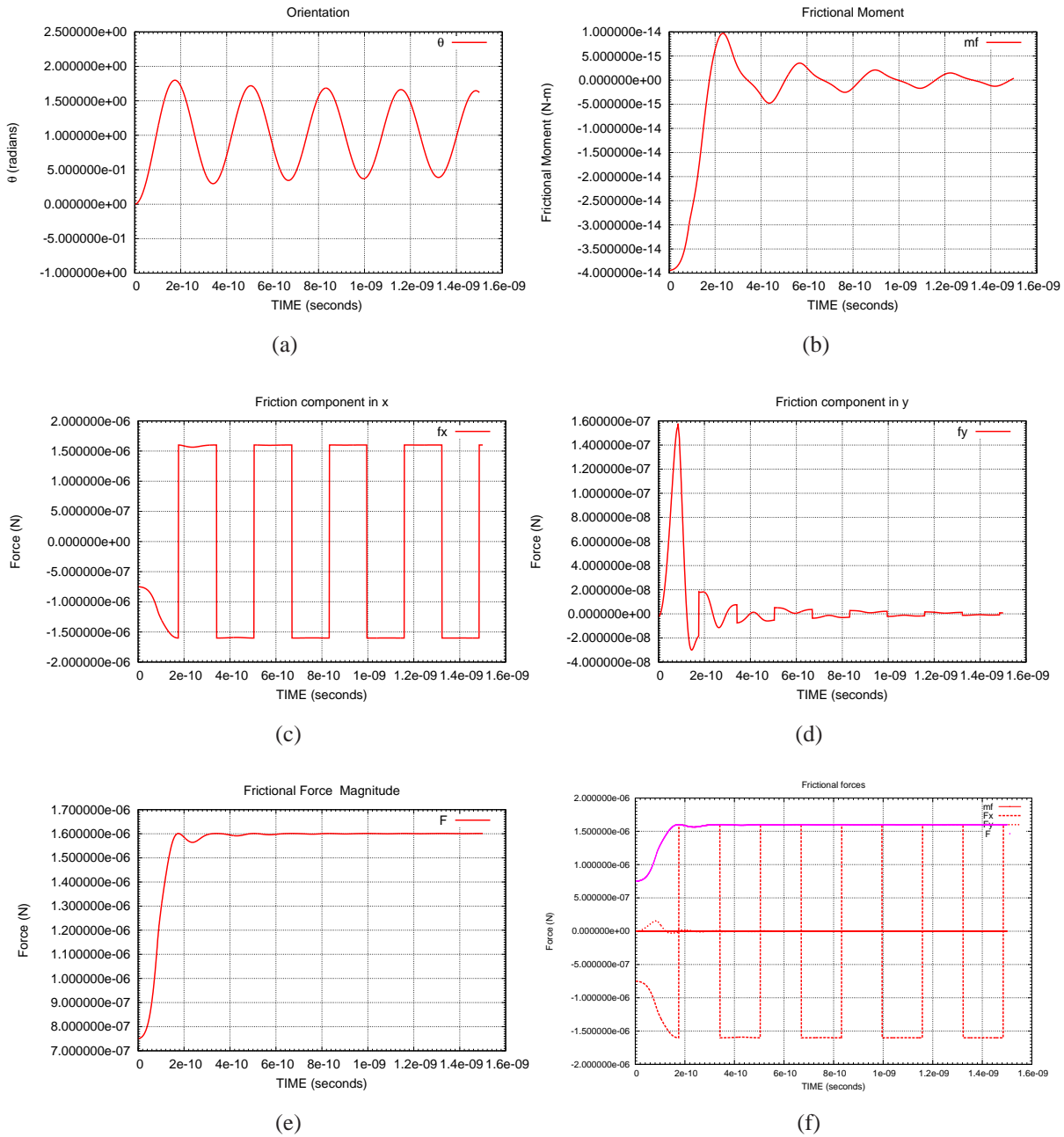
115

(a)

(b)

(c)

(d)

(e)

(f)
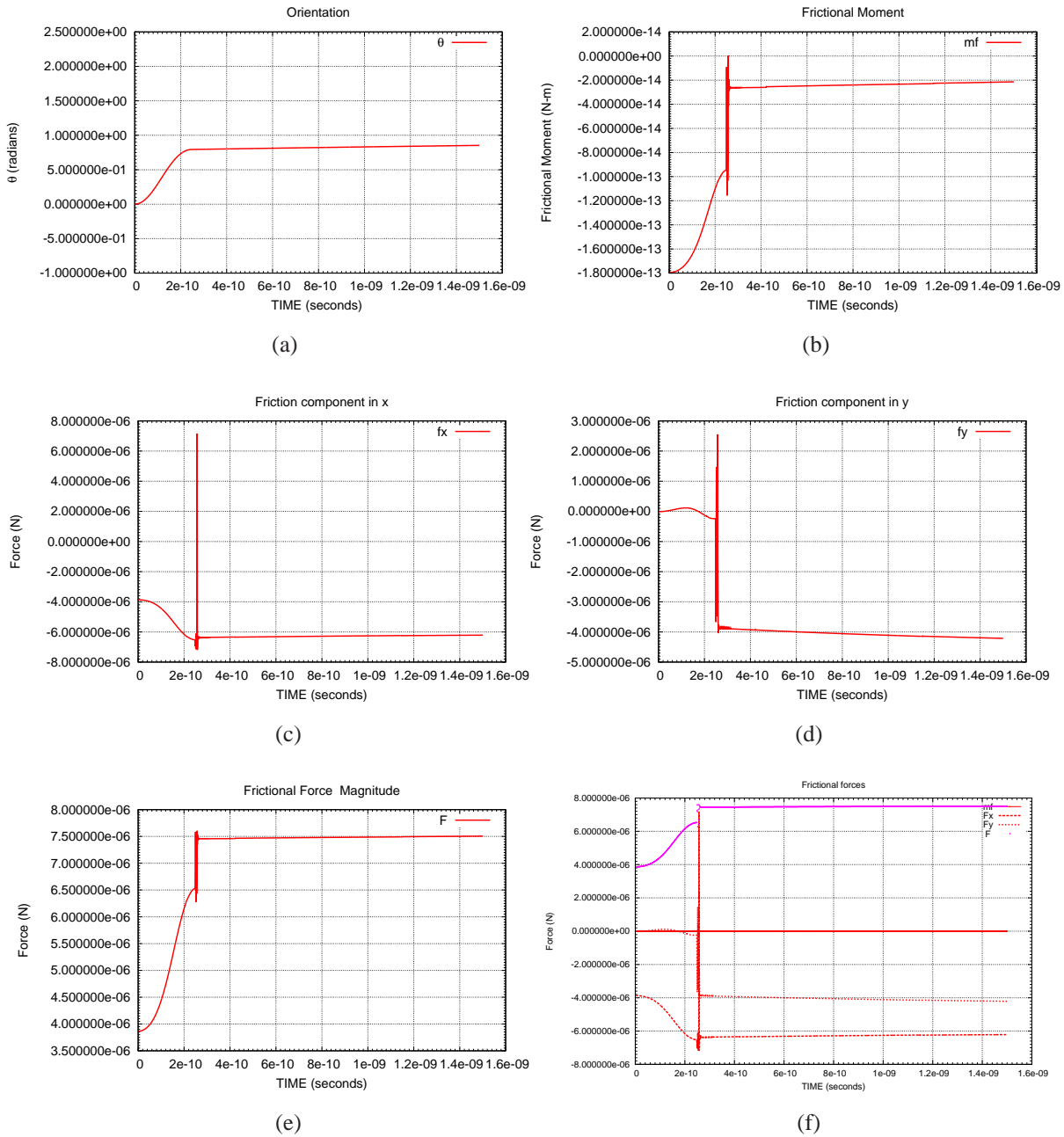
Figure 3.31: Coordinates of Application Force: Xn= 0.275000E-07[m] Yn= 0.450000E-07[m]. Initial Coordinates of C.M: CMx= 0.00E+00[m] CMy= 0.00E+00[m]. Initial orientation: Angle= 0.000000E+00[rad]. Initial velocity in x: Vx= 0.000000E+00[m/s]. Initial velocity in y: Vy= 0.000000E+00[m/s]. Initial angular velocity: $\omega_o = 0.000000E+00$[rad/s]. Pulling/Pushing Force Applied: F= 0.500000E-05[N]. Adhesion Force (VdW): Fvdw= 0.400252E-04[N]. Coefficient Friction: μ= 0.190000E+00 . Object mass: m= 0.623425E-18[kg]. Object dimensions: sa= 0.550000E-07[m] sb= 0.100000E-06[m] sc= 0.550000E-07[m]
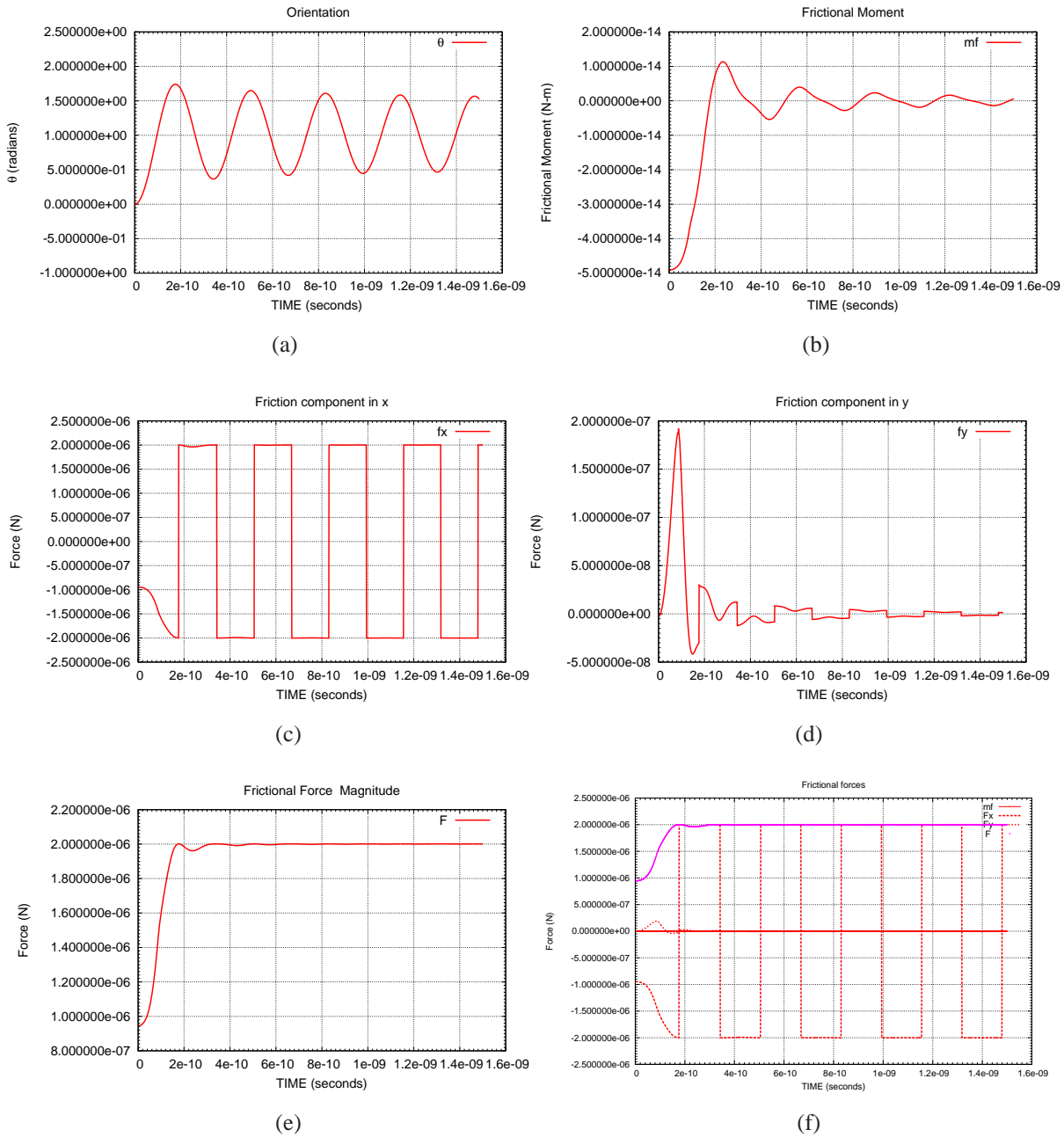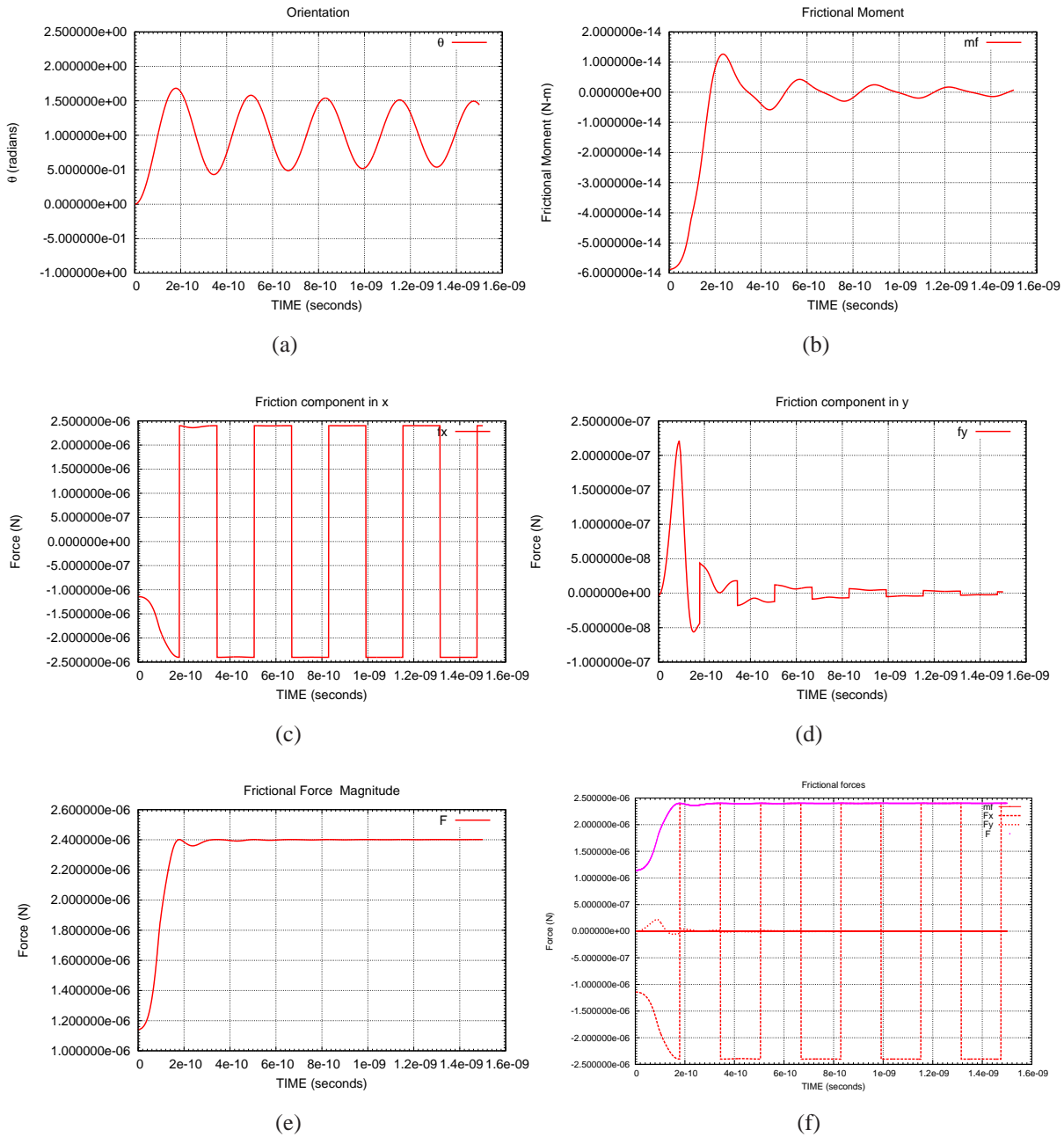
116
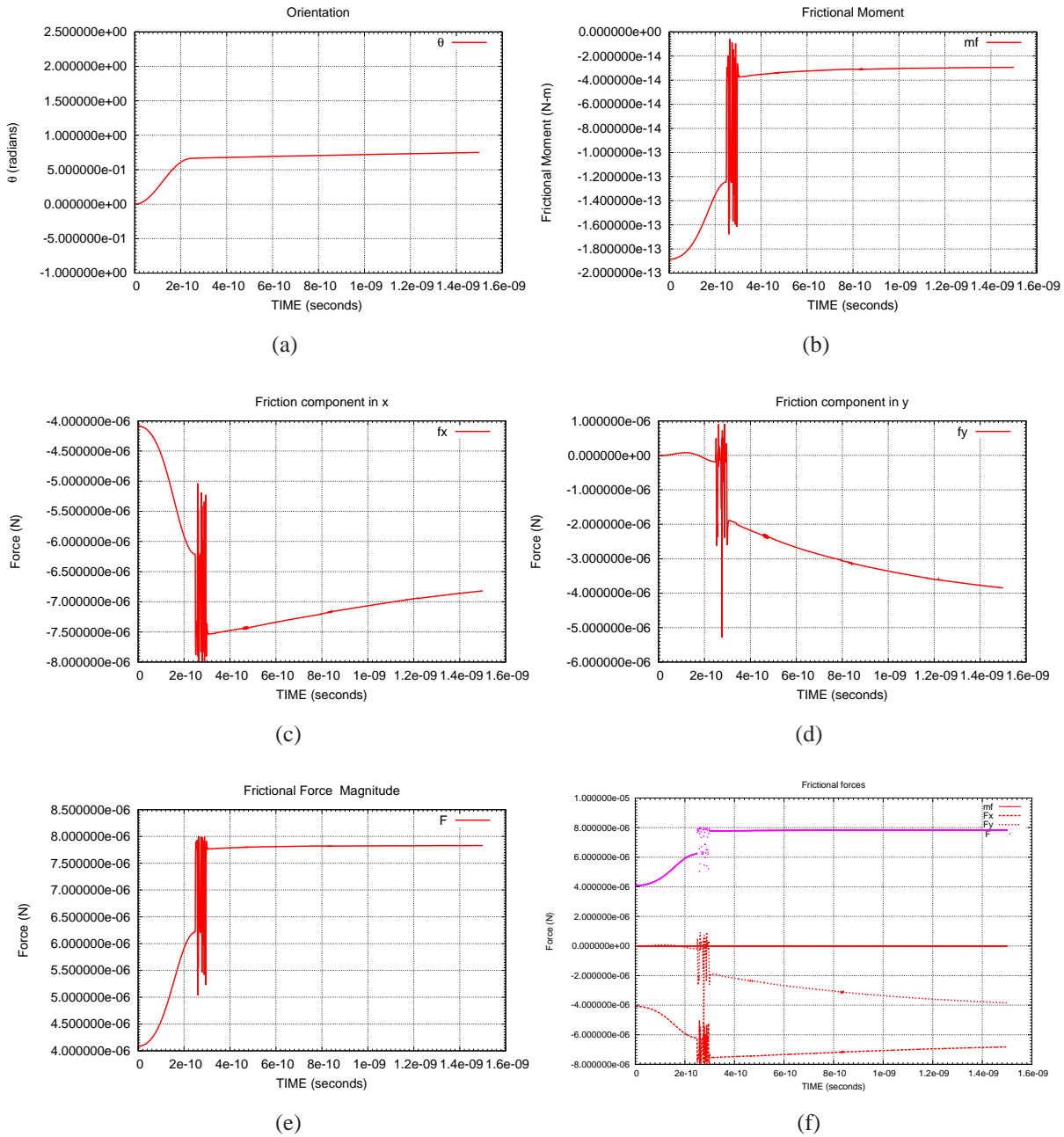
Figure 3.32: Coordinates of Application Force: Xn= 0.275000E-07[m] Yn= 0.450000E-07[m]. Initial Coordinates of C.M: CMx= 0.00E+00[m] CMy= 0.00E+00[m]. Initial orientation: Angle= 0.000000E+00[rad]. Initial velocity in x: Vx= 0.000000E+00[m/s]. Initial velocity in y: Vy= 0.000000E+00[m/s]. Initial angular velocity: ω_o = 0.000000E+00[rad/s]. Pulling/Pushing Force Applied: F= 0.500000E-05[N]. Adhesion Force (VdW): Fvdw= 0.400252E-04[N]. Coefficient Friction: μ= 0.200000E+00 . Object mass: m= 0.623425E-18[kg]. Object dimensions: sa= 0.550000E-07[m] sb= 0.100000E-06[m] sc= 0.550000E-07[m]

117

3.5 Summary

This Chapter presented the developed equations to characterise the full motion of objects at the nanoscale. Proposed models were simulated using high accuracy integration techniques such as the **Bulirsch-Stoer Method**, implemented on FORTRAN. It is been shown that in general the motion of the objects is a combination of translation and rotation. This can explain the stick-slip problem broadly observed for objects at different scales. Rolling and sliding motion can still exist even if the frictional force is equal to zero. The effect of adhesion is greater for objects rolling than for those that slide. Therefore, in terms of energy and force to manipulate objects at te nanoscale, pushing or pulling operations are preferred as they minimise the energy necessary to move the nano-object. On the other hand, the location of the applied pushing/pulling force has a direct relation with the resulted motion of the nano-object. Finally this chapter generated new values of surface energy of some materials as well as a corrected equation that can be used to calculate the surface energy parameter γ which in some cases was close to those experimentally obtained in the literature.

Chapter 4

The instantaneous centre of rotation of objects at nanoscale (iCOR)

4.1 Introduction

In this chapter a new analysis to calculate the location of the instantaneous centre of rotation (**iCOR**) for an object in quasi-static motion at nano-scale is presented. The new model which expands the proposed model by Pham and Cheung at macroscale is then developed for objects at the nanoscale using continuum mechanics [77]. Also, a similar methodology is followed because of its relevant and simplicity and the richness of information that it provides. To validate our model, the results are compared with those reported in the literature.

The motion of an object on a surface (plane) acting under an external force can be described by the instantaneous centre of rotation (**iCOR**). Since the motion of the object may be expressed in terms of translation, rotation or a combination of both, it can be referenced to a fixed point in space on the plane of motion that maintains a constant distance from every point of the object. This fixed point that exists at every instant of the object's motion and is called the *instantaneous centre of rotation* (**iCOR**).

From previous paragraphs, it could be inferred that there should exist a relation between the **iCOR** and the location of the pushing or pulling force as well as its magnitude as applied to the object. Also, given that this analysis is being used to describe macro scale objects it raises the question as to whether these models will predict the motion of objects at the nanometre scale. Since the object's size is almost the size of an elementary particle that constitutes them, this means that the forces at the nanoscale are more electrostatic in the origin.

The motion of nano-objects such as single-walled carbon nanotubes **CNT**, multi-walled carbon nanotube **MWCNT** and nanorods is mostly described by experiment. A study of a different shape of nano-objects is presented by Sitti, who studied the motion of spherical objects (nano spheres) relative to their nano-tribological properties. In his work, the dynamics of the nano-objects are mixed with the dynamics of the manipulator obtaining values that could not corespond in the totality to the dynamics of the manipulated objects [52]. On the other hand, only a few articles can provide consistent analytical models to describe the behaviour of the manipulated nano-object and also they are restricted to the modeling of quasi-static motion.

Therefore, the analysis and development of equations to predict nano-objects' motion which describe the relation between the **iCOR** location and the effective pushing force magnitude-location being applied is presented. The properties of the **iCOR** are analysed and compared with different developed models in the area for the quasi-static motion of nanoscale objects. This analysis is easily applied to different nano structures such as nanorods, carbon nanotubes **CNT**, nanobars, and nanocubes. All of them are assumed to have a rectangular or square contact area. It is also assumed that Coulomb's law of friction model is still a valid one to describe motion at the nanoscale. In addition, the difference between shear stress and the frictional force is discussed and clarified.

4.2 Quasi-static motion at the nanoscale: methods to calculate the instantaneous centre of rotation (iCOR) for nano-objects

Quasi-static motion describes mechanical systems where the motion of the object acting under an effective force is considered enough to start object's motion and at the same time the effects of the inertia in $F = ma$ are negligible (mass or acceleration are sufficiently small) [78]. Quasi-static conditions were assumed to exist in a very short period of time ($t \approx 0\,sec$), once the object started its motion. Furthermore, the applied force is always balanced by the frictional force acting on the contact between the object and the surface. The previously mentioned properties are very useful tools when calculating an unknown pressure distribution on the contact area with a uniform friction force when it is combined with high-precision integration algorithms.

The analysis of the **iCOR** for objects at the nanoscale such as nanorods and carbon nanotubes has been introduced and discussed in early works. According to these works, methods to calculate the **iCOR** could be mainly divided in two methodologies; the first one corresponds to calculate it by *experimentation*, whereas the second methodology is based on continuum mechanics combined with *the minimum power principle* studied by Peshkin and Sanderson [78].

4.2.1 Method 1: Experimental determination of the iCOR

A series of experiments are arranged where the information generated is analysed and characterised to find the nano-objects motion. This characterisation is achieved by applying a curve fitting technique to the recorded force-displacement data obtained from the manipulation process. An example of this method is presented by Jung-Hui and Shuo-Hung [79], where the **iCOR** for multi-walled carbon nanotubes **MWCNT** during lateral pushing operations was determined. Images were taken before and after the **MWCNT** manipulation was done and, then the two images overlapped to determine the **iCOR** location. Finally, a graph

with the observed **iCOR** location and the pushing point location was constructed in order to obtain a dimensionless fitting function. The derived relation after applying the fitting curve approximation to the obtained experimental dataset is shown in Equation 4.1.

$$\alpha = 0.5\sqrt{\beta - 0.5} \quad , \beta > 0.5 \tag{4.1}$$

where $\alpha = \frac{\rho}{L}$ and $\beta = \frac{x}{L}$ are the normalized values for the **iCOR** and the lateral pushing locations, respectively. L is the **MWCNT** length, and x is the longitudinal distance from the pushing point and the lower end of the **MWCNT**. ρ is the longitudinal distance between the lower end of the **MWCNT** and the determined **iCOR**. In addition, the experimental conditions and the schemes of manipulation can interfere with the real motion of the nano-object providing results limited to the experimental set-up and misleading as they overestimate the parameters values, leaving a gap in knowledge of the true object motion and its tribological properties.

4.2.2 Method 2: Frictional moment analysis and the minimum energy principle

In-plane rotations of objects were observed to occur about a point of the object support. This point of support can be associated with the location of the **iCOR**, as this point satisfied the conditions mentioned by Huntington in [80]. On the other hand, *the minimum energy principle* stated the conditions when the motion of the object due to the effective force applied is just sufficient to produce a motion as dissipative forces (**i.e.** the frictional forces) are still dominant. These two principles provide a useful tool for solving the location of the **iCOR** at macro, micro and nano scale.

4.2.2.1   Analysis of moments taken around the point of applied force

Falvo et al. in [69] manipulated **MWCNT** by using an **AFM** probe to apply lateral forces at different locations. This generated two types of motions in the **MWCNT**: rolling and sliding. In dealing with **MWCNT** sliding motion, two additional motions were observed: in-plane-translations and in-plane-rotations. Particular to **MWCNT** in-plane-rotations, he analysed the relation between the point of manipulation and the observed pivot point or **iCOR**. Thus, by taking moments around the applied point of the pushing force and solving for the motion that minimises the energy loss due to friction, the follows relation results

$$\dot{x}_o = \dot{x}_1 - \sqrt{\dot{x}_1^2 - \frac{1}{2}(2\dot{x}_1 - 1)} \tag{4.2}$$

where L is the length of the **MWCNT**. $\dot{x}_o = \frac{x_o}{L}$ is the calculated **iCOR** location measured from the lower end of the **MWCNT** and the location of the **iCOR**. $\dot{x}_1 = \frac{x_1}{L}$ is the normalised distance between pushing point and the lower end of the **MWCNT**. Equation 4.2 describes the relation between the point of applied force and the observed pivot point as being in almost good agreement with the observed **MWCNT** in-plane rotations.

4.2.2.2   Analysis of moments taken around the iCOR

Taking moments around the **iCOR** is presented to model in-plane rotations of objects at macro scale by Pham et al. [77]. In this strategy, the moments due to the frictional force and the effective resultant force are taken with respect to an assumed **iCOR** location. After solving the equation of motion for the pulled/pushed force, the equation is derivated and equated to zero by using the 'minimum effort criteria'(minimum power principle). The calculated **iCOR** locations values were similar with those reported when moments of forces are taken around the point of applied force.

Li et al. presented a similar analysis to model the behaviour of nanorods and nanowires [6]. Furthermore, in the case of nanowires it was noticed that when nanowires of a certain aspect

ratio (diameter/length) they behaved as a rigid segment line like nanorods. Thus, this developed analysis can describe in-plane rotations for both types of nano-structures under lateral pushing operations produced by an **AFM**-probe (*see* Eq. 4.3).

$$S = \begin{cases} l + \sqrt{l^2 - lL + \frac{L^2}{2}} & \text{, when } l < \frac{L}{2} \\ \\ l - \sqrt{l^2 - lL + \frac{L^2}{2}} & \text{, when } l > \frac{L}{2} \end{cases} \tag{4.3}$$

where l is the longitudinal distance between the left end of the nanorod and the location of the pushing force, L is the length of the nanorod and S is the **iCOR** location measured referenced to the left end of the nanorod. An extension of this methodology is used by Wu et al. [81] to model the behaviour of manipulated **MWCNT** and also to investigate their Young's moduli and tribological aspects. The manipulation is used to drag the **MWCNT** onto pre-etched micro trenches in order to measure their Young's moduli by the three-point bending method.

All previously mentioned works are restricted to modelling only in-plane rotations of the nano-object, not providing a description of the nano-object during pure sliding motion. In addition, in these methodologies the challenge is to define the model to describe the friction force at the nano scale as friction is extremely debated area. Also, the use of the minimum energy principle is only valid for frictional models that obeys the Coulomb friction model. As a result, the above methods could validate the idea that the Coulomb friction model is still valid at the nano-scale.

Limitations in previous methodologies are covered in this research such as developed models based on classic mechanics proposed by Pham and Cheung (**i.e.** taking moments around the iCOR). The corresponding modelling forces atthe nanoscale (**i.e.** Van der Waals forces) are introduced bellow.

4.2.3 Developed Quasi-static motion analysis extension to nano scale

The proposed model for the sliding frictional force expands the Coulomb's friction model by modelling the adhesion component due to the Van der Waals forces at the load (normal force) $F_f = \mu(mg + F_{VdW})$. This analysis was developed to determine the nano-objects' motion behaviour in terms of the **iCOR** position when a minimal force acts on it. Also, the minimum force to be applied to the nano-object that causes in-plane rotation is calculated.

The effective forces modelled acting on a manipulated rigid nanorod and their parameter interpretation are shown in Figure 4.1, where **F** is the pushing/pulling force applied at the point **Q**, y_n is the distance between the applied force and the nanorod centre of mass (**C.M.**), f_1 and f_2 are the resultant frictional forces acting in opposite directions respectively, **2b** is the nanorod's length, **R** is the distance between the **iCOR** (point **C**) and the nanorod centre of mass **C.M.**, point **A** and **B** representents the ends of the nano rod, respectively.

To start, the **iCOR** position is assumed to be located at some point **C** about the nanorod contact length at **R** distance from the nanorod centre of mass **C.M.**. The frictional force is assumed to be uniform between the nanorod and the supporting surface. Also, it obeys *Coulomb´s friction law*. Thus, assuming the nano rod begins to turn about the **iCOR**, the frictions due to each point of contact on opposite sides of the **iCOR** (sides **AC** and **CB**) will act in opposite directions.

The frictional forces f_1 and f_2 represents the resultant frictional force on each line of segment acting at its middle point of **CB** $(b + R)/2$ and middle point of **CA** $(b - R)/2$, respectively. Also, the frictional forces acting between the point **C** and **B** have a resultant: $f_1 = \frac{(b+R)}{2b}\mu(T_{otal}\,L_{oad})$, which acts at the middle point of **CB**. Similary the friction on **CA** acts thorugh the middle point of **CA** and its resultant magnitude is: $f_2 = \frac{(b-R)}{2b}\mu(T_{otal}\,L_{oad})$, which acts at the middle point of **CA**.

<div align="center">125</div>

Finally, arranging the frictional forces terms and substituiting the total load value, their respective magnitudes are defined by Equation 4.4 and Equation 4.5.

$$f_1 = \mu \left[mg + F_{VdW} \right] \times \left[\frac{(b+R)}{(2b)} \right] \tag{4.4}$$

$$f_2 = \mu \left[mg + F_{VdW} \right] \times \left[\frac{(b-R)}{(2b)} \right] \tag{4.5}$$

where, m is the mass of the nano-object (nanorod) which is calculated from the relationship $\rho = m/V$, where ρ is the material density and V is its geometric volume, μ is the coefficient of friction, g represents the constant of gravity of Earth taken as $9.81 \, [m/s^2]$, F_{VdW} the adhesive force due to the Van der Waals forces, **b** and **R** represent the geometrical paremeters defined in Figure 4.1.

The Van der Waals interaction force between a thin nanorod and a plane is given by Parsegian in [82] as $F_{VdW} = 2b(Hd^{1/2}/16z_o^{5/2})$; where $2b$ is the length of the nanorod, d represents the nanorod's diameter, z_o represents the distance between the nanorod and the surface in contact which can be considered equal to the interlayer spacing of the surface material ($z_o = 0.2nm$) in contact with the surface, and H represents the material's Hamaker constant.
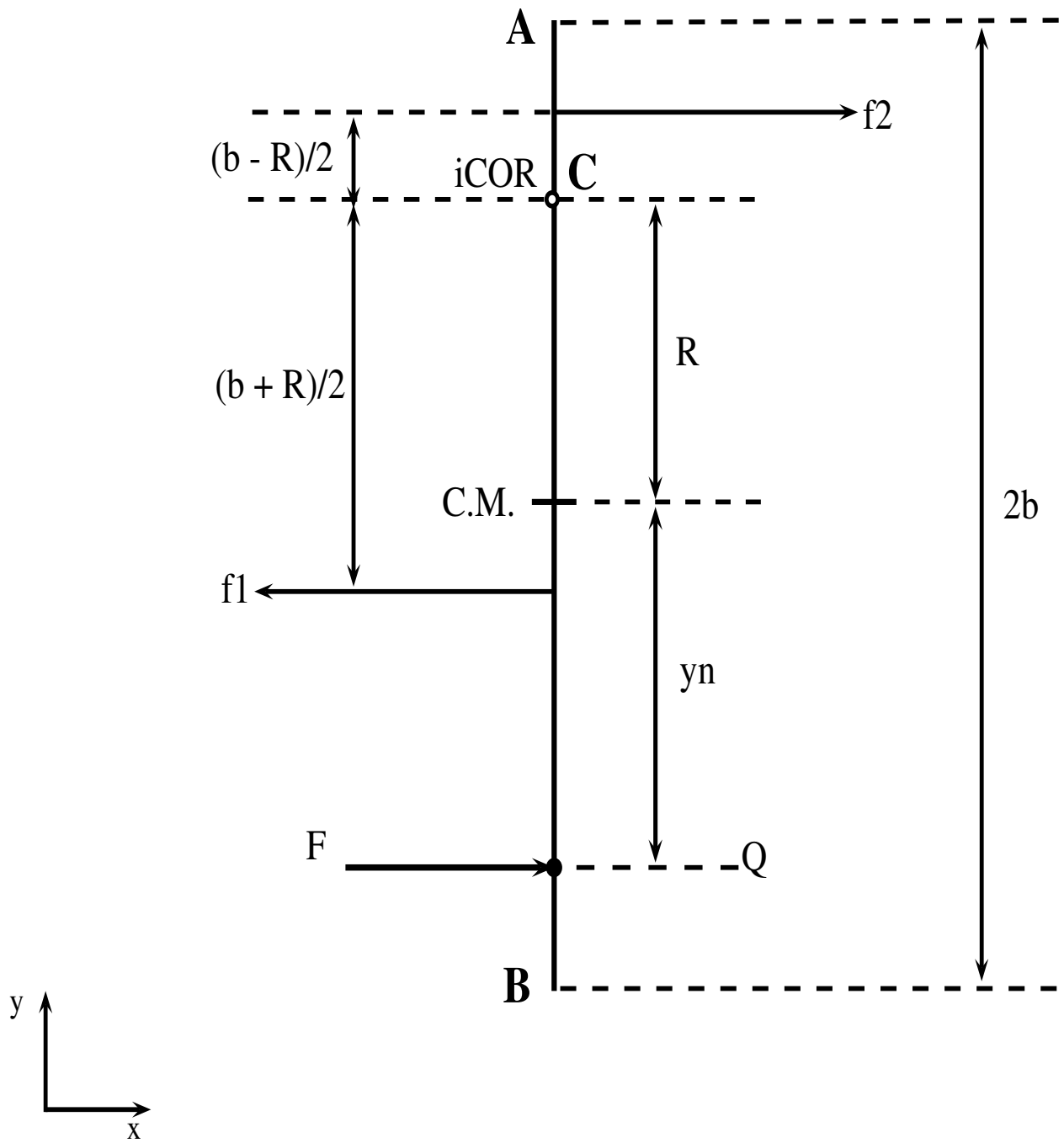
Figure 4.1: Analysis of forces and parameters description to calculate the **iCOR**.

In this Chapter, the developed analysis of the object's motion is presented without the use of constrains by modelling the forces and moments acting on the nano-object as defined in Equation 4.6. Thus, Equation 4.6 provides a starting equation to model the **iCOR** position under two different pressure conditions. These conditions correspond to unknown and known pressure distributions between the nanorod and the plane where motion takes place. For the case of unknown pressure distribution, any pressure distribution could be assumed. Whereas in the second case, a symmetric and distributed pressure distribution is assumed.

Taking moments about the assumed **iCOR** location for quasi-static motion (see Figure 4.1)

$$F \times (R + y_n) - f1 \times \left(\frac{b+R}{2}\right) - f2 \times \left(\frac{b-R}{2}\right) = 0 \tag{4.6}$$

4.2.3.1 Location of the iCOR for known pressure distribution

The new equation to calculate the location of the **iCOR**, when the pressure distribution is known, is obtained by taking Equation 4.6 and solving for **R**

$$R = \frac{bF + \sqrt{b^2 F^2 - \mu(mg + F_{VdW})\big(\mu(mg + F_{VdW})b^2 - 2by_n F\big)}}{\mu(mg + F_{VdW})} \tag{4.7}$$

From Equation 4.7, the value of R is the function of the pushing/pulling force **F**, coefficient of friction μ, and the location of the applied force y_n. So, $R(\mu, y_n, F)$ is a useful relationship to explore in detail. Also, from Equation 4.7, the value of **F** is unknown, but it could be estimated by taking the inside part of the root-square. Similarly, solving for real values of the root a value of the minimum magnitude force F that starts object motion can be estimated. For instance,

$$\sqrt{b^2 F^2 - \mu(mg + F_{VdW})\big(\mu(mg + F_{VdW})b^2 - 2by_n F\big)} \geq 0$$

and solving for **F**

$$F(\mu, yn) = \frac{\mu(mg + F_{VdW})(\sqrt{y_n^2 + b^2} - y_n)}{b} \tag{4.8}$$

Equation 4.8 provides a direct dependence with the location of the applied force y_n and the coefficient of friction μ.

In addition, assuming that the applied force is acting perpendicular to the pushed/pulled nanorod during the manipulation, an extended equation can be obtained ($\sum F_{\text{perpendicular}} = 0$, *see Equation* 4.9). Then, by resolving the forces perpendicular to the nanorod in order to calculate the minimum pushing/pulling force **F** necessary to start motion, a relationship that locates the quasi-static **iCOR** in terms of the frictional force can be derived (Equation 4.10).

$$F - f1 + f2 = 0, \tag{4.9}$$

$$F(\mu, R) = \frac{\mu(mg + F_{VdW})R}{b}, \tag{4.10}$$

Expression as in Equation 4.10 can be usefull when the **iCOR** position and the pulled/pushed magnitude force are known (**i.e.** experimental information) to approximate a value for the coefficient of friction μ. The frictional forces due to moments $f1$ and $f2$ are the values previously defined in Equation 4.4 and Equation 4.5, respectively.

4.2.3.2 Location of the iCOR for unknown pressure distribution

A similar analysis is used taking Equation 4.6. In this case Equation 4.6 is solved for **F** (Equation 4.11). **F** represents the minimum pushing/pulling force necessary to start the nanorod's motion.

$$F = \frac{\mu(mg + F_{VdW})}{2b}\left[\frac{(b^2 + R^2)}{R + y_n}\right], \qquad (4.11)$$

solving for the forces perpendicular to the nanorod ($\sum F_{\text{perpendicuar}} = 0$ *see Equation* 4.12) with the value of **F** (Equation 4.11) in the bellow equation, and solving for **R**.

$$F - f1 + f2 = 0, \qquad (4.12)$$

$$R = \sqrt{b^2 + y_n^2} - y_n \qquad (4.13)$$

Equation (4.13) results in the same equation as theone obtained by Pham et al. in [77] using the *minimum force principle* at the macroscale (*see appendix* A.1). In this case, the frictional parameters are absent representing the case of unknown pressure distribution. Also, Equation 4.13 shows a direct relation between the pushing point of the force and the **iCOR** position at quasi-static motion.

4.3 Results from simulations

This section presents results on the simulations for the proposed developed models of equations to calculate the **iCOR** position at quasi-static motion. First, a comparison is made between the resulted equation for unknown pressure distribution and those found in the lit-

erature. Second, the minimum pushing force magnitude to start the nano object motion is calculated and related with its applied location to study the relationship between a moment of force and its frictional coefficient. Finally, the **iCOR** location is calculated and related to the applied pushing force magnitude to study the relationship between the **iCOR** and the nanorod frictional coefficient. Simulations were done for a nano-objects of graphite (carbon) on graphite. Simulations were running under a Linux environment (Ubuntu 12.04 LTS) on a CPU AMD Turion64x2, 4Gb in RAM and using double precision arithmetic.

4.3.1 Location of Quasi-static iCOR for unknown pressure distribution using different techniques

Figure 4.2 shows the calculated **iCOR** positions using different methodologies described in section 4.2.1 and section 4.2.2 without the use of constrains for a thin carbon nanorod of length $L = 590[nm]$. The pushing force is applied at different locations y_n (x-axis) and its corresponding **iCOR** location is then calculated (y-axis). From the graphic shown in Figure 4.2 it is noted that Equation (4.3) and Equation (4.2) produced no variation in the calculated **iCOR** position. In order to find the reason why these equations gave the same results, an analysis which consists in a coordinate transformation was done. The previous analysis concluded that the differences in shape of the previous equations is due to the localization of the reference point from which all the longitudinal parameters are defined (left side end or right side end of the rod). Thus, Equation (4.3) and Equation (4.2) are in essence the same, with just a translation in its coordinates. Furthermore, the developed Equation (4.13) using the proposed methodology described in Section 4.2.3.2 predicts the same results in comparison with the equations derived using the minimum energy principle (Equation (4.3) and Equation (4.2)).
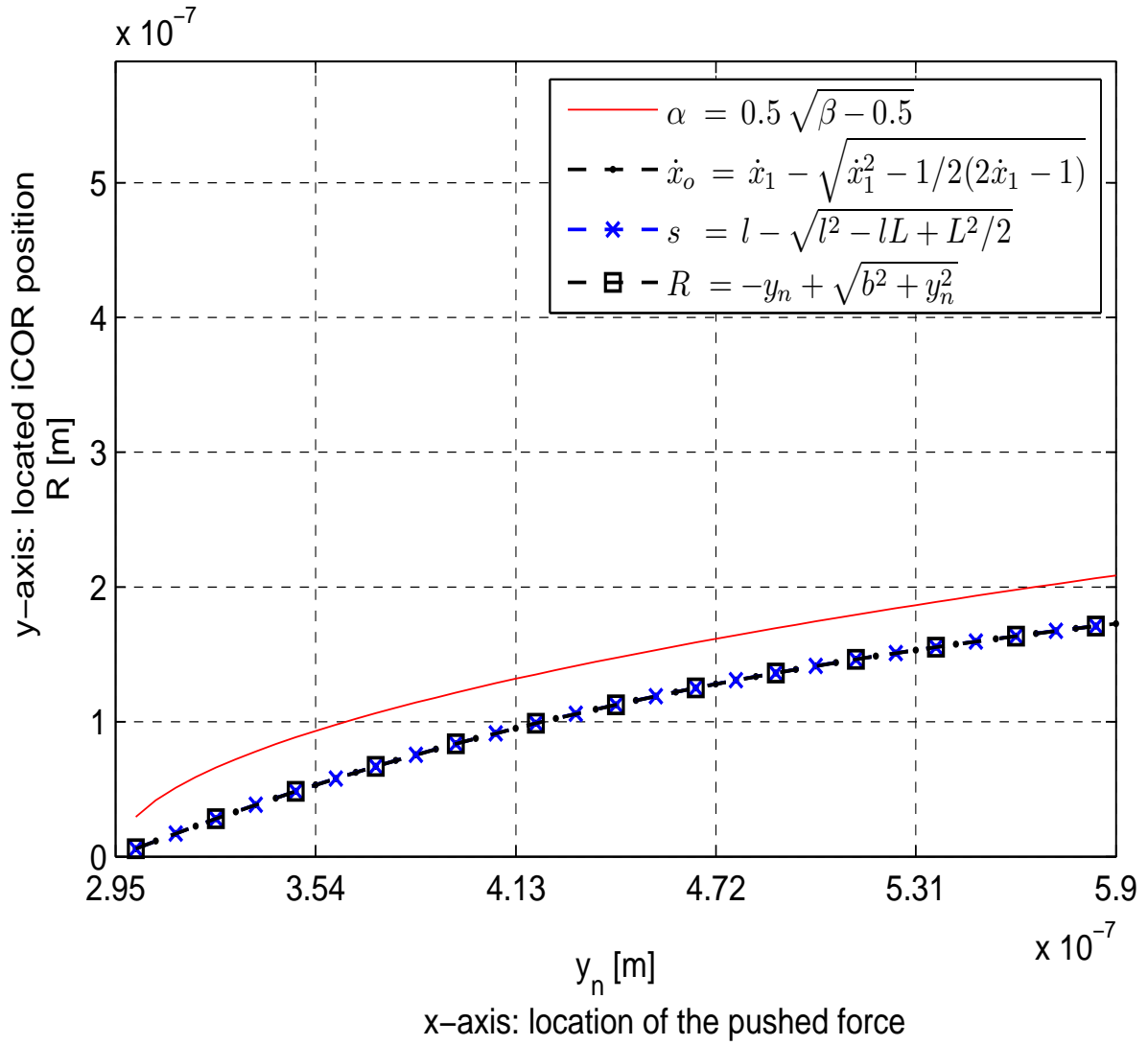
Figure 4.2: Comparison using four different equations to calculate the *Quasi-static* **iCOR** location for a thin carbon nanorod of length $L = 590[nm]$.

Moreover, for the case of the method described in section 4.2.1, the resulting curve from Equation (4.1) shows a scale factor in the values of the **iCOR** position. A possible cause of this can be attributed to some differences in the the experimental procedure such as the type of substrate used, teh **AFM** calibration process and ambient conditions during the manipulation. Also, it may be because the motion is more approximate in the dynamic case as the measured **iCOR** locations were taken after the **AFM**-probe lost contact with the nano-object.

In general, Equation (4.1), Equation (4.2) and Equation (4.3), were obtained for an assumed rigid cylinder (**MWCNT**) where the contact is only a line (there is no deformation). However, these equations are still valid and can be used to describe the motion of a nanorod.

4.3.2 Location of Quasi-static iCOR for known pressure distributions for line segment contact

When the material parameters of the nano-object being manipulated are know (**i.e.** *coefficient of friction* μ) Equation (4.7) represents an equation that models the location of the **iCOR**. Figure 4.3 shows the resulting graphs of the **iCOR** locations for different values of the coefficient of friction for a thin carbon nanorod of length $L = 590[nm]$. Coefficient of friction values were varied from 0.01 to 0.15. Pushing force values were taken such as satisfied the quasi-static motion $F \cong \mu(mg + F_{VdW})$.

It is noted from the graph in Figure 4.3 that a family of parallel curves was obtained. This results in the location of the **iCOR** being in accordance with the theory. No variation is presented in the **iCOR** location as the method solves its location for every pushing force that will keep quasi-static motion possible. Therefore, a variation in the pushed force magnitude will be more related with the frictional properties of the system.
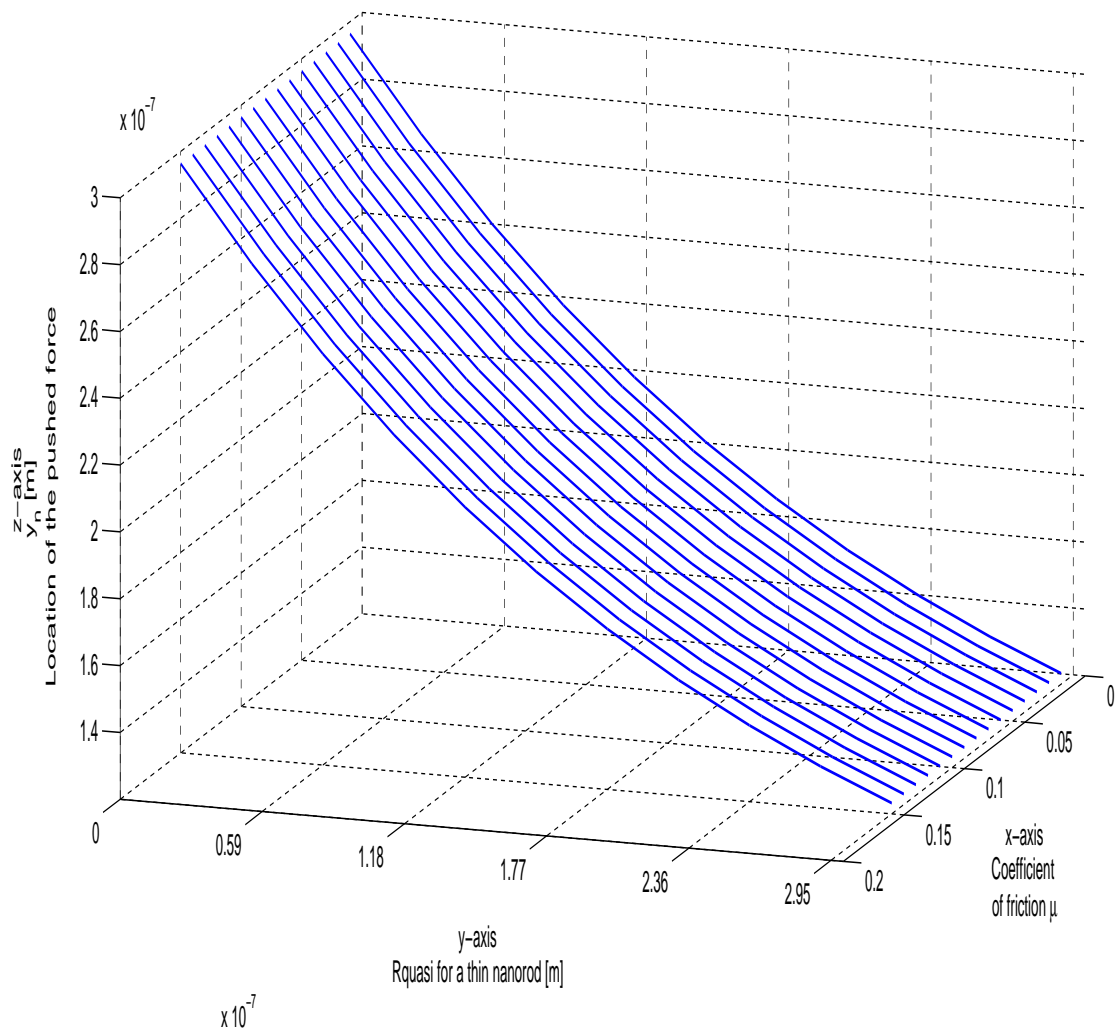
Figure 4.3: *Quasi-static* **iCOR** locations for a thin carbon nanorod of length $L = 590[nm]$ for different coefficient of friction values μ for known pressure distribution.

On the other hand, the developed Equation (4.8) can be used in conjunction with experimental parameters obtained from the manipulation process to approximate the coefficient of friction μ. Figure 4.3 shows the family of curves where the minimum magnitude of the pushed force will move the nano-object. This magnitude has a dependence with its application point (y_n) and a coefficient of friction (μ). The value of μ varies from 0.01 to 1.00.

Therefore, Figure 4.4 may be used as a graphic map to approximate an estimated value for the coefficient of friction μ of the system once the value of the magnitude of the pushed force is known. The value of the magnitude of the pushed force may be obtained from the experimental data (**i.e. AFM** *force graph*).

Figure 4.5 shows the resulting graph using Equation (4.10). Also, with reference to the graph on Figure 4.5 it is also noted that a consistent **iCOR** point location is found at $\approx$ 118 nm (x-axis). This point is the location where the pushed or pulled force is minimised, but its arm moment is maximised (**i.e.** on end of the nanorod). As a result, pushing or pulling one end of the nanorod will give the best location to approximate the value of the coefficient of friction μ from the system under manipulation.

Figure 4.4 and Figure 4.5 shows two different options to generate frictional maps which can approximate the coefficient of friction value using data measured directly from the manipulation in process and using observed values in the location of the resulted **iCOR** from experimentation, respectively. Thus, the use of each map will vary in accordance with the preferred data acquisition method. It is also noted that if both maps are generated, then an increment in the prediction of the coefficient of friction value can be achieved using the statistic mean of the two obtained frictional coefficient values.
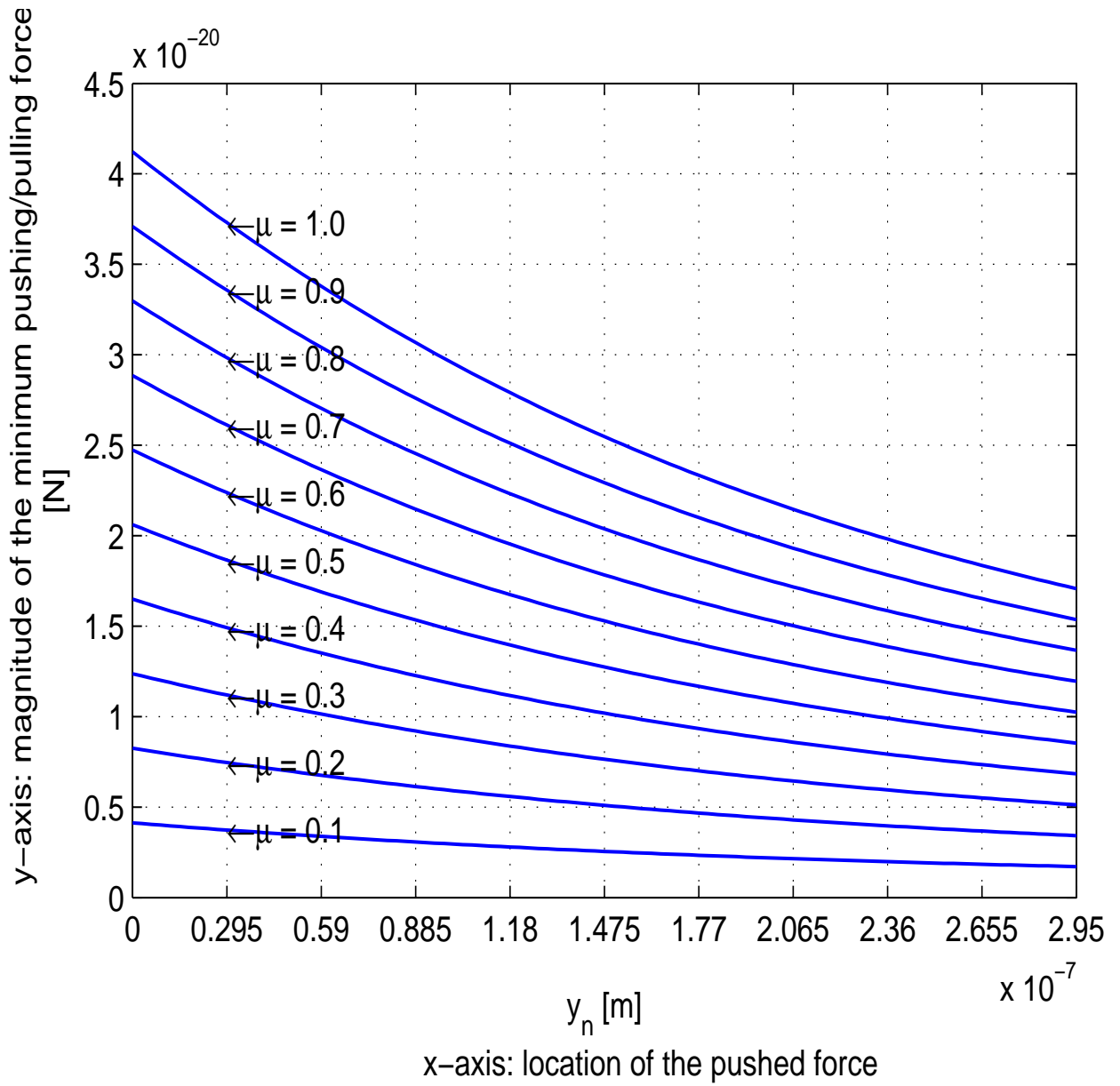
Figure 4.4: Variation of the pulled/pushed magnitude force $\mathbf{F}$ for a thin carbon nanorod of length $L = 590[nm]$ with its application location yn.
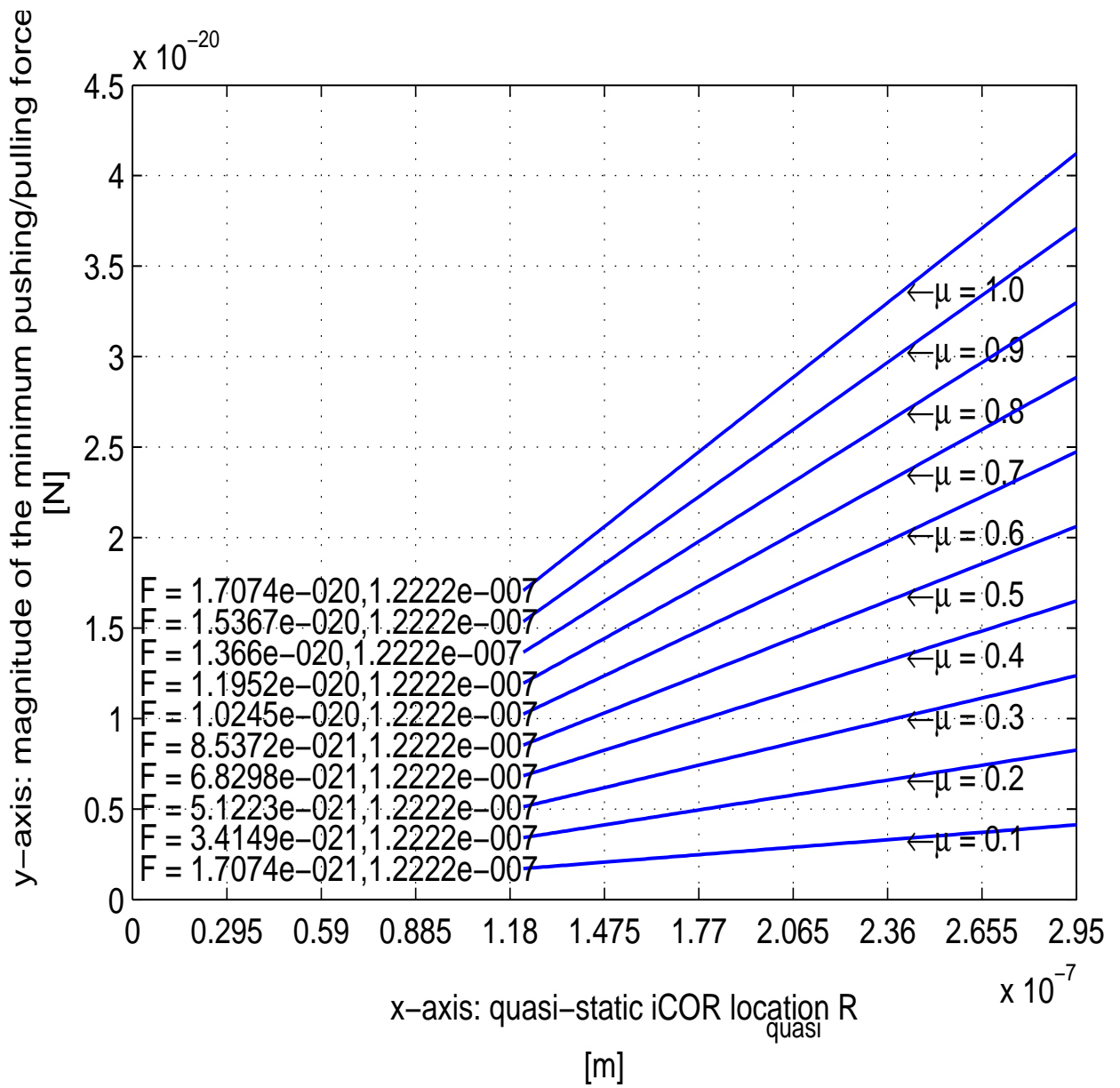
Figure 4.5: Variation of the pulled/pushed magnitude force **F** for a thin carbon nanorod of length $L = 590[nm]$ with its quasi-static **iCOR** location.

4.4 Discussion

It is worth establishing the difference between the shear stress force and frictional force, which the literature treats as equivalent. The shear force is due to the tensile or compressive stress that an object will experience through and at each element of its constituent body (particles) as two different forces acting on it at the same or opposite direction. Whereas the frictional force is a tangential force which depends on the load and a coefficient of friction μ and is independent of the area of contact between the object and the supporting surface.

4.5 Summary

This chapter introduced developed equations to describe the quasi-static motion of nano-objects being pushed/pulled by locating their **iCOR** position for unknown and known pressure distributions. Also, this chapter presents two new graphic methods to approximate the numerical value of the coeffcient of friction μ. These two graphic methods showed a relationship between the **iCOR** location and the applied moment of the force. In the same way, the correlation between values generated by the developed equations and those developed using the minimum energy principle strongly suggest that the frictional force for nanoscale objects can be modelled using the Coulomb frictional model. Also, that the frictional force is uniformly distributed in the contact.

Chapter 5

Location of the iCOR using a novel minimum force principle and the use of constraints

5.1   Introduction

This chapter presents a novel technique to calculate the **iCOR** position for in-plane rotations when the nano-object is sliding. This developed analysis is based on the use of constraints. Constraints are those which limit the nano-object's motion by adding or restricting its movements. Therefore, motion constraints are defined and included in the previously modelled equations for sliding motion. The equations are then solved using a minimum force principle. Thus, to solve for a minimal pushed/pulled force that will start the nano-object's sliding motion, a new model is generated. Results obtained using the proposed technique improved accuracy from the methodology proposed in previous chapter.

Moreover, this Chapter studies and analyses the corresponding **iCOR** location for two different types of motion. The analysed motions are Impulsive and Dynamic motion during sliding.

5.2 iCOR location combining a minimum force principle and constraints of motion

From Chapter 4, the displacement or rotation of the nano-object is controlled by the magnitude and location of the effective resultant force acting on it. When the effective resultant force acts at the centre of mass of the object, the moment produced in respect to it is zero and the object will not rotate [see pp. 83, chap. 4]. Furthermore, if the effective resultant force is perpendicular to the object's orientation and overcomes the value of the frictional force, then the object will be on pure translation. For pure translation, the **iCOR** is suggested to be located at infinity in a plane parallel to the one where the effective resultant force acts or to exist in the imaginary solution plane [see pp. 75, chap. 5].

The instantaneous centre of rotation **iCOR** is defined for different types of phases that the object will have when its motion starts. The phases of motion that an object has when it is pulled or pushed are: Quasi-static, Impulsive and Dynamic. Each of these phases are related to different conditions or constraints imposed by the system under analysis. The analysis in detail of each of these phases contributes to developing equations that in conjunction provide a complete description of the object's motion and also describe the properties of the system (**i.e.** frictional force).

When the nano-object is subject to an effective force, it can go through rotating (circular trajectory) or sliding motion (tangential trajectory). A constraint is defined in this work as 'a limitation on the space of motions over the which the instantaneous power is minimized ' [78]. For instance, in modelling rotation motion, a pure sliding motion could be considered as a constraint (a limitation on the space of motions). On the other hand, in modelling pure sliding motion, rotation motion could be considered as a constraint in the solution space. A relation between tangential and circular motion is well stated to follow the relation $a_T = r\alpha$, where a_T represents the tangential acceleration, α represents the angular acceleration and r is

the distance from the particle or nano object rotating about a fixed point [83].

5.3 Developed analysis to locate the iCOR position

This section describes the developed analysis using constraints. Essentially to solve for quasi-static motion is equivalent to solving Newton's equations of motion in equilibrium when there are no external constraints (Equation (4.7) and Equation (4.13)). When constraints need to be added, is necessary to take into account the inertial part (ma or $I\alpha$) and then minimise the value of **F** with respect to **R** (**i.e.** $\delta F/\delta R = 0$). This means to look for the minimum force which produces the minimum change in the nano-object's position for a sequence of equilibrium states. Firstly, the set of equations which describes the nano-object's motion are defined as

Force   Moments   Tangential   Forces   Constraint

$$\sum M_o = I_o \alpha \qquad\qquad \sum F_{\mathrm{T}} = m a_T \qquad\qquad \alpha = \frac{a_T}{R}$$

$$\sum M_o = I_o \left(\frac{a_T}{R}\right) \qquad\qquad a_T = \frac{\sum F_{\mathrm{T}}}{m}$$

$$I_o = I + m R^2 \qquad\qquad \sum F_{\mathrm{T}} = F - f_1 + f_2$$

where I_o is the inertia moment of the nano-object taken around the assumed **iCOR** location, α is the angular acceleration, m is the nano-object mass, a_T is the tangential acceleration, R is the distance between the **iCOR** position and the nano-object's centre of mass (C.M.), f_1 and f_2 represents the frictional forces and F is the pushing/pulling force acting on the nano-object.

Secondly, the above equations need to be manipulated in order to include the relation between translational and rotational displacements (**i.e.** $\alpha = a_T/R$). This is achieved when the tangential acceleration a_T is solved in terms of the tangential forces and the nano-object's mass $(a_T = \sum F_T/m)$. Then, the angular acceleration of the nano-object (α) is expressed in terms of tangential acceleration and the **iCOR** distance R. Finally, the inertia moment I_o is defined as expressed in $I_o = I + mR^2$ and all the previous manipulated equations are substituted in the moment equation. Thereby, Equation 5.1 remains as the principal equation to be solved in terms of R, thus

$$F(R + y_n) - f_1\left(\frac{b+R}{2}\right) - f_1\left(\frac{b+R}{2}\right) = I_o\left(\frac{\sum F_T}{mR}\right) \tag{5.1}$$

The manipulation of Equation 5.1 was done using the software package $wxMaxima11.08.0$ running under a Linux environment (Ubuntu 12.04 LTS). $wxMaxima$ is a graphical user interface for the computer algebra system. Therefore,

```
(%i1)  f1(R):= ((u*(m*g+F_{vdw}))*(b+R))/(2*b);
```

$$(\%o1) \quad \mathrm{f1}\,(R) := \frac{\mu\,(m\,g + F_{vdw})\,(b+R)}{2\,b}$$

```
(%i2)  f2(R):= ((u*(m*g+F_{vdw}))*(b-R))/(2*b);
```

$$(\%o2) \quad \mathrm{f2}\,(R) := \frac{\mu\,(m\,g + F_{vdw})\,(b-R)}{2\,b}$$

```
(%i3)  Io(R):= I+m*R^2;
```

$$(\%o3) \quad \mathrm{Io}\,(R) := I + m\,R^2$$

(%i4)   C1: F*(R+yn)-f1(R)*((b+R)/2)-f2(R)*((b-R)/2)

             = Io(R)*((F-f1(R)+f2(R))/(m*R));

$$-\frac{(g\,m+F_{vdw})\,\mu\,(R+b)^2}{4\,b}+F\,(R+yn)-\frac{(g\,m+F_{vdw})\,\mu\,(b-R)^2}{4\,b}$$

$$=\frac{\left(-\frac{(g\,m+F_{vdw})\,\mu\,(R+b)}{2\,b}+\frac{(g\,m+F_{vdw})\,\mu\,(b-R)}{2\,b}+F\right)\,(m\,R^2+I)}{m\,R}$$

(%i5) factor(C1);

(%o5)

$$-\frac{g\,m\,\mu\,R^2+F_{vdw}\,\mu\,R^2-2\,b\,F\,R-2\,b\,yn\,F+b^2\,g\,m\,\mu+b^2\,F_{vdw}\,\mu}{2\,b}$$

$$=-\frac{(g\,m\,\mu\,R+F_{vdw}\,\mu\,R-b\,F)\,(m\,R^2+I)}{b\,m\,R}$$

(%i6) solve(C1,F);

As a result, the simplified equation of motion solved for the pushing/pulling force **F** using comand 'solve(C1,F)' obtained is

$$F = \frac{-1}{(2\,b\,m\,y_n\,R-2\,b\,I)}\left[(g\,m^2+F_{vdw}\,m)\,\mu\,R^3+\left((2\,g\,m+2\,F_{vdw})\,\mu\,I\right.\right.$$

$$\left.\left.+(-b^2\,g\,m^2-b^2\,F_{vdw}\,m)\,\mu\right)\,R\right] \tag{5.2}$$

and minimising the force **F** in Equation (5.2) with respect to **R** in the quasi-static approxima-
tion which is equivalent to $\delta F/\delta R = 0$, therefore

(%i7) diff(%o6,R);

(%o8)

$$
= \frac{2\,b\,m\,y_n\left((g\,m^2 + F_{vdw}\,m)\,\mu\,R^3 + \left((2\,g\,m + 2\,F_{vdw})\,\mu\,I + (-b^2\,g\,m^2 - b^2\,F_{vdw}\,m)\,\mu\right)R\right)}{(2\,b\,m\,y_n\,R - 2\,b\,I)^2}
$$

$$
- \frac{3\,(g\,m^2 + F_{vdw}\,m)\,\mu\,R^2 + (2\,g\,m + 2\,F_{vdw})\,\mu\,I + (-b^2\,g\,m^2 - b^2\,F_{vdw}\,m)\,\mu}{2\,b\,m\,y_n\,R - 2\,b\,I}
$$

(%i9) ratsimp(%o8);

$$
\delta F/\delta R \;=\; \frac{-1}{(2\,b\,m^2\,y_n^2\,R^2 - 4\,b\,m\,y_n\,I\,R + 2\,b\,I^2)}\Bigg[(2gm^3 + 2F_{vdw}m^2)\mu\,y_n R^3
$$

$$
+ (-3\,g\,m^2 - 3\,F_{vdw}\,m)\,\mu\,I\,R^2 + (-2\,g\,m - 2\,F_{vdw})\,\mu\,I^2
$$

$$
+ (b^2\,g\,m^2 + b^2\,F_{vdw}\,m)\,\mu\,I\Bigg] \tag{5.3}
$$

in the quasi-static approximation $\delta F/\delta R = 0$, consequently solving Equation (5.3) under the
quasi-static conditions will yield the value of **R** that minimises **F**

144

$$(2\,g\,m^3 + 2\,F_{vdw}\,m^2)\,\mu\,y_n\,R^3 + (-3\,g\,m^2 - 3\,F_{vdw}\,m)\,\mu\,I\,R^2$$

$$+\,(-2\,g\,m - 2\,F_{vdw})\,\mu\,I^2 + (b^2\,g\,m^2 + b^2\,F_{vdw}\,m)\,\mu\,I = 0$$

and simplifying,

$$(2\,g\,m^3 + 2\,F_{vdw}\,m^2)\,y_n\,R^3 + (-3\,g\,m^2 - 3\,F_{vdw}\,m)\,I\,R^2$$

$$+\,(-2\,g\,m - 2\,F_{vdw})\,I^2 + (b^2\,g\,m^2 + b^2\,F_{vdw}\,m)\,I = 0 \tag{5.4}$$

where I is the inertia moment of the nano-object and m, g, F_{vdw}, b, y_n are the parameters previously defined. Equation (5.4) is one dimensional (one independent variable) and it can be solved using root finding methods (**i.e.** *Eigenvalues method, Van Wijngaarden-Deker-Brent method*).

5.3.1 Van Wijngaarden-Deker-Brent and Eigenvalues root finding methods

In contrast to the root finding Eigenvalues method, the Van Wijngaarden-Deker-Brent method provides high accuracy in its solution because it searches in a given solution space. This reduces the computing time required to find the solution and increases its accuracy. Thus, the solution is restricted to a specific range in a solution space. This method combines root bracketing, bisection, and inverse quadratic interpolation to converge from the neighbourhood of

a zero crossing. By contrast, the eigenvalues method involves computing the eigenvalues of the companion matrix defined by the polynomial [73]. Thus, the eigenvalues method requires more computing time because it searches over a whole range of possible solutions.

5.3.2   Results from simulations

As the **iCOR** could be located at some point inside the area of contact or outside of it (**i.e. iCOR** located at infinity). Therefore, to be assured that all possible solutions are included (roots space), Equation (5.4) is solved by the two root finding methods mentioned in previous section. The eigenvalues method is used to map for all possible solutions (**i.e. iCOR** locations outside the contact area or **iCOR** locations at infinity).

Calculated **iCOR** locations for a thin carbon nano-rod of length $L = 590[nm]$ using the developed Equation (5.4) are presented on Table 5.1. From Table 5.1, the eigenvalues method produces the same results as those obtained by Van Wijngaarden-Deker-Brent method. Thus, Equation (5.4) is able to map all possible solutions of the location of the **iCOR**.

Finally, near the end of the Table 5.1, values bifurcation points start to appear when the force is near to the nano-object's **C.M.**. The bifurcation points represent a symmetric location of values by having its positive and negative values.

146

Table 5.1: iCOR location using two different methodologies to find the roots of the Equation (5.4)

yn meters	Van Wijngaarden-Deker-Brent meters	Eigenvalues method meters
2.95e-007	7.93e-008	7.93e-008
2.85e-007	7.97e-008	7.97e-008
2.75e-007	8.012e-008	8.012e-008
2.65e-007	8.054e-008	8.054e-008
2.55e-007	8.098e-008	8.098e-008
2.45e-007	8.142e-008	8.142e-008
2.35e-007	8.188e-008	8.188e-008
2.25e-007	8.235e-008	8.235e-008
2.15e-007	8.283e-008	8.283e-008
2.05e-007	8.333e-008	8.333e-008
1.95e-007	8.384e-008	8.384e-008
1.85e-007	8.436e-008	8.436e-008
1.75e-007	8.49e-008	8.49e-008
1.65e-007	8.546e-008	8.546e-008
1.55e-007	8.603e-008	8.603e-008
1.45e-007	8.662e-008	8.662e-008
1.35e-007	8.723e-008	8.723e-008
1.25e-007	8.787e-008	8.787e-008
1.15e-007	8.852e-008	8.852e-008
1.05e-007	8.92e-008	8.92e-008
9.5e-008	8.99e-008	8.99e-008
8.5e-008	9.064e-008	9.064e-008
7.5e-008	9.14e-008	9.14e-008
6.5e-008	9.219e-008	9.219e-008
5.5e-008	9.302e-008	9.302e-008
4.5e-008	9.388e-008	9.388e-008
3.5e-008	9.479e-008	9.479e-008
2.5e-008	9.574e-008	9.574e-008
1.5e-008	9.673e-008	9.673e-008
5e-009	9.779e-008	9.779e-008
4e-009	9.789e-008	9.789e-008
3e-009	9.800e-008	9.800e-008
2e-009	$\pm$9.811e-008	$\pm$9.811e-008
1e-009	$\pm$9.822e-008	$\pm$9.822e-008
0.0e000	$\pm$9.833e-008	$\pm$9.833e-008

5.4 iCOR location for quasi-impulsive motion

Impulsive motion describes mechanical systems where the motion of the object is caused by an impulse force. An impulse force is a force whose value is extremely high in a very short period of time. As a result, an impulse force has a tendency to increase without limit in a limit period of time, overcoming finite forces (**i.e.** *frictional force*). This fundamental characteristic results in an analysis describing the momentum of the object during the period of time where the impulse exists. Therefore, the Newton's laws equations of motion must be presented in terms of impulse-momentum equations.

The linear momentum is defined as $P = mV_{C.M.}$, where m is the mass of the object, $V_{C.M.}$ is the linear speed of its mass object centre, and the angular momentum by $H_{C.M.} = I_{C.M.}\omega$, where $H_{C.M.}$ represents the moment of momentum caused by the impulsive force, $I_{C.M.}$ is the inertia moment and ω is the angular speed of the rotating object. It is important to emphasis that previous equations should defined with reference to the instantaneous axis of rotation by using the parallel axis theorem [83, 84].

Parameters are defined in Figure 5.1, where **F** is the impulse force applied at the point **Q**, y_n is the distance between the applied impulse force and the nano-rod centre of mass(**C.M.**), **2b** is the length of the nano-rod, $R_{Impulsive}$ is the distance between the Impulsive **iCOR** location and the nano-rod centre of mass **C.M.** Also, the impulsive equation of motion is solved in terms of the radius of gyration $k_{C.M.}$ ($k_{C.M.} = I_{C.M.}/m$). Thus, by solving for $R_{Impulsive}$, the simplified equation results in Equation (5.5),

$$R_{Impulsive} + y_n = \frac{(K_{C.M.}^2 + R_{Impulsive}^2)}{R_{Impulsive}},$$

$$R_{Impulsive} = \frac{K_{C.M.}^2}{y_n} \tag{5.5}$$
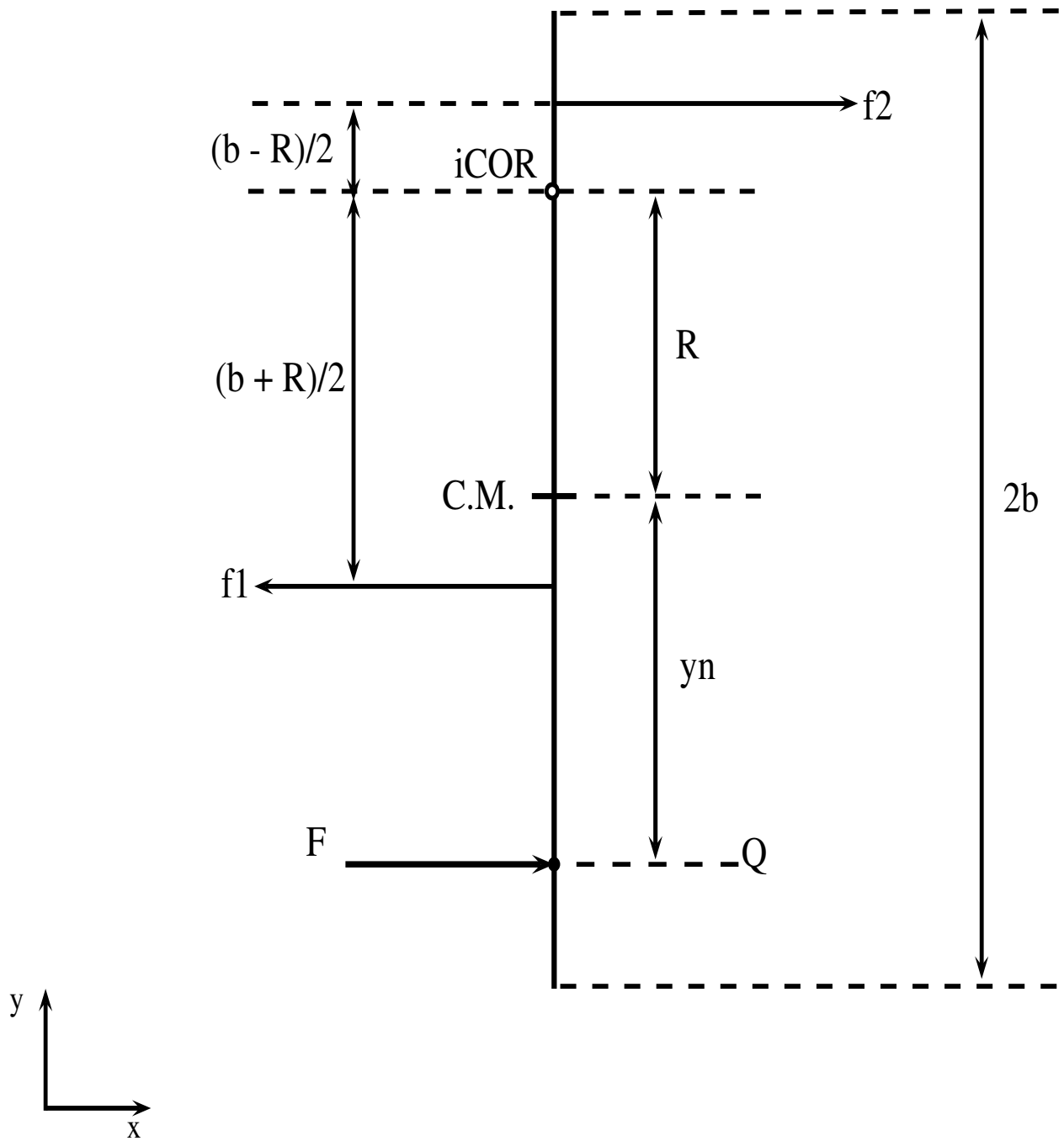
Figure 5.1: Analysis of forces and parameters description for impulsive analysis (*Impulsive* **iCOR**).

5.5 iCOR location for quasi-dynamic motion

Dynamic motion describes a mechanical system that obeys Newton's second laws of motion ($\sum F = m\ddot{x}$ and $\sum M = I_{C.M.}\ddot{\theta}$), where F is the effective force applied, $\ddot{x}$ is the linear acceleration, m the mass of the nano-object, M is the moment of the force produced by the effective force F, $I_{C.M.}$ the moment of inertia and $\ddot{\theta}$ the in-plane angular acceleration of the nano-object. Also, for the analysis of forces, a similar value for static and kinetic coefficient of friction is assumed.

In dealing with the nano-scale case, the nano-object is uniformly accelerated by an effective force subject to the gravitational and Van der Waals forces. The effective force overcomes the static forces (**i.e.** static friction force). Therefore, the motion is characterised by the dynamic friction force and the effective force magnitude which can overcome friction and adhesional forces to keep motion in the pushed/pulled nano-object.

To describe the quasi-dynamic behaviour of the nano-object, the obtained group of algebraic dynamic second order differential equations developed in Chapter 3, that describes a nano-object's motion, was integrated over a short period of time ($t = 10^{-10}$ seconds). The program was coded in FORTRAN using the Bulirsch-Stooer integration routine which is then used to solve for the quasi-dynamic motion case at very small integration steps of $t = 10^{-10}$ seconds.

5.6 Results from simulations

This section presents firstly the results of the simulations for the proposed developed models of equations to calculate the **iCOR** position. Secondly, a comparison between the use of constraints and when they are absent in the quasi-static **iCOR** analysis is explored. Finally, a variation of the quasi-static **iCOR** and the impulsive **iCOR** is analysed. Simulations were done for nano-objects of graphite (carbon) on graphite of different sizes. These simulations were run under a Linux environment (Ubuntu 12.04 LTS) on a CPU AMD Turion64x2, 4Gb

in RAM and using double precision arithmetic.

5.6.1 Location of Quasi-static iCOR free of constraints vs location of Quasi-static iCOR with constraints for line segment contact

The analyses developed in Section 5.2 and in Section 4.2.3.2 were used to generate Figure 5.2. Figure 5.2 shows two graphs. A continuous line is used to describe the **iCOR** locations using Equation (5.4), whereas a dashed line describes the **iCOR** locations using Equation (4.13). Negative values in the $y - axis$ are presented to describe **iCOR** positions that are under the nano-rod's centre of gravity ($y - axis$ origin).

The plotted graph using constraints in the nano-object's motion (continuous line in Figure 5.2) presents a bifurcation point when the pushing force acts at the nanorod's centre of mass. The bifurcation points are represented with two squares in the graph. Bifurcation points were being observed in nanomachines with translation in its motion [85, 86]. Also, another interpretation of this particular solution is that the nanorod will be rotating in opposite directions at the same time. Previous interpretation is also related, as a couple of forces acting on the nanorod, which makes it be in a equilibrium state. This equilibrium state is highly dependent of the magnitude and direction of the force acting at the nanorod's centre of gravity as reported in experiments by Li et al. [6]. Li et al. concluded that attempting to manipulate the nano-object through its centre of gravity provides high uncertainly in the resulting in-plane rotation direction of the nano-object under manipulation.

Pulling or pushing through the nanorod's centre of gravity with a force perpendicular to the nanorod will produce translation (pure sliding). It is also noted that pushing near to the object's centre of gravity (a short moment arm) provides no greater rotation to the nano-object (**iCOR** location states closely). This is quite the opposite to the case when the motion constraints are omitted (dashed line). Including the tangential motion constraint into the motion's

analysis will reduce the angular speed magnitude of the rotating nano-object, as tangential displacement generates some resistance, slowing down the nanorod's angular motion. Then, the accuracy in the quasi-static analysis is compared with object's speed. For low speeds, quasi-static analysis is more accurate, whereas for high speed it is less accurate. Therefore, pushing near to the nano-object's centre of gravity, the nanorod's angular speed decreases as the force moment reduces its magnitude. Thus, values of the **iCOR** locations are less than those calculated without the use of constrains.

5.6.1.1   Anlysis of error

This section describes the calculated margin of error using a 95% level of confidence in the **iCOR** locations for both methods. This level of confidence is roughly between -2 and $+2$ times the standard error. Using the data generated by Equation (4.13), where the constraints are not taken into account, a standard deviation of the normalised computed data is: 49.6987 and the number of locations (samples). The number of samples corresponds to the number of different locations at which the force is applied to the nanorod (number of samples $n = 296$).

On the other hand, the standard deviation of the computed **iCOR** locations using the equation with constraints is: 5.3950 for the same number of samples (**i.e.** $n = 296$). The substantial increment in the accuracy using the proposed methodology when constraints are included is more significant when the nano objects are pushed/pulled by locations near to its centre of mass. Thi is quite opposite to the case when constraints are omitted and perhaps this could be the reason why its standard deviation value is high.
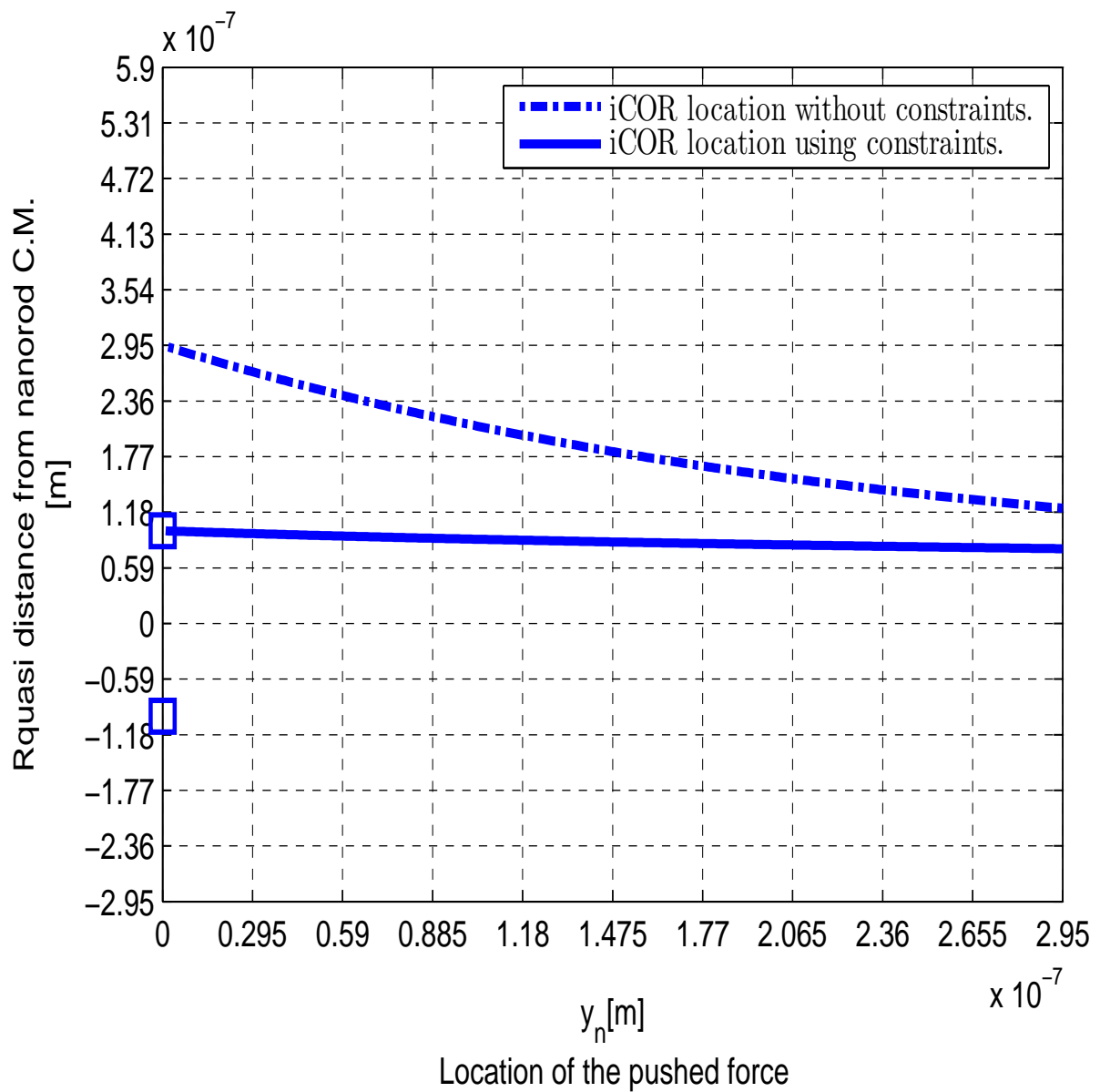
Figure 5.2: *Quasi-static* **iCOR** locations for a thin carbon nanorod of length $L = 590[nm]$ using constraints Equation (5.4) and without constraints Equation (4.13).

5.6.2 Variation of *quasi-static*, *dynamic* and *impulsive* iCOR with the point of application of force

The variation in the **iCOR** location for the three different motion stages (*quasi-static, impulsive and dynamic motion*) is presented in Figure 5.3.

Quasi-static motion shows its particular bifurcation points to express translation of the nanorod (the two squares at the $y - axis$). These results strongly favour the presence of pure translation of the nanorod, and as it is the same zone of pushing location for the dynamic and impulsive motion (y_n values near to zero), the values of the **iCOR** have a tendency to be at infinity. This is a condition observed and described to express translations of rigid bodies in a manipulation task of objects at the macroscale.

Pushing at the nanorod's end (nanorod's extreme), impulsive and dynamic **iCOR** locations are quite similar. This could result because pushing or pulling at the end of the nanorod produces a big moment of the force which mean similar conditions for both methods. Moreover, a pushing point where the **iCOR** location for these two different motions are consistent is found. After this consistent point (at approximately $yn \approx 1.77 \times 10^{-7}$) a separation of each stages is better appreciated. Thus, **iCOR** values for dynamic motion are less in magnitude than those corresponding to impulsive motion. In addition, from the impulsive and dynamic graphics is noted that the tendency of the nanorod to rotate is high, in contrast to the quasi-static case. Therefore, a relation between magnitude force, its position and the **iCOR** can be found which can produce fine and large nano-object displacements. Dynamic simulation was done with a coefficient of friction $\mu = 0.1$ for a thin carbon nanorod of 590 nm and radius of 13.5 nm, and using the parameters and technique described at Section 5.5.
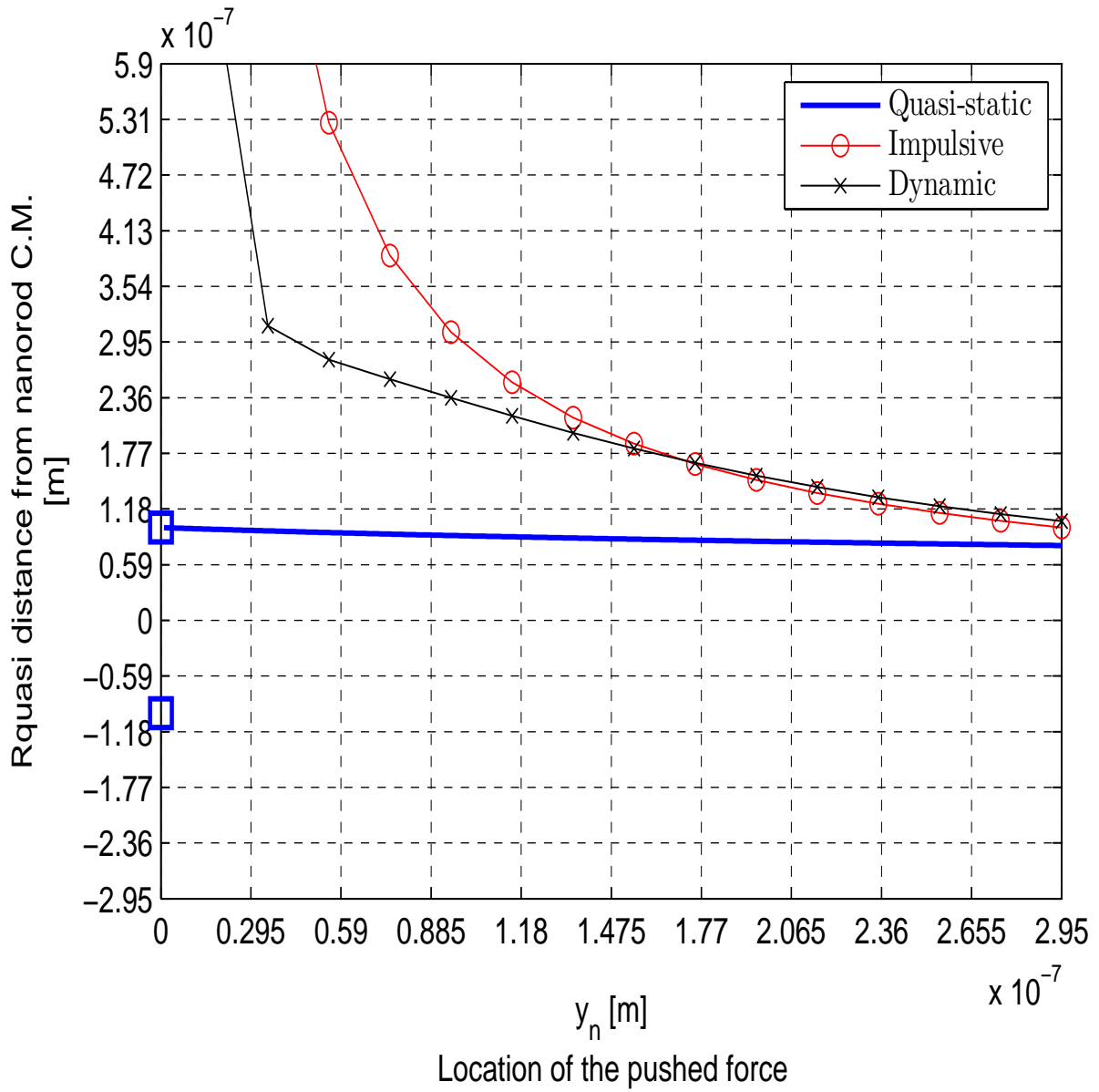
Figure 5.3: Comparative in the **iCOR** locations for a thin carbon nanorod of length $L = 590[nm]$ for different stages of motions: Quasi-Static, Dynamic and Impulsive.

5.7 Summary

Based on previous results, this chapter introduced a new equation to describe the quasi-static motion of nano-objects being pushed/pulled using constraints. Defined motion constraints and a minimal force principle were used to develop a novel methodology compared with those found in the latest literature. This methodology was used to generate a new mathematical analysis and to characterise the motion of nanoscale objects for the quasi-static motion. The results from simulations showed an accurate and improved method to locate the **iCOR** position. Moreover, simulations and analysis of nano-object's being pushed for different stages of motion suach as quasi-static, impulsive and dynamic motion were presented and analysed in detail.

Chapter 6

Conclusions

In this chapter, the contributions and conclusions of this thesis are listed and suggestions for future work provided.

6.1   Contributions

The main contributions of this thesis are:

1. Defining new parameters for surface energy for different materials. Trustful parameters in properties of materials are a critical factor to approaching and understanding their behaviour. In particular, a corrected factor value in an equation that can be found in the literature and defines the surface energy was introduced. Using this corrected parameter, new values on some materials can be obtained.

2. Mapping the coefficient of friction μ for nanoscale objects with different geometries. Scanning probe microscopes **SPM** are able to measure the total forces acting at the atomic level. For this reason, it is worthwhile providing suitable techniques than can be used to extract the major parameters to characterise the sample under analysis. This research provides, by means of developed equations that use the force and the **iCOR** of the manipulated object, a suitable tool to approximate the coeffcient of friction.

3. Location of the **iCOR** for unknown pressure distribution equation. Unknown pressure distribution means the motion is described approximately without the knowledge of tribological parameters. Therefore, using a proposed methodology, an equation that

models the **iCOR** position for quasi-static motion of nano-scale objects was presented. This equation results in the same one when used for macroscale objects. A relation to approximate the **iCOR** location betwween macroscale models and nanoscale without fitting parameters was found.

4. Location of the **iCOR** using a minimum force principle and constraints. A novel equation that improves the accuracy of the previous equation to locate the **iCOR** position for objects was developed. This proposed equation improves accuracy when calculating the **iCOR** location in quasi-static motion by expressing the motion of the nano-object as a combination of in-plane translation and in-plane rotation displacements.

5. Analysis of motion for different stages of motion. This analysis evaluates the location of the **iCOR** for Quasi-static, Quasi-dynamic and Impulsive motion. This study and analysis of the different stages of motion that nanoscale objects will experience can help to understand and estimate the best method for manipulating them. Furtherore, a consistent pushing point for Impulsive and Dynamic motion was found. This point open the posiblility of providing a consistent motion with less force and ca analyse deformations that could appear on the material/nano-object surfaces (wear) when the nano-object is manipulated under such magnitude forces.

6. Analysis of the Coulomb frictional model over a contact area. Before this research was conducted, there were no models in the literature that provide a detailed analysis of friction over a contact area for a nano-object resting on a surface using continuum mechanics. Frictional force and frictional moment were in most cases characterised by experimentation. This model relies on a macroscale model and is extended when forces at the nanoscale are introduced. Moreover, the analysis is implemented in a different nano-structure such as a nanobar whose geometry provides stable conditions for sliding motion and also applies for cylinder geometry such as **CNT** that takes into account a deformation area betweem the contact with the surface.

6.2 Conclusions

The key conclusions for each topic analysed are:

- The location of the applied force and its magnitude has a direct relation with the **iCOR** location. Furthermore, the **iCOR** location could be used to describe and determine the real motion of the nano-object, coping with the problem of blind real time manipulation monitoring at the nanoscale. Therefore, it opens the posiblility of providing a reliable manipulation of nano-objects. A reliable manipulation at the nanoscale is desirable when assambling objects into more complex structures and at the same time studying the properties and behaviour of different materials and objects at the nanoscale.

- It was shown and demonstrated that pure translation can be represented by a bifurcation point. Nevertheless, this point introduces uncertainties in the manipulated object's direction. This uncertainly in the manipulated object's direction is highly dependant on the manipulated system conditions, as for any change in the force direction the body will rotate according to the applied force angle, applied force location and applied force magnitude. In addition, this uncertainly in the object's motion can be attribuited to any topographical feature on the surface in both particle and substrate, wear during the manipulation processes and external ambient conditions Also, these uncertainties can interfere with the true frictional force being measured by the system.

- *Quasi-static* motion can be modelled not only by solving the Newton's equations of motion in equilibrium. In addition, it can be solved using the dynamic system by minimising the force, which is the equivalent to having small accelerations, as the force F is defined according to $F = ma$. On the other hand, introducing the mass of the object into the equations of motion produced an accurate picture of the forces acting on the objects, as the particle momentum of interia depends on the particle mass.

- The equations which use *the minimum power* principle to locate the **iCOR** position shown good agreement with the reported manipulation experiments at the nanoscale.

This opens the idea that Coulomb's friction model is still valid at the nanoscale. Moreover, the *minimum power principle* is only valid for models that obey Coulomb's model of friction $F_{friction} = \mu \times (Normal\,load)^n$, as the relation is linear (**i.e.** n=1). In dealing with the frictional force magnitude, rolling frictional force value is higher than sliding frictional force. This value in its magnitude is related with the arm length of the induced moment and with the surface value of the materials in contact (adehsion). Therefore, sliding is a desirable motion in terms of the manipulation of the nano-object over the surface using a minimum force value.

- The data generated from the frictional force analysis showed that the sliding motion in the nano-objet is a motion composed of in-plane translation and in-plane rotation displacements. Also, these results could imply that the stick-slide motion observed in objects at the nanoscale corresponds to in-plane rotations and in-plane translations.

6.3   Suggestions for future research

Future area of research can be orientated in two areas: *control systems* and *path planning algorithms*. In the *area of control*, results and analysis generated in this research can be implemented to derive new feedback control strategies. To control the motions of the nano-objects by pushing or pulling operations, control systems should be fast, accurate and precise in order to deliver and sense the correct amount of force being applied. Such capabilities still needs more attention. Also, better SPM calibration processes that can ensure to increase sense/feedback force could also be included in this tentative area of research.

Path planning is an area of research that can be assisted using the developed analysis and equations to automate the manipulation at the nanoscale. Algorithms which can generate paths to position and orientate nanoscale objects whilst minimising the necessary force and also the requested time are essential and not yet fully introduced in nanoscale manipulation schemes.

On the other hand, although the models and simulation presented in this research are in good agreement with the expected dynamics that can be found when pushing/pulling nano-objects, more models using the proposed methodology might be developped. Extensions to this work can be done by introducing other interactive forces at the nanoscale, using different contact models (**i.e.** DMT or Bradley models), attraction potentials (**i.e.** Leonard-Jones potential) and different conditions (**i.e.** temperature, relative humidity).

Appendices

Appendix A

A.1 iCOR location.

Using the methodology developed by Pham et al. [77] and Equations (A.1) and (A.2) to model the quasi-static motion of the nanorod.

$$F_f = \mu(mg + F_{VdW})$$ (A.1)

where, *m* is the mass of the rod, *g* represents the constant of gravity of Earth and F_{VdW} the adhesive force due to the Van der Waals forces. The Van der Waals forces interaction for a rod and a plane [82] is defined as

$$F_f = L\left(\frac{Hd^{\frac{1}{2}}}{16z_o^{\frac{5}{2}}}\right)$$ (A.2)

Taking moments about **iCOR**, for motion to be possible:

$$F \times (R + yn) - Mc > 0$$ (A.3)

In the quasi-static case, $F \times (R + yn) - Mc = 0$, thus solving for F as:

$$F = \frac{Mc}{(R + yn)} \tag{A.4}$$

defined M_c as the frictional moment. Then M_c is defined as

$$M_c = f_1 \times \frac{(b + R)}{2} + f_2 \times \frac{(R - b)}{2} \tag{A.5}$$

where f_1 and f_2 are assumed to be uniform and to be the frictional force acting on the rod. Substitute Equation (A.2) in Equation (A.1), then frictional forces are:

$$f_1 = \mu \left[mg + L\left(\frac{Hd^{\frac{1}{2}}}{16z_o^{\frac{5}{2}}} \right) \right] \times \left[\frac{(b+R)}{(2b)} \right] \tag{A.6}$$

$$f_2 = \mu \left[mg + L\left(\frac{Hd^{\frac{1}{2}}}{16z_o^{\frac{5}{2}}} \right) \right] \times \left[\frac{(b-R)}{(2b)} \right] \tag{A.7}$$

Subsititute Equation (A.6) and Equation (A.7) in Equation (A.5) results

$$Mc = \mu \left[mg + L\left(\frac{Hd^{\frac{1}{2}}}{16z_o^{\frac{5}{2}}} \right) \right] \times \left[\frac{(b+R)}{(2b)} \right] \times \left[\frac{(b+R)}{2} \right]$$

$$+ \mu \left[mg + L\left(\frac{Hd^{\frac{1}{2}}}{16z_o^{\frac{5}{2}}} \right) \right] \times \left[\frac{(b-R)}{(2b)} \right] \times \left[\frac{(b-R)}{2} \right]$$

Simplify above equation results in

$$M_c = \mu \left[mg + L\left(\frac{Hd^{\frac{1}{2}}}{16z_o^{\frac{5}{2}}} \right) \right] \times \left[\frac{(b^2 + R^2)}{(2b)} \right] \tag{A.8}$$

Subsititute Equation (A.8) into Equation (A.4) results in:

$$F = \frac{\mu \left[mg + L\left(\frac{Hd^{\frac{1}{2}}}{16z_o^{\frac{5}{2}}} \right) \right] \times \left[\frac{(b^2+R^2)}{(2b)} \right]}{(R + yn)} \tag{A.9}$$

Factorising the above equation before derivating it results in the following equation

$$\frac{dF}{dR} = \frac{\mu}{2b} \left[mg + L\left(\frac{Hd^{\frac{1}{2}}}{16z_o^{\frac{5}{2}}} \right) \right] \times \frac{d}{dR} \left[\frac{b^2 + R^2}{R + yn} \right]$$

Then finding the derivate as

$$\frac{dF}{dR} = \frac{\mu}{2b} \left[mg + L\left(\frac{Hd^{\frac{1}{2}}}{16z_o^{\frac{5}{2}}} \right) \right] \times \left[\frac{2R(R + yn) - (b^2 + R^2)}{(R + yn)^2} \right]$$

Thus for quasi-static motion $\frac{\delta F}{\delta R} = 0$ and solving for R results in the equation below.

$$0 = \frac{\mu}{2b} \left[mg + L\left(\frac{Hd^{\frac{1}{2}}}{16z_o^{\frac{5}{2}}} \right) \right] \times \left[\frac{2R(R + yn) - (b^2 + R^2)}{(R + yn)^2} \right]$$

165

$$2R(R + yn) - (b^2 + R^2) \ = 0$$

$$2R^2 + 2Ryn - b^2 - R^2 \ = 0$$

$$R^2 + 2Ryn - b^2 \ = 0$$

The final solution to this equation is then:

$$R = \sqrt{b^2 + yn^2} - yn \tag{A.10}$$

Equation (A.10) results in the same equation as the one derivated in section 4.2.3.2. Although the adesive forces due to the Van der forces were included in the model, they have not influence on the location of the **iCOR** for quasi-static motion of the rod.

Appendix B

Appdx B
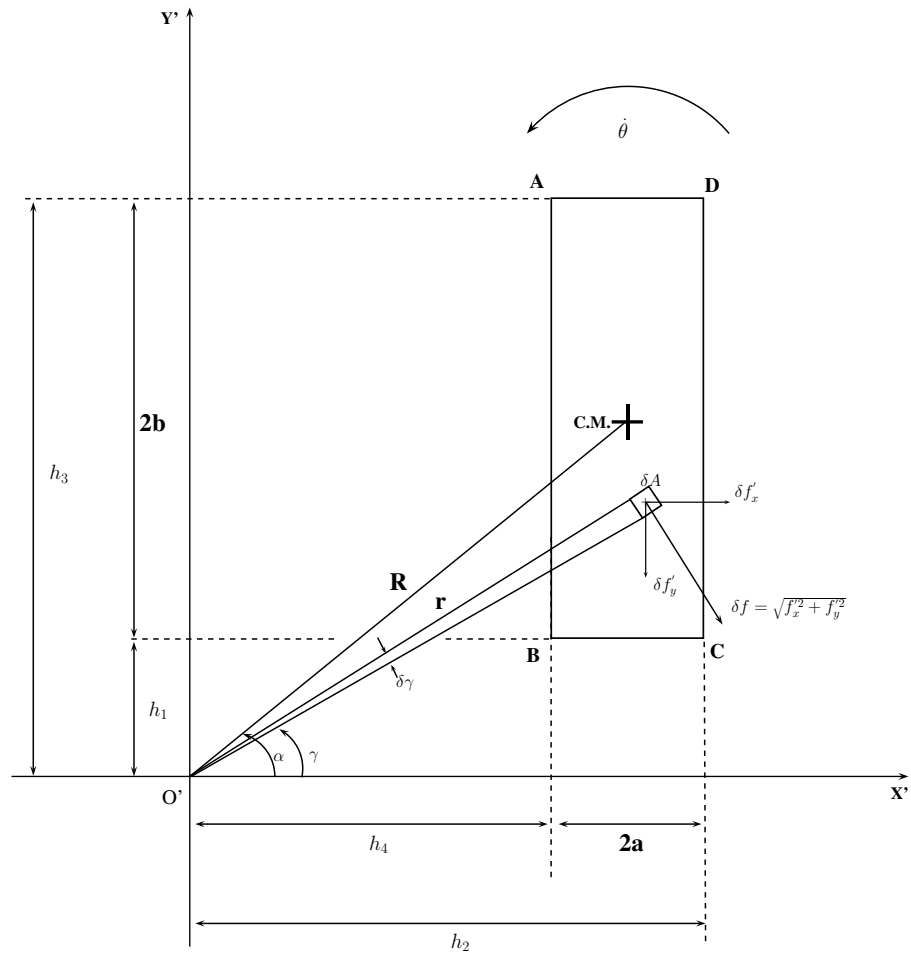
Figure B.1: Geometrical parameters definitions reference to the mobile frame **X'O'Y'**.

B.1 $f'_x = \iint_S \sin(\gamma) r dr d\gamma$

In particular to the Figure B.1, the limits of the integrals over the region S are:

$$\beta_1 \le \gamma \le \beta_2 \qquad for \qquad h_1/\sin(\gamma) \le r \le h_2/\cos(\gamma) \qquad (B.1)$$

$$\beta_2 \le \gamma \le \beta_3 \qquad for \qquad h_4/\cos(\gamma) \le r \le h_2/\cos(\gamma) \qquad (B.2)$$

$$\beta_3 \le \gamma \le \beta_4 \qquad for \qquad h_4/\cos(\gamma) \le r \le h_3/\sin(\gamma) \qquad (B.3)$$

Therefore, the limits of the integral over the region S are:

$$\iint_S \sin(\gamma) r dr d\gamma = \int_{\beta_1}^{\beta_2} \int_{h_1/\sin(\gamma)}^{h_2/\cos(\gamma)} \sin(\gamma) r dr d\gamma + \int_{\beta_2}^{\beta_3} \int_{h_4/\cos(\gamma)}^{h_2/\cos(\gamma)} \sin(\gamma) r dr d\gamma$$

$$+ \int_{\beta_3}^{\beta_4} \int_{h_4/\cos(\gamma)}^{h_3/\sin(\gamma)} \sin(\gamma) r dr d\gamma \qquad (B.4)$$

Solving the first integral results

$$\iint_S \sin(\gamma) r dr d\gamma = \frac{1}{2} \left\{ \int_{\beta_1}^{\beta_2} \left[r^2 \right]_{h_1/\sin(\gamma)}^{h_2/\cos(\gamma)} \sin(\gamma) d\gamma + \int_{\beta_2}^{\beta_3} \left[r^2 \right]_{h_4/\cos(\gamma)}^{h_2/\cos(\gamma)} \sin(\gamma) d\gamma \right.$$

$$\left. + \int_{\beta_3}^{\beta_4} \left[r^2 \right]_{h_4/\cos(\gamma)}^{h_3/\sin(\gamma)} \sin(\gamma) d\gamma \right\} \qquad (B.5)$$

Evaluating the first integral limits

$$\iint_S \sin(\gamma) r dr d\gamma = \frac{1}{2} \left\{ \int_{\beta_1}^{\beta_2} \left(h_2^2 \sin(\gamma)/\cos^2(\gamma) - h_1^2/\sin(\gamma) \right) d\gamma \right.$$

$$+ \int_{\beta_2}^{\beta_3} \left(h_2^2 \sin(\gamma)/\cos^2(\gamma) - h_4^2 \sin(\gamma)/\cos^2(\gamma) \right) d\gamma$$

$$\left. + \int_{\beta_3}^{\beta_4} \left(h_3^2/\sin(\gamma) - h_4^2 \sin(\gamma)/\cos^2(\gamma) \right) d\gamma \right\} \qquad (B.6)$$

Solving the second integral results

$$\iint_S \sin(\gamma) r dr d\gamma = \frac{1}{2} \left\{ \left[h_2^2/\cos(\gamma) - h_1^2 \ln[\csc(\gamma) - \cot(\gamma)] \right]_{\beta_1}^{\beta_2} + \left[h_2^2/\cos(\gamma) - h_4^2/\cos(\gamma) \right]_{\beta_2}^{\beta_3} \right.$$

$$\left. + \left[h_3^2 \ln[\csc(\gamma) - \cot(\gamma)] - h_4^2/\cos(\gamma) \right]_{\beta_3}^{\beta_4} \right\} \qquad (B.7)$$

Evaluating the second integral limits

$$= \frac{1}{2} \left\{ h_2^2/\cos(\beta_2) - h_2^2/\cos(\beta_1) - h_1^2 \ln\left[(\csc(\beta_2) - \cot(\beta_2))/(\csc(\beta_1) - \cot(\beta_1)) \right] \right.$$

$$+ h_2^2/\cos(\beta_3) - h_2^2/\cos(\beta_2) - h_4^2/\cos(\beta_3) + h_4^2/\cos(\beta_2)$$

$$\left. + h_3^2 \ln\left[(\csc(\beta_4) - \cot(\beta_4))/(\csc(\beta_3) - \cot(\beta_3)) \right] + h_4^2/\cos(\beta_3) - h_4^2/\cos(\beta_4) \right\}$$

$$(B.8)$$

170

Grouping and fartorising terms

$$
= \frac{1}{2} \Bigg\{ -h_2^2/\cos(\beta_1) + h_2^2/\cos(\beta_3) + h_4^2/\cos(\beta_2) - h_4^2/\cos(\beta_4)
$$

$$
- h_1^2 \ln\Bigg[\Big(\csc(\beta_2) - \cot(\beta_2)\Big)/\Big(\csc(\beta_1) - \cot(\beta_1)\Big) \Bigg]
$$

$$
+ h_3^2 \ln\Bigg[\Big(\csc(\beta_4) - \cot(\beta_4)\Big)/\Big(\csc(\beta_3) - \cot(\beta_3)\Big) \Bigg] \Bigg\} \tag{B.9}
$$

Substituting trigonometrics functions for their correspond trigonometric value according with Figure B.1

$$
= \frac{1}{2} \Bigg\{ h_2^2\Big(1/\cos(\beta_3) - 1/\cos(\beta_1)\Big) + h_4^2\Big(1/\cos(\beta_2) - 1/\cos(\beta_4)\Big)
$$

$$
- h_1^2 \ln\Bigg[\Big(\sqrt{h_1^2 + h_4^2}/h_1 - h_4/h_1\Big)/\Big(\sqrt{h_1^2 + h_2^2}/h_1 - h_2/h_1\Big) \Bigg]
$$

$$
+ h_3^2 \ln\Bigg[\Big(\sqrt{h_3^2 + h_4^2}/h_3 - h_4/h_3\Big)/\Big(\sqrt{h_2^2 + h_3^2}/h_3 - h_2/h_3\Big) \Bigg] \Bigg\} \tag{B.10}
$$

$$
= \frac{1}{2} \Bigg\{ h_2^2\Big(\sqrt{h_2^2 + h_3^2}/h_2 - \sqrt{h_1^2 + h_2^2}/h_2\Big) + h_4^2\Big(\sqrt{h_1^2 + h_4^2}/h_4 - \sqrt{h_3^2 + h_4^2}/h_4\Big)
$$

$$
- h_1^2 \ln\Bigg[\Big(\sqrt{h_1^2 + h_4^2}/h_1 - h_4/h_1\Big)/\Big(\sqrt{h_1^2 + h_2^2}/h_1 - h_2/h_1\Big) \Bigg]
$$

$$
+ h_3^2 \ln\Bigg[\Big(\sqrt{h_3^2 + h_4^2}/h_3 - h_4/h_3\Big)/\Big(\sqrt{h_2^2 + h_3^2}/h_3 - h_2/h_3\Big) \Bigg] \Bigg\} \tag{B.11}
$$

Finally, the resulted equation is:

$$f'_x = \frac{1}{2} \left\{ h_2 \left(\sqrt{h_2^2 + h_3^2} - \sqrt{h_1^2 + h_2^2} \right) + h_4 \left(\sqrt{h_1^2 + h_4^2} - \sqrt{h_3^2 + h_4^2} \right) \right.$$

$$- h_1^2 \ln \left[\left(\sqrt{h_1^2 + h_4^2} - h_4 \right) / \left(\sqrt{h_1^2 + h_2^2} - h_2 \right) \right]$$

$$\left. + h_3^2 \ln \left[\left(\sqrt{h_3^2 + h_4^2} - h_4 \right) / \left(\sqrt{h_2^2 + h_3^2} - h_2 \right) \right] \right\} \qquad \text{(B.12)}$$

for $\lim\limits_{h \to 0} \left[h \cdot \ln\left(\frac{1}{h}\right) \right] = 0$

B.2 $f'_y = \iint_\mathbf{S} \cos(\gamma) r \, dr \, d\gamma$

In particular to the Figure B.1, the limits of the integrals over the region S are:

$$\beta_1 \leq \gamma \leq \beta_2 \qquad for \qquad h_1/\sin(\gamma) \leq r \leq h_2/\cos(\gamma) \qquad \text{(B.13)}$$

$$\beta_2 \leq \gamma \leq \beta_3 \qquad for \qquad h_4/\cos(\gamma) \leq r \leq h_2/\cos(\gamma) \qquad \text{(B.14)}$$

$$\beta_3 \leq \gamma \leq \beta_4 \qquad for \qquad h_4/\cos(\gamma) \leq r \leq h_3/\sin(\gamma) \qquad \text{(B.15)}$$

Therefore, the limits of the integral over the region S are:

$$\iint_\mathbf{S} \cos(\gamma) r \, dr \, d\gamma = \int_{\beta_1}^{\beta_2} \int_{h_1/\sin(\gamma)}^{h_2/\cos(\gamma)} \cos(\gamma) r \, dr \, d\gamma + \int_{\beta_2}^{\beta_3} \int_{h_4/\cos(\gamma)}^{h_2/\cos(\gamma)} \cos(\gamma) r \, dr \, d\gamma$$

$$+ \int_{\beta_3}^{\beta_4} \int_{h_4/\cos(\gamma)}^{h_3/\sin(\gamma)} \cos(\gamma) r \, dr \, d\gamma \qquad \text{(B.16)}$$

Solving the first integral results

$$\iint_\mathbf{S} \cos(\gamma) r \, dr \, d\gamma = \frac{1}{2} \left\{ \int_{\beta_1}^{\beta_2} \left[r^2 \right]_{h_1/\sin(\gamma)}^{h_2/\cos(\gamma)} \cos(\gamma) d\gamma + \int_{\beta_2}^{\beta_3} \left[r^2 \right]_{h_4/\cos(\gamma)}^{h_2/\cos(\gamma)} \cos(\gamma) d\gamma \right.$$

$$\left. + \int_{\beta_3}^{\beta_4} \left[r^2 \right]_{h_4/\cos(\gamma)}^{h_3/\sin(\gamma)} \cos(\gamma) d\gamma \right\} \qquad \text{(B.17)}$$

Evaluating the first integral limits

$$\iint_S \cos(\gamma) r dr d\gamma = \frac{1}{2} \left\{ \int_{\beta_1}^{\beta_2} \left(h_2^2 / \cos(\gamma) - h_1^2 \cos(\gamma) / \sin^2(\gamma) \right) d\gamma \right.$$

$$+ \int_{\beta_2}^{\beta_3} \left(h_2^2 / \cos(\gamma) - h_4^2 / \cos(\gamma) \right) d\gamma$$

$$+ \left. \int_{\beta_3}^{\beta_4} \left(h_3^2 \cos(\gamma) / \sin^2(\gamma) - h_4^2 / \cos(\gamma) \right) d\gamma \right\} \qquad \text{(B.18)}$$

Solving the second integral results

$$\iint_S \cos(\gamma) r dr d\gamma = \frac{1}{2} \left\{ \left[h_2^2 \ln\left[\sec(\gamma) + \tan(\gamma) \right] + h_1^2 / \sin(\gamma) \right]_{\beta_1}^{\beta_2} \right.$$

$$+ \left[h_2^2 \ln\left[\sec(\gamma) + \tan(\gamma) \right] - h_4^2 \ln\left[\sec(\gamma) + \tan(\gamma) \right] \right]_{\beta_2}^{\beta_3}$$

$$- \left. \left[h_3^2 / \sin(\gamma) + h_4^2 \ln\left[\sec(\gamma) + \tan(\gamma) \right] \right]_{\beta_3}^{\beta_4} \right\} \qquad \text{(B.19)}$$

Evaluating the second integral limits

$$= \frac{1}{2} \left\{ h_1^2 / \sin(\beta_2) - h_1^2 / \sin(\beta_1) + h_1^2 \ln \left[(\sec(\beta_2) + \tan(\beta_2)) / (\sec(\beta_1) + \tan(\beta_1)) \right] \right.$$

$$+ h_2^2 \ln \left[(\sec(\beta_3) + \tan(\beta_3)) / (\sec(\beta_2) + \tan(\beta_2)) \right]$$

$$- h_4^2 \ln \left[(\sec(\beta_3) + \tan(\beta_3)) / (\sec(\beta_2) + \tan(\beta_2)) \right]$$

$$\left. - h_4^2 \ln \left[(\sec(\beta_4) - \tan(\beta_4)) / (\sec(\beta_3) - \tan(\beta_3)) \right] + h_3^2 / \sin(\beta_3) - h_3^2 / \cos(\beta_4) \right\}$$

(B.20)

Grouping and fartorising terms

$$= \frac{1}{2} \left\{ h_1^2 \left(1 / \sin(\beta_2) - 1 / \sin(\beta_1) \right) + h_3^2 \left(1 / \sin(\beta_3) - 1 / \sin(\beta_4) \right) \right.$$

$$+ h_2^2 \ln \left[\left(\sec(\beta_3) + \tan(\beta_3) \right) / \left(\sec(\beta_1) + \tan(\beta_1) \right) \right]$$

$$\left. - h_4^2 \ln \left[\left(\sec(\beta_4) + \tan(\beta_4) \right) / \left(\sec(\beta_2) + \tan(\beta_2) \right) \right] \right\}$$

(B.21)

175

Substituting trigonometrics functions for their correspond trigonometric value according with Figure B.1

$$= \frac{1}{2} \left\{ h_1^2 \left(\sqrt{h_1^2 + h_4^2}/h_1 - \sqrt{h_1^2 + h_2^2}/h_1 \right) + h_3^2 \left(\sqrt{h_2^2 + h_3^2}/h_3 - \sqrt{h_3^2 + h_4^2}/h_3 \right) \right.$$

$$+ h_2^2 \ln \left[\left(\sqrt{h_2^2 + h_3^2}/h_2 + h_3/h_2 \right) / \left(\sqrt{h_1^2 + h_2^2}/h_2 + h_1/h_2 \right) \right]$$

$$\left. - h_4^2 \ln \left[\left(\sqrt{h_3^2 + h_4^2}/h_4 - h_3/h_4 \right) / \left(\sqrt{h_1^2 + h_4^2}/h_4 - h_1/h_4 \right) \right] \right\} \qquad (B.22)$$

Finally, the resulted equation is:

$$f_y' = \frac{1}{2} \left\{ h_1 \left(\sqrt{h_1^2 + h_4^2} - \sqrt{h_1^2 + h_2^2} \right) + h_3 \left(\sqrt{h_2^2 + h_3^2} - \sqrt{h_3^2 + h_4^2} \right) \right.$$

$$+ h_2^2 \ln \left[\left(\sqrt{h_2^2 + h_3^2} + h_3 \right) / \left(\sqrt{h_1^2 + h_2^2} + h_1 \right) \right]$$

$$\left. + h_4^2 \ln \left[\left(\sqrt{h_1^2 + h_4^2} + h_1 \right) / \left(\sqrt{h_3^2 + h_4^2} + h_3 \right) \right] \right\} \qquad (B.23)$$

for $\lim\limits_{h \to 0} \left[h \cdot \ln \left(\frac{1}{h} \right) \right] = 0$

176

B.3 $\quad m_f = \iint_S \big(R\cos(\alpha - \gamma) - r\big)r\,dr\,d\gamma$

In particular to the Figure B.1, the limits of the integrals defining the region S are:

$$\beta_1 \leq \gamma \leq \beta_2 \qquad for \qquad h_1/\sin(\gamma) \leq r \leq h_2/\cos(\gamma) \qquad \text{(B.24)}$$

$$\beta_2 \leq \gamma \leq \beta_3 \qquad for \qquad h_4/\cos(\gamma) \leq r \leq h_2/\cos(\gamma) \qquad \text{(B.25)}$$

$$\beta_3 \leq \gamma \leq \beta_4 \qquad for \qquad h_4/\cos(\gamma) \leq r \leq h_3/\sin(\gamma) \qquad \text{(B.26)}$$

Also,

$$\iint_S \big(R\cos(\alpha - \gamma) - r\big)r\,dr\,d\gamma = \iint_S \big(R\cos(\alpha)\cos(\gamma) + R\sin(\alpha)\sin(\gamma) - r\big)r\,dr\,d\gamma$$

$$= R\cos(\alpha)\iint_S \cos(\gamma)r\,dr\,d\gamma + R\sin(\alpha)\iint_S \sin(\gamma)r\,dr\,d\gamma$$

$$- \iint_S r^2\,dr\,d\gamma \qquad \text{(B.27)}$$

The first tow integrals of the Equation (B.27) were solved (sections B.1 and B.2). Therefore, the limits of the remining integral over the region S are:

$$\iint_S r^2\,dr\,d\gamma = \int_{\beta_1}^{\beta_2}\int_{h_1/\sin(\gamma)}^{h_2/\cos(\gamma)} r^2\,dr\,d\gamma + \int_{\beta_2}^{\beta_3}\int_{h_4/\cos(\gamma)}^{h_2/\cos(\gamma)} r^2\,dr\,d\gamma + \int_{\beta_3}^{\beta_4}\int_{h_4/\cos(\gamma)}^{h_3/\sin(\gamma)} r^2\,dr\,d\gamma$$

$$\text{(B.28)}$$

Solving the first integral results

$$\iint_S r^2\,dr\,d\gamma = \frac{1}{3}\left\{ \int_{\beta_1}^{\beta_2}\Big[r^3\Big]_{h_1/\sin(\gamma)}^{h_2/\cos(\gamma)}d\gamma + \int_{\beta_2}^{\beta_3}\Big[r^3\Big]_{h_4/\cos(\gamma)}^{h_2/\cos(\gamma)}d\gamma + \int_{\beta_3}^{\beta_4}\Big[r^3\Big]_{h_4/\cos(\gamma)}^{h_3/\sin(\gamma)}d\gamma \right\}$$

$$\text{(B.29)}$$

Evaluating the first integral limits

$$= \frac{1}{3} \left\{ \int_{\beta_1}^{\beta_2} \left(h_2^3 / \cos^3(\gamma) - h_1^3 / \sin^3(\gamma) \right) d\gamma + \int_{\beta_2}^{\beta_3} \left(h_2^3 / \cos^3(\gamma) - h_4^3 / \cos^3(\gamma) \right) d\gamma \right.$$

$$\left. + \int_{\beta_3}^{\beta_4} \left(h_3^3 / \sin^3(\gamma) - h_4^3 / \cos^3(\gamma) \right) d\gamma \right\} \tag{B.30}$$

Solving the second integral

$$= \frac{1}{6} \left\{ \left[h_2^3 \sin(\gamma) / \cos^2(\gamma) + \ln\left[\sec(\gamma) + \tan(\gamma)\right] + h_1^3 \cos(\gamma) / \sin(\gamma) - \ln\left[\csc(\gamma) - \cot(\gamma)\right] \right]_{\beta_1}^{\beta_2} \right.$$

$$+ \left[h_2^3 \sin(\gamma) / \cos^2(\gamma) + h_2^3 \ln\left[\sec(\gamma) + \tan(\gamma)\right] - h_4^3 \sin(\gamma) / \cos^2(\gamma) - h_4^3 \ln\left[\sec(\gamma) + \tan(\gamma)\right] \right]_{\beta_2}^{\beta_3}$$

$$\left. + \left[h_3^3 \ln\left[\csc(\gamma) - \cot(\gamma) - h_3^3 \cos(\gamma) / \sin^2(\gamma)\right] - h_4^3 \sin(\gamma) / \cos^2(\gamma) - h_4^3 \ln\left[\sec(\gamma) + \tan(\gamma)\right] \right]_{\beta_3}^{\beta_4} \right\}$$

$$\tag{B.31}$$

Evaluating the second integral limits

$$
\begin{aligned}
=\frac{1}{6}\Bigg\{ & h_2^3\Big(\sin(\beta_2)/\cos^2(\beta_2)-\sin(\beta_1)/\cos^2(\beta_1)\Big)+h_2^3\ln\Big[\big(\sec(\beta_2)+\tan(\beta_2)\big)/\big(\sec(\beta_1)+\tan(\beta_1)\big)\Big] \\
& +h_1^3\Big(\cos(\beta_2)/\sin^2(\beta_2)-\cos(\beta_1)/\sin^2(\beta_1)\Big)-h_1^3\ln\Big[\big(\csc(\beta_2)-\cot(\beta_2)\big)/\big(\csc(\beta_1)-\cot(\beta_1)\big)\Big] \\
& +h_2^3\Big(\sin(\beta_3)/\cos^2(\beta_3)-\sin(\beta_2)/\cos^2(\beta_2)\Big)+h_2^3\ln\Big[\big(\sec(\beta_3)+\tan(\beta_3)\big)/\big(\sec(\beta_2)+\tan(\beta_2)\big)\Big] \\
& -h_4^3\Big(\sin(\beta_3)/\cos^2(\beta_3)-\sin(\beta_2)/\cos^2(\beta_2)\Big)-h_4^3\ln\Big[\big(\sec(\beta_3)+\tan(\beta_3)\big)/\big(\sec(\beta_2)+\tan(\beta_2)\big)\Big] \\
& -h_3^3\Big(\cos(\beta_4)/\sin^2(\beta_4)-\cos(\beta_3)/\sin^2(\beta_3)\Big)+h_3^3\ln\Big[\big(\csc(\beta_4)-\cot(\beta_4)\big)/\big(\csc(\beta_3)-\cot(\beta_3)\big)\Big] \\
& -h_4^3\Big(\sin(\beta_4)/\cos^2(\beta_4)-\sin(\beta_3)/\cos^2(\beta_3)\Big)+h_4^3\ln\Big[\big(\sec(\beta_4)+\tan(\beta_4)\big)/\big(\sec(\beta_3)+\tan(\beta_3)\big)\Big] \Bigg\}
\end{aligned}
$$

$$\text{(B.32)}$$

$$
\begin{aligned}
=\frac{1}{6}\Bigg\{ & h_1^3\Big(\cos(\beta_2)/\sin^2(\beta_2)-\cos(\beta_1)/\sin^2(\beta_1)\Big)+h_2^3\Big(\sin(\beta_3)/\cos^2(\beta_3)-\sin(\beta_2)/\cos^2(\beta_2)\Big) \\
& -h_3^3\Big(\cos(\beta_4)/\sin^2(\beta_4)-\cos(\beta_3)/\sin^2(\beta_3)\Big)-h_4^3\Big(\sin(\beta_4)/\cos^2(\beta_4)-\sin(\beta_2)/\cos^2(\beta_2)\Big) \\
& -h_1^3\ln\Big[\big(\csc(\beta_2)-\cot(\beta_2)\big)/\big(\csc(\beta_1)-\cot(\beta_1)\big)\Big] \\
& +h_2^3\ln\Big[\big(\sec(\beta_3)+\tan(\beta_3)\big)/\big(\sec(\beta_2)+\tan(\beta_2)\big)\Big] \\
& +h_3^3\ln\Big[\big(\csc(\beta_4)-\cot(\beta_4)\big)/\big(\csc(\beta_3)-\cot(\beta_3)\big)\Big] \\
& -h_4^3\ln\Big[\big(\sec(\beta_4)+\tan(\beta_4)\big)/\big(\sec(\beta_2)+\tan(\beta_2)\big)\Big] \Bigg\}
\end{aligned}
$$

$$\text{(B.33)}$$

Substituting trigonometrics functions for their correspond trigonometric value according with Figure B.1

$$=\frac{1}{6}\Bigg\{\ h_1^3\bigg[\Big(h_4/\sqrt{h_1^2+h_4^2}\Big)/\Big(h_1^2/(h_1^2+h_4^2)\Big)-\Big(h_2/\sqrt{h_1^2+h_2^2}\Big)/\Big(h_1^2/(h_1^2+h_2^2)\Big)\bigg]$$

$$+\ h_2^3\bigg[\Big(h_3/\sqrt{h_2^2+h_3^2}\Big)/\Big(h_2^2/(h_2^2+h_3^2)\Big)-\Big(h_1/\sqrt{h_1^2+h_2^2}\Big)/\Big(h_2^2/(h_1^2+h_2^2)\Big)\bigg]$$

$$-\ h_3^3\bigg[\Big(h_4/\sqrt{h_3^2+h_4^2}\Big)/\Big(h_3^2/(h_3^2+h_4^2)\Big)-\Big(h_2/\sqrt{h_2^2+h_3^2}\Big)/\Big(h_3^2/(h_2^2+h_3^2)\Big)\bigg]$$

$$-\ h_4^3\bigg[\Big(h_3/\sqrt{h_3^2+h_4^2}\Big)/\Big(h_4^2/(h_3^2+h_4^2)\Big)-\Big(h_1/\sqrt{h_1^2+h_4^2}\Big)/\Big(h_4^2/(h_1^2+h_4^2)\Big)\bigg]$$

$$-\ h_1^3\ln\bigg[\Big(\sqrt{h_1^2+h_4^2}/h_1-h_4/h_1\Big)/\Big(\sqrt{h_1^2+h_2^2}/h_1-h_2/h_1\Big)\bigg]$$

$$+\ h_2^3\ln\bigg[\Big(\sqrt{h_2^2+h_3^2}/h_2+h_3/h_2\Big)/\Big(\sqrt{h_1^2+h_2^2}/h_2+h_1/h_2\Big)\bigg]$$

$$+\ h_3^3\ln\bigg[\Big(\sqrt{h_3^2+h_4^2}/h_3-h_4/h_3\Big)/\Big(\sqrt{h_2^2+h_3^2}/h_3-h_2/h_3\Big)\bigg]$$

$$-\ h_4^3\ln\bigg[\Big(\sqrt{h_3^2+h_4^2}/h_4+h_3/h_4\Big)/\Big(\sqrt{h_1^2+h_4^2}/h_4+h_1/h_4\Big)\bigg]\ \Bigg\} \tag{B.34}$$

$$=\frac{1}{6}\Bigg\{\ h_1\Big(h_4\sqrt{h_1^2+h_4^2}-h_2\sqrt{h_1^2+h_2^2}\Big)+h_2\Big(h_3\sqrt{h_2^2+h_3^2}-h_1\sqrt{h_1^2+h_2^2}\Big)$$

$$-\ h_3\Big(h_4\sqrt{h_3^2+h_4^2}-h_2\sqrt{h_2^2+h_3^2}\Big)-h_4\Big(h_3\sqrt{h_3^2+h_4^2}-h_1\sqrt{h_1^2+h_4^2}\Big)$$

$$-\ h_1^3\ln\bigg[\Big(\sqrt{h_1^2+h_4^2}-h_4\Big)/\Big(\sqrt{h_1^2+h_2^2}-h_2\Big)\bigg]$$

$$+\ h_2^3\ln\bigg[\Big(\sqrt{h_2^2+h_3^2}+h_3\Big)/\Big(\sqrt{h_1^2+h_2^2}+h_1\Big)\bigg]$$

$$+\ h_3^3\ln\bigg[\Big(\sqrt{h_3^2+h_4^2}-h_4\Big)/\Big(\sqrt{h_2^2+h_3^2}-h_2\Big)\bigg]$$

$$-\ h_4^3\ln\bigg[\Big(\sqrt{h_3^2+h_4^2}+h_3\Big)/\Big(\sqrt{h_1^2+h_4^2}+h_1\Big)\bigg]\ \Bigg\} \tag{B.35}$$

$$
= \frac{1}{6} \Bigg\{ -2h_1 h_2 \sqrt{h_1^2 + h_4^2} + 2h_2 h_3 \sqrt{h_2^2 + h_3^2} - 2h_3 h_4 \sqrt{h_3^2 + h_4^2} + 2h_1 h_4 \sqrt{h_1^2 + h_4^2}
$$

$$
- h_1^3 \ln\left[\left(\sqrt{h_1^2 + h_4^2} - h_4 \right) \Big/ \left(\sqrt{h_1^2 + h_2^2} - h_2 \right) \right]
$$

$$
+ h_2^3 \ln\left[\left(\sqrt{h_2^2 + h_3^2} + h_3 \right) \Big/ \left(\sqrt{h_1^2 + h_2^2} + h_1 \right) \right]
$$

$$
+ h_3^3 \ln\left[\left(\sqrt{h_3^2 + h_4^2} - h_4 \right) \Big/ \left(\sqrt{h_2^2 + h_3^2} - h_2 \right) \right]
$$

$$
- h_4^3 \ln\left[\left(\sqrt{h_3^2 + h_4^2} + h_3 \right) \Big/ \left(\sqrt{h_1^2 + h_4^2} + h_1 \right) \right] \Bigg\} \tag{B.36}
$$

Therefore, the solution for the third integral is:

$$
\iint_{\mathbf{S}} r^2 dr d\gamma = \frac{1}{3} \Bigg\{ -h_1 h_2 \sqrt{h_1^2 + h_4^2} + h_2 h_3 \sqrt{h_2^2 + h_3^2} - h_3 h_4 \sqrt{h_3^2 + h_4^2} + h_1 h_4 \sqrt{h_1^2 + h_4^2} \Bigg\}
$$

$$
+ \frac{1}{6} \Bigg\{ h_1^3 \ln\left[\left(\sqrt{h_1^2 + h_2^2} - h_2 \right) \Big/ \left(\sqrt{h_1^2 + h_4^2} - h_4 \right) \right]
$$

$$
+ h_2^3 \ln\left[\left(\sqrt{h_2^2 + h_3^2} + h_3 \right) \Big/ \left(\sqrt{h_1^2 + h_2^2} + h_1 \right) \right]
$$

$$
+ h_3^3 \ln\left[\left(\sqrt{h_3^2 + h_4^2} - h_4 \right) \Big/ \left(\sqrt{h_2^2 + h_3^2} - h_2 \right) \right]
$$

$$
+ h_4^3 \ln\left[\left(\sqrt{h_1^2 + h_4^2} + h_1 \right) \Big/ \left(\sqrt{h_3^2 + h_4^2} + h_3 \right) \right] \Bigg\} \tag{B.37}
$$

for $\lim\limits_{h \to 0}\left[h \cdot \ln\left(\frac{1}{h}\right) \right] = 0$.

Finally, the complete solution for the integral that defines the frictional moment $m_f = \iint_{\mathbf{S}} \left(R \cos(\alpha - \gamma) - r \right) r dr d\gamma$ is given as:

$$
\iint_{\mathbf{S}} \left(R \cos(\alpha - \gamma) - r \right) r dr d\gamma = R \cos(\alpha) \iint_{\mathbf{S}} \cos(\gamma) r dr d\gamma + R \sin(\alpha) \iint_{\mathbf{S}} \sin(\gamma) r dr d\gamma
$$

$$
- \iint_{\mathbf{S}} r^2 dr d\gamma \tag{B.38}
$$

181

$$m_f = \frac{R\cos(\alpha)}{2}\left\{ h_1\left(\sqrt{h_1^2+h_4^2}-\sqrt{h_1^2+h_2^2}\right)+h_3\left(\sqrt{h_2^2+h_3^2}-\sqrt{h_3^2+h_4^2}\right)\right.$$

$$+\,h_2^2\,\ln\left[\left(\sqrt{h_2^2+h_3^2}+h_3\right)/\left(\sqrt{h_1^2+h_2^2}+h_1\right)\right]$$

$$\left.+\,h_4^2\,\ln\left[\left(\sqrt{h_1^2+h_4^2}+h_1\right)/\left(\sqrt{h_3^2+h_4^2}+h_3\right)\right]\right\}$$

$$+\,\frac{R\sin(\alpha)}{2}\left\{ h_2\left(\sqrt{h_2^2+h_3^2}-\sqrt{h_1^2+h_2^2}\right)+h_4\left(\sqrt{h_1^2+h_4^2}-\sqrt{h_3^2+h_4^2}\right)\right.$$

$$-\,h_1^2\,\ln\left[\left(\sqrt{h_1^2+h_4^2}-h_4\right)/\left(\sqrt{h_1^2+h_2^2}-h_2\right)\right]$$

$$\left.+\,h_3^2\,\ln\left[\left(\sqrt{h_3^2+h_4^2}-h_4\right)/\left(\sqrt{h_2^2+h_3^2}-h_2\right)\right]\right\}$$

$$-\,\frac{1}{3}\left\{-h_1h_2\sqrt{h_1^2+h_4^2}+h_2h_3\sqrt{h_2^2+h_3^2}-h_3h_4\sqrt{h_3^2+h_4^2}+h_1h_4\sqrt{h_1^2+h_4^2}\right\}$$

$$-\,\frac{1}{6}\left\{ h_1^3\,\ln\left[\left(\sqrt{h_1^2+h_2^2}-h_2\right)/\left(\sqrt{h_1^2+h_4^2}-h_4\right)\right]\right.$$

$$+\,h_2^3\,\ln\left[\left(\sqrt{h_2^2+h_3^2}+h_3\right)/\left(\sqrt{h_1^2+h_2^2}+h_1\right)\right]$$

$$+\,h_3^3\,\ln\left[\left(\sqrt{h_3^2+h_4^2}-h_4\right)/\left(\sqrt{h_2^2+h_3^2}-h_2\right)\right]$$

$$\left.+\,h_4^3\,\ln\left[\left(\sqrt{h_1^2+h_4^2}+h_1\right)/\left(\sqrt{h_3^2+h_4^2}+h_3\right)\right]\right\},\; for \lim_{h\to 0}\left[h\cdot\ln\left(\frac{1}{h}\right)\right]=0.$$

(B.39)

References

[1] Chen, H. , Xi, N. , Li, G. , Zhang, J. , and Saeed, A. . Automated nano-assembly of nanoscale structures. In *IEEE 2004 4th Conference on Nanotechnology*, pp. 465–467, August 2004.

[2] Heping, C. , Ning, X. , Guangyong, L. , and Saeed, A. . CAD-guided manufacturing of nanostructures using nanoparticles. In *IROS 2004 IEEE/RSJ Proceedings of International Conference on Intelligent Robots and Systems*, Sendai, Japan, pp. 595 – 600, 28 September - 2 October 2004.

[3] McNally, H. , Pingle, M. , Lee, S. , Guo, D. , Bergstrom, D. , and Bashir, R. . Self-assembly of micro- and nano-scale particles using bio-inspired events. *Applied Surface Science*, 214(14), pp. 109–119, 2003.

[4] Wejinya, U. , Xi, N. , Shen, Y. , and Lai, K. W. C. . Modeling dielectrophoretic force for manipulating carbon nanotubes (CNTs). In *IEEE/ASME 2007 International Conference on Advanced Intelligent Mechatronics*, pp. 1–6, September 2007.

[5] Fahlbusch, S. , Mazerolle, S. , Breguet, J. M. , Steinecker, A. , Agnus, J. , Pérez, R. , and Michler, J. . Nanomanipulation in a scanning electron microscope. *Journal of Materials Processing Technology*, 167(2-3), pp. 371–382, 2005.

[6] Li, G. , Xi, N. , Chen, H. , Saeed, A. , and Yu, M. . Assembly of nanostructure using AFM based nanomanipulation system. In *ICRA '04. Proceedings of the IEEE International Conference on Robotics and Automation*, New Orleans, L.A., USA, pp. 428–433, April 2004.

[7] Xie, H. , Vitard, J. , Haliyo, D. , and Regnier, S. . Enhanced accuracy of force application for AFM nanomanipulation using nonlinear calibration of optical levers. *IEEE Sensors Journal*, 8(8), pp. 1478 –1485, August 2008.

[8] Andersen, K. , Petersen, D. , Carlson, K. , Molhave, K. , Sardan, O. , Horsewell, A. , Eichhorn, V. , Fatikow, S. , and Boggild, P. . Multimodal electrothermal silicon micro-grippers for nanotube manipulation. *IEEE Transactions on Nanotechnology*, 8(1), pp. 76–85, January 2009.

[9] Liu, Z. , Li, Z. , Wei, G. , Song, Y. , Wang, L. , and Sun, L. . Manipulation, dissection, and lithography using modified tapping mode atomic force microscope. *Microscopy Research and Technique*, 69(12), pp. 998–1004, September 2006.

[10] Xi, Z. J.-C. H. C. H. W. K. , N. and Li, G. . Atomic force microscope based nano robotic system for nanomanipulation, 2007.

[11] Lai, K. W. C. , Xi, N. , Fung, C. K. M. , Zhang, J. , Chen, H. , Luo, Y. , and Wejinya, U. C. . Automated nanomanufacturing system to assemble carbon nanotube based devices. *The International Journal of Robotics Research*, 28(4), pp. 523–536, 2009.

[12] Hui, X. and Régnier, S. . High-efficiency automated nanomanipulation with parallel imaging/manipulation force microscopy. *IEEE Transactions on Nanotechnology*, 11(1), pp. 21–33, January 2012.

[13] Hayes, C. and Aguilar, J. . Dielectrophoretic manipulation of micro and nanoscale objects with a modified atomic force microscope tip, 1998.

[14] Toset, J. , Casuso, I. , Samitier, J. , and Gomila, G. . Deflection-voltage curve mod-elling in atomic force microscope and its use in DC electrostatic manipulation of gold nanopartilces. *Nanotechnology*, 18(1), pp. 015503–015512, 2007.

[15] Fatikow, S. , Eichhorn, V. , Krohs, F. , Mircea, I. , Stolle, C. , and Hagemann, S. . Development of automated microrobot-based nanohandling stations for nanocharacterization. *Microsyst. Technol.*, 14(4), pp. 463–474, March 2008.

[16] Martin, M. , Roschier, L. , Hakonen, P. , Parts, U. , Paalanen, M. , Schleicher, B. , and Kauppinen, E. I. . Manipulation of Ag nanoparticles utilizing noncontact atomic force microscopy. *Applied Physics Letters*, 73(11), pp. 1505–1507, 1998.

[17] Postma, a. S.-A. , H.W.C. and Dekker, C. . Manipulation and imaging of individual single-walled carbon nanotubes with an atomic force microscope. *Advanced Materials*, 12(17), pp. 1299–1302, 2000.

[18] Ritter, C. , Heyde, a. S.-U. , M., and Rademann, K. . Controlled translational manipulation of small latex spheres by dynamic force microscopy. *Langmuir*, 18(21), pp. 7798–7803, 2002.

[19] Decossas, S. , Mazen, F. , Baron, T. , Bremond, G. , and Souifi, A. . Atomic force microscopy nanomanipulation of silicon nanocrystals for nanodevice fabrication. *Nanotechnology*, 14, pp. 1272–1278, 2003.

[20] Yun, Y. , Ah, a. K.-S. , C.S., Yun, W. , Park, B. , and Ha, D. . Manipulation of freestanding Au nanogears using an atomic force microscope. *Nanotechnology*, 18, pp. 505304–1 – 505304–5, 2007.

[21] Tian, X. , Wang, Y. , Xi, N. , Dong, Z. , and Tung, S. . Pulse gas alignment and AFM manipulation of single-wall carbon nanotube. *Chinese Science Bulletin*, 53(22), pp. 3590–3596, 2008.

[22] Tranvouez, E. and Orieux, a. B.-D. E. a. D. C. a. H. V. a. C. G. a. D. G. , A. Manipulation of cadmium selenide nanorods with an atomic force microscope. *Nanotechnology*, 20, pp. 165304 – 165314, 2009.

[23] Lievonen, J. and Ahlskog, M. . Lateral force microscopy of multiwalled carbon nanotubes. *Ultramicroscopy*, 109(7), pp. 825 – 829, 2009.

[24] Fukuda, T. , Arai, F. , and Dong, L. . Assembly of nanodevices with carbon nanotubes through nanorobotic manipulations. *Proceedings of the IEEE*, 91(11), pp. 1803 – 1818, November 2003.

[25] Fukuda, T. , Arai, F. , and Dong, L. . Micro and nano robotic manipulation systems, 2004. URL `http://conf.uni-obuda.hu/jubilee/Fukuda.pdf`. [Accessed 16th June 2008].

[26] Sitti, M. . Survey of nanomanipulation systems. In *IEEE-NANO 2001. Proceedings of the 2001 1st IEEE Conference on Nanotechnology*, pp. 75–80, October 2001.

[27] Sitti, M. , Aruk, B. , Shintani, K. , and Hashimoto, H. . Scaled teleoperation system for nanoscale interaction and manipulation. *Advanced Robotics*, 17(3), pp. 275–291, 2002.

[28] Sitti, M. . Atomic force microscope probe based controlled pushing for nanotribological characterization. *IEEE/ASME Transactions on Mechatronics*, 9(2), pp. 343–349, 2004.

[29] Requicha, A. . X. Nanomanipulation with the atomic force microscope. *IEEE/ASME Transactions on Mechatronics*, 9(1), pp. 1–39, 2004.

[30] Saeidpourazar, R. and Jalili, N. . Nano-robotic manipulation using a RRP nanomanipulator: Part A - mathematical modeling and development of a robust adaptive driving mechanism. *Applied Mathematics and Computation*, 206(2), pp. 618–627, 2008.

[31] Saeidpourazar, R. and Jalili, N. . Nano robotic manipulation using a RRP nanomanipulator: Part B - robust control of manipulators tip using fused visual servoing and force sensor feedbacks. *Applied Mathematics and Computation*, 206(1), pp. 628–642, 2008.

[32] Binnig, G. and Rohrer, H. . Scanning tunneling microscopy - from birth to adolescence, 1986.

[33] Binnig, G. , Quate, C. , and Gerber, C. . Atomic force microscope. *Physical Review Letters*, 56(9), pp. 930–933, 1986.

[34] Junno, T. , Deppert, K. , Montelius, L. , and Samuelson, L. . Controlled manipulation of nanoparticles with an atomic force microscope. *Applied Physics Letters*, 66(26), pp. 3627–3629, 1995.

[35] Hu, J. , Zhang, Y. , Gao, H. , Li, M. , and Hartmann, U. . Artificial DNA patterns by mechanical nanomanipulation. *Nano Letters*, 2(1), pp. 55–57, 2002.

[36] Landousy, F. and Cam, E. . Probing DNA-protein interactions with atomic force microscopy, 2004.

[37] Rubio Sierra, F. , Heckl, W. , and Stark, R. . Nanomanipulation by atomic force microscopy. *Advanced Engineering Materials*, 7(4), pp. 193–196, 2005.

[38] Du, S. and Li, Y. . Micromanipulation based on AFM: Probe tip selection. In *IEEE-NANO 2007 7th IEEE Conference on Nanotechnology*, Hong Kong, pp. 506–510, 2-5 August 2007.

[39] Ikai, A. , Afrin, R. , and Sekiguchi, H. . Pulling and pushing protein molecules by AFM. *Current Nanoscience*, 3(1), pp. 17–19, 2007.

[40] Zhang, J. , Xi, N. , Liu, L. , Chen, H. , Lai, K. , and Li, G. . Atomic force yields a master nanomanipulator. *IEEE Nanotechnology Magazine*, 2(2), pp. 13–17, June 2008.

[41] Yang, Y. , Dong, Z. , and Li, W. . Towards automated nanomanipulation of nano-bio-entities using real-time molecular force feedback information. In *ICIA 2008 International Conference on Information and Automation*, Zhangjiajie, China, pp. 1490–1493, 20-23 June 2008.

[42] Yongliang, Y. , Zaili, D. , Yanli, Q. , Minglin, L. , and Li, W. . A programmable AFM-based nanomanipulation method using vibration-mode operation. In *NEMS 2008 3rd IEEE International Conference on Nano/Micro Engineered and Molecular Systems*, Sanya, China, pp. 681–685, 6-9 January 2008.

[43] Schaefer, D. M. , Reifenberger, R. , Patil, A. , and Andres, R. P. . Fabrication of two-dimensional arrays of nanometer-size clusters with the atomic force microscope. *Applied Physics Letters*, 66(8), pp. 1012–1014, 1995.

[44] Hansen, T. , Kuhle, A. , Sorensen, A. , Bohr, J. , and Lindelof, P. . A technique for positioning nanoparticles using an atomic force microscope. *Nanotechnology*, 9, pp. 337–342, 1998.

[45] Hertel, T. , Martel, R. , and Avouris, P. . Manipulation of individual carbon nanotubes and their iteraction with surfaces. *Physics & Chemical B*, 102, pp. 910–915, 1998.

[46] Kashiwase, a. I.-T. , Y., Oya, T. , and Ogino, T. . Manipulation and soldering of carbon nanotubes using atomic force microscope. *Applied Surface Science*, 254, pp. 7897–7900, 2008.

[47] Paolicelli, G. , Mougin, K. , Vanossi, A. , and Valeri, S. . Adhesion detachment and movement of gold nanoclusters induced by dynamic atomic force microscopy. *Journal of Physics:Condensed Matter*, 20, pp. 354011–1 –354011–6, 2008.

[48] Tong, L. , Li, Z. , Zhu, T. , Xu, H. , , and Liu, Z. . Single gold-nanoparticle-enhanced raman scattering of individual single-walled carbon nanotubes via atomic force microscope manipulation. *The Journal of Physical Chemistry C*, 112(18), pp. 7119–7123, 2008.

[49] Suümer, B. and Sitti, M. . Rolling and spinning friction characterization of fine particles using lateral force microscopy based contact pushing. *Journal of Adhesion Science and Technology*, 2008.

[50] Lynch, N. , Onal, C. , Schuster, E. , and Sitti, M. . A strategy for vision-based controlled pushing of microparticles. In *IEEE 2007 International Conference on Robotics and Automation*, Roma, Italy, pp. 1413–1418, April 2007.

[51] Onal, C. D. and Sitti, M. . Autonomous 2D microparticle manipulation based on visual feedback. In *IEEE/ASME 2007. International Conference on Advanced Intelligent Mechatronics*, pp. 1–6, 2007.

[52] Sitti, M. . Atomic force microscope probe based controlled pushing for nano-tribological characterization. *IEEE/ASME Transactions on Mechatronics*, 8(3), 2003.

[53] Sitti, M. and Hashimoto, H. . Teleoperated touch feedback from the surfaces at the nanoscale: modeling and experiments. *IEEE/ASME Transactions on Mechatronics.*, 8 (2), pp. 287–298, 2003.

[54] Tafazzoli, A. and Sitti, M. . Dynamic modes of nanoparticle motion during nanoprobe-based manipulation. In *IEEE 2004. Procedings of the 4th International Conference on Nanotechnology*, pp. 35–37, 2004.

[55] Sitti, M. . Teleoperated and automatic nanomanipulation systems using atomic force microscope probes. In *IEEE 2003. Proceedings of the 42nd International Conference on Decision and Control*, Maui, Hawaii, USA, pp. 2118–2123, December 2003.

[56] Thorsten, H. and Markus, S. . The study of molecular interactions by AFM force spectroscopy. *Macromolecular Rapid Communications*, 22(13), pp. 989–1016, 2001.

[57] Law, B. and Rieutord, F. . Electrostatic forces in atomic force microscopy. *Physical Review B*, 66, pp. 035402–1 – 035402–6, 2002.

[58] Lee, a. S.-W. , S. AFM study of repulsive van der waals forces between teflon AFTM thin film and silica or aluminia. *Colloids and Surfaces A: Physicochemical and Enineering Aspects*, 204, pp. 43–50, 2002.

[59] Israelachvili, J. . *Intermolecular and Surfaces Forces*. Second Edition. Academic Press Harcourt Brace & Company, 1997.

[60] Hamaker, H. . The london-van der waals attraction between spherical particles. *Physica*, 4(10), pp. 1058–1070, 1937.

[61] Banerjee, A. , Ferrante, J. , and Smith, J. . *Fundamentals of Adhesion*. Plenum, New York, 1991.

[62] Ferrante, J. and Smith, J. R. . Theory of the bimetallic interface. *Phys. Rev. B*, 31, pp. 3427–3434, Mar 1985.

[63] Israelachvili, J. N. and Tabor, D. . The measurement of van der waals dispersion forces in the range 1.5 to 130 nm. *Proceedings of the Royal Society of London. A. Mathematical and Physical Sciences*, 331(1584), pp. 19–38, 1972.

[64] Loskill, P. , Puthoff, J. , Wilkinson, M. , Mecke, K. , Jacobs, K. , and Autumn, K. . Macroscale adhesion of gecko setae reflects nanoscale differences in subsurface composition. *Journal of The Royal Society Interface*, 10(78), January 2013.

[65] Buffat, P. and Borel, J.-P. . Size effect on the melting temperature of gold particles. *Phys. Rev. A*, 13, pp. 2287–2298, Jun 1976.

[66] Johnson, K. L. , Kendall, K. , and Roberts, A. D. . Surface energy and the contact of elastic solids. *Proceedings of the Royal Society of London. A. Mathematical and Physical Sciences*, 324(1558), pp. 301–313, 1971.

[67] Rabinovich, Y. I. , Adler, J. J. , Esayanur, M. S. , Ata, A. , Singh, R. K. , and Moudgil, B. M. . Capillary forces between surfaces with nanoscale roughness. *Advances in Colloid and Interface Science*, 96(1-3), pp. 213–230, 2002.

[68] Lambert, P. , Chau, A. , Delchambre, A. , and Regnier, S. . Comparison between two capillary forces models. *Langmuir*, 24(7), pp. 3157–3163, 2008.

[69] Falvo, M. , Taylor II, R. , Helser, A. , Chi, V. , Brooks Jr, F. , Washburn, S. , and Superfine, R. . Nanometre-scale rolling and sliding of carbon nanotubes. *Letters to Nature*, 397, pp. 236–238, 1999.

[70] Jensen, J. H. . Rules for rolling as a rotation about the instantaneous point of contact. *European Journal of Physics*, 32(2), pp. 389–397, 2011.

[71] Johnson, K. . *Contact Mechanics*. University of Cambridge, 1985.

[72] Chaudhury, M. . Interfacial interaction between low-energy surfaces. *Materials Science and Engineering: R: Reports*, 16(3), pp. 97–159, 1996.

[73] Stoer, J. and Bulirsch, R. . *Introduction to numerical analysis*. Springer - Verlag New York, third edition, 2002.

[74] Wiley, B. J. , Chen, Y. , McLellan, J. M. , Xiong, Y. , Li, Z.-Y. , Ginger, D. , and Xia, Y. . Synthesis and optical properties of silver nanobars and nanorice. *Nano Letters*, 7(4), pp. 1032–1036, 2007.

[75] Mason, T. , Matthew. *Mechanics of robotic manipulation*. MIT Press, 2001.

[76] Cheung, K. C. . *Hig-speed manipulation of discrete objects by pushing or pulling*. PhD thesis, School of Electrical, Electronic and Systems Engineering, University of Wales Collage of Cardiff, 1989.

[77] Pham, D. , Cheung, K. , and Yeo, S. . Initial motion of rectangular object being pushed or pulled. In *IEEE 1990. Proceedings of the IEEE International Conference on Robotics and Automation*, pp. 1046–1050, 13-18 May 1990.

[78] Peshkin, M. A. and Sanderson, A. C. . Minimization of energy in quasistatic manipulation. *IEEE Transactions on Robotics and Automation*, 5(1), February 1989.

[79] Jung-Hui, H. and Shuo-Hung, C. . Tribological interaction between multi-walled carbon nanotubes and silica surface using lateral force microscopy. *Wear*, 266(9-10), pp. 952–959, 2009.

[80] Huntington, E. V. . The theorem of rotation in elementary mechanics. *The American Mathematical Monthly*, 21(10), pp. 315–320, 1914.

[81] Wu, S. , Fu, X. , Hu, X. , and Hu, X. . Manipulation and behavior modeling of one-dimensional nanomaterials on a structured surface. *Applied Surface Science*, 256(14), pp. 4738 – 4744, 2010.

[82] Parsegian, V. A. . *Van der Waals Forces A HANDBOOK FOR BIOLOGISTS, CHEMISTS, ENGINEERS, AND PHYSICISTS*. Cambridge university press, 2006.

[83] MacMillan, W. D. . *Theoretical mechanics Dynamic of rigid bodies*. Dover publications, Inc., 1936.

[84] Prescott, J. . *Mechanics of particles and rigid bodies*. Longmans, green and Co. ltd., third edition edition, 1929.

[85] Andersson, L.-E. and Klarbring, A. . A review of the theory of static and quasi-static frictional contact problems in elasticity. *Philosophical Transactions of the Royal Society of London. Series A:Mathematical, Physical and Engineering Sciences*, 359(1789), pp. 2519–2539, 2001.

[86] Popov, V. . The theory of quasistatic nanomachines. *Technical Physics Letters*, 28, pp. 385–390, 2002.